

Epitaxial growth and characterization of GaAs-based
type-II (GaIn)As/Ga(AsSb)/(GaIn)As
“W”-quantum well heterostructures and lasers

Dissertation

zur
Erlangung des Doktorgrades
der Naturwissenschaften
(Dr. rer. nat.)

dem

Fachbereich Physik
der Philipps-Universität Marburg

vorgelegt von

Christian Fuchs, M.Sc.

aus

Hartenrod

Marburg (Lahn), 2017

Vom Fachbereich Physik der Philipps-Universität Marburg
als Dissertation angenommen am: 23.11.2017
Erstgutachter: Prof. Dr. Wolfgang Stolz
Zweitgutachter: Prof. Dr. Wolfram Heimbrod
Tag der mündlichen Prüfung: 12.12.2017
Hochschulkennziffer: 1180

Originaldokument gespeichert auf dem Publikationsserver der
Philipps-Universität Marburg
<http://archiv.ub.uni-marburg.de>

Danksagung

Die Erstellung der vorliegenden Arbeit wäre ohne die tatkräftige Unterstützung und Motivation durch eine Vielzahl von Kollegen, Freunden und Familienmitgliedern unmöglich gewesen. Insofern möchte ich mich ganz recht herzlich für die tolle gemeinsame Zeit bedanken. Mein besonderer Dank gilt dabei...

... Prof. Dr. Wolfgang Stolz für die exzellente Betreuung, die vielen hilfreichen Diskussionen und Tipps sowie die Möglichkeit meine Dissertation in seiner Arbeitsgruppe anzufertigen. An dieser Stelle darf auch Prof. Dr. Kerstin Volz nicht fehlen, die immer wieder wertvolle Tipps gegeben und das Projekt unterstützt hat.

... Prof. Dr. Wolfram Heimbrodts für die freundliche Übernahme des Zweitgutachtens sowie die hervorragende und erfolgreiche Zusammenarbeit mit seiner Arbeitsgruppe.

... Prof. Dr. Florian Gebhard für die Übernahme des Postens des Prüfungskommissionsvorsitzenden und seine hervorragenden und engagierten Vorlesungen in theoretischer Physik.

... Prof. Dr. Carsten von Hänisch für die kurzfristige Vervollständigung meiner Prüfungskommission.

... Prof. Dr. Stephan W. Koch für die durchweg enge Kooperation im Rahmen dieses Projekts und die scharfsinnigen Anmerkungen zu meinen Ergebnissen.

... Dr. Ada Bäumner, Anja Brüggemann, Dr. Christian Berger, Dr. Christoph Möller und Maria J. Weseloh für die stets freundschaftliche und produktive Zusammenarbeit. Es war mir immer eine große Freude mit euch an diesem Projekt arbeiten zu dürfen!

... den Kollegen von NAsP_{III/V} (Ulrike Häuplik, Dr. Peter Ludewig, Antje Ruiz Perez, Michael Volk, Johannes Zimmet) für die vielen gemeinsamen Stunden beim Sport, die Hilfe bei den experimentellen Arbeiten, die lehrreichen Diskussionen und die "aktive und direkte Unterstützung" bei der Überwindung von Motivationstiefs.

... den Epitaxie-Kollegen (Eduard Sterzer, Lukas Nattermann, Thilo Hepp, Oliver Maßmeyer) für die kollegiale Zusammenarbeit, unzählige Diskussionen und die gute Stimmung im Reinraum.

... den STEM-Kollegen (Dr. Andreas Beyer, Dr. Jan Oliver Oelerich, Pirmin Kükellhan) für ihre hervorragende Arbeit, welche den Fortschritt des Projekts maßgeblich beeinflusst hat.

... Isabelle Kimmel, Marina Koch und Elke Vaupel für exzellente administrative Betreuung. Ohne euch wäre ich wohl im Universitäts-Formular-Dschungel untergegangen.

... Celina Becker, Thomas Ochs und Stefan Reinhard, die jederzeit zur Stelle waren, wenn etwas kaputt war oder technischer Sachverstand erforderlich war.

... Sebastian Gies, Christian Lammers und Markus Stein für die Kooperation im Rahmen diverser Projekte.

... Jürgen Belz und Lennart Duschek für die vielen schönen gemeinsamen Stunden und die fachlichen und “nicht so fachlichen” Gespräche.

... auch allen anderen Kollegen für die schöne gemeinsame Zeit.

... meinen Freunden für die oftmals nötige Ablenkung von der Arbeit.

... meiner Familie – insbesondere meinen Eltern – für ihre bedingungslose Unterstützung.

Zusammenfassung

Unsere heutige Telekommunikation basiert auf der optischen Übertragung von Daten mit Hilfe von Halbleiterlasern, welche typischerweise auf Indiumphosphid-Substraten hergestellt werden. Die Materialschichten, in denen das emittierte Licht generiert wird, sind typischerweise wenige Nanometer dick und werden daher als Quantenfilme bezeichnet. Obwohl dieser Ansatz die Herstellung von Halbleiterlasern in den technologisch wichtigen Wellenlängenbereichen um $1.3\text{ }\mu\text{m}$ und $1.55\text{ }\mu\text{m}$ ermöglicht, ist die Erforschung von alternativen Konzepten von großem Interesse, da die Effizienz der bestehenden Halbleiterlaser durch nichtstrahlende Verlustprozesse limitiert ist. Eine mögliche Alternative stellen Galliumarsenid-basierte Typ-II Heterostrukturen dar, in denen Elektronen und Löcher räumlich voneinander getrennt sind. Daher werden die elektronischen Eigenschaften der beiden Ladungsträgerspezies von unterschiedlichen Materialien dominiert und können unabhängig voneinander angepasst werden, wodurch eine gezielte Reduktion der nichtstrahlenden Verlustprozesse ermöglicht werden könnte. Um sicherzustellen, dass die räumliche Trennung der Elektronen und Löcher in diesen Systemen nicht zu einer ineffizienten strahlenden Rekombination der Ladungsträgerspezies führt, werden diese oft als sogenannte "W"-Struktur angeordnet. Dabei wird ein Lochquantenfilm in zwei Elektronenquantenfilme eingebettet, wodurch der räumliche Überlapp erhöht wird. Die vorliegende Dissertation thematisiert die Herstellung von Typ-II "W"-Strukturen mittels metallorganischer Gasphasenepitaxie und deren Verwendung als aktives Medium in Nahinfrarot-Lasern. Dabei dient das Galliumarsenid-basierte $(\text{GaIn})\text{As}/\text{Ga}(\text{AsSb})/(\text{GaIn})\text{As}$ Materialsystem als Modellsystem.

Da jegliche Folgeuntersuchungen an Typ-II Heterostrukturen und Lasern auf deren Herstellung in hinreichend hoher Qualität aufbauen, wird zunächst die Herstellung mittels metallorganischer Gasphasenepitaxie untersucht. Die Metallorganika Triethylgallium (TEGa), Trimethylindium (TMIn), Tertiärbutylarsin (TBAs) und Triethylantimon (TESb) dienen in dieser Studie als Präkursoren. Aufgrund der Vielzahl an möglichen Kompositions- und Schichtdickenkombinationen wurden der Indiumgehalt auf 20 %, die $(\text{GaIn})\text{As}$ Schichtdicken auf 6 nm und die $\text{Ga}(\text{AsSb})$ Schichtdicke auf 4 nm festgelegt. Entsprechend verbleibt die Antimonkonzentration als letzter freier Parameter, was eine Untersuchung der Wachstumsbedingungen von $\text{Ga}(\text{AsSb})$ ermöglicht. Als Grundlage für diese Herangehensweise diente eine theoretische Studie zur Optimierung des Materialgewinns basierend auf den

vorliegenden Strukturen. Dafür wurden Proben bei einer Wachstumstemperatur von 550 °C mit V/III Gasphasenverhältnissen zwischen 2.0 und 7.5 abgeschieden. Weiterhin wurde das TESb/V Gasphasenverhältnis variiert, um die maximal erreichbare Antimonkonzentration festzustellen und somit den maximal erreichbaren Wellenlängenbereich zu bestimmen. Im Rahmen dieser Studie konnten strukturell hochwertige Typ-II Heterostrukturen mit Antimonkonzentrationen zwischen 19.3 % und 30.2 % demonstriert werden. Diese Konzentrationen entsprachen Photolumineszenzmaxima zwischen 1.22 μm und 1.47 μm , welche eine hohe spektrale Flexibilität dieser Heterostrukturen implizieren.

Die Ergebnisse der Wachstumsstudie werden im Folgenden genutzt, um Injektionslaser abzuschneiden, wobei eine Emissionswellenlänge von 1.2 μm eingestellt wird. Elektrolumineszenzmessungen unterhalb der Laserschwelle offenbaren eine Blauverschiebung als Funktion der Injektionsstromdichte von $(93 \pm 14) \text{ meV}/(\text{kA}/\text{cm}^2)$. Diese Blauverschiebung endet mit dem Einsetzen der stimulierten Emission, welche durch die Verringerung der Linienbreite des Elektrolumineszenzspektrums, sowie ein deutliches Schwellverhalten der Laserkennlinie angedeutet wird. Die Auswertung der Laserkennlinie ergibt außerdem eine Schwellstromdichte von $0.4 \text{ kA}/\text{cm}^2$, eine optische Effizienz von 0.35 W/A pro Facette, welche einer differentiellen Effizienz von 66 % entspricht und einer maximalen gepulsten optischen Ausgangsleistung von 1.4 W pro Facette, welche durch den verwendeten Messaufbau limitiert ist.

Die temperaturabhängige Charakterisierung eines Einzel- und eines Doppel-“W”-Quantenfilmlasers zeigt, dass auch Typ-II Übergänge höherer Ordnung das Emissionsspektrum dominieren können. Übergänge höherer Ordnung werden jedoch nur im Fall des Einzel-“W”-Quantenfilmlasers beobachtet, was die Wichtigkeit des Betriebs bei hinreichend niedrigen Ladungsträgerdichten hervorhebt. Weiterhin wird die Temperaturstabilität der Schwellstromdichte, sowie der differentiellen Effizienz, im Rahmen dieser Studie untersucht und mit einem exponentiellen Modell beschrieben. Dabei dienen die sogenannten charakteristischen Temperaturen T_0 und T_1 als Parameter, welche eine Aussage über die Temperaturstabilität ermöglichen. Die Untersuchung ergibt charakteristische Temperaturen von $T_0 = (56 \pm 2) \text{ K}$ und $T_1 = (105 \pm 6) \text{ K}$ für den Einzel-“W”-Quantenfilmlaser, sowie $T_0 = (60 \pm 2) \text{ K}$ und $T_1 = (107 \pm 12) \text{ K}$ für den Doppel-“W”-Quantenfilmlaser. Diese verhältnismäßig niedrigen T_0 -Werte führen in Kombination mit der zuvor beschriebenen Blauverschiebung zu einer Modifikation der temperaturinduzierten Verschiebungsrates der Emissionswellenlänge, wodurch sogar negative Verschiebungsrates demonstriert werden können. Diese Modifikation kann als fundamentaler Unterschied zu Typ-I Lasern verstanden werden und ermöglicht als solcher die Untersuchung von neuartigen Bauelementkonzepten und könnte zur Optimierung bestehender Bauelementkonzepte beitragen.

Neben den bereits thematisierten Injektionslasern konnte auch ein weiteres Halbleiterlaserkonzept mit “W”-Quantenfilmen als aktives Medium realisiert werden. Es handelt sich dabei um optische gepumpte *vertical-external-cavity surface-emitting laser* (VECSEL). Dabei konnte eine maximale Ausgangsleistung von 4 W im Dauerstrichbetrieb demons-

triert werden. Die charakteristische Blauverschiebung spielt auch bei diesen Bauelementen eine wichtige Rolle und erfordert eine positive Verstimmung des Resonators und der Emissionswellenlänge bei niedrigen Anregungsleistungen.

Während die zuvor genannten Ergebnisse vielversprechend sind und das Anwendungspotenzial von Typ-II Heterostrukturen in Halbleiterlasern unterstreichen, wurde bisher eine wichtige Eigenschaft von Halbleiterlasern vernachlässigt. Ihre spektrale Flexibilität ist ein wichtiges Argument für ihre Verwendung, da dadurch die Anpassung der Emissionswellenlänge an die jeweilige Aufgabe möglich ist. Ein wichtiges Wellenlängenfenster ist dabei der Bereich um $1.3\text{ }\mu\text{m}$, welcher für Telekommunikationsanwendungen genutzt wird. Die theoretische Optimierung der “W”-Struktur für diese Emissionswellenlänge führt zur erfolgreichen Demonstration eines Doppel-“W”-Quantenfilmlasers bei $1.3\text{ }\mu\text{m}$. Dieser kann bis mindestens $100\text{ }^{\circ}\text{C}$ betrieben werden und Elektroluminszenzmessungen zeigen, dass der Laserbetrieb auch bei $100\text{ }^{\circ}\text{C}$ auf dem fundamentalen Typ-II Übergang basiert. Die temperaturabhängige Charakterisierung ergibt charakteristische Temperaturen von $T_0 = (132 \pm 3)\text{ K}$ und $T_1 = (109 \pm 12)\text{ K}$. Weiterhin werden bei $20\text{ }^{\circ}\text{C}$ eine Schwellstromdichte von 1.0 kA/cm^2 , eine differenzielle Effizienz von 41% und eine maximale gepulste optische Ausgangsleistung von 0.68 W pro Facette beobachtet, wobei diese wiederum durch den verwendeten Messaufbau limitiert ist.

Die obigen Ergebnisse zeigen, dass Typ-II Heterostrukturen interessante fundamentale Eigenschaften aufweisen, welche in zukünftigen Untersuchungen näher betrachtet werden sollten. Dazu zählen unter anderem eine Analyse der Ladungsträgerdynamik in solchen Systemen und die Analyse ihrer strukturellen Eigenschaften mittels Transmissionselektronenmikroskopie. Desweiteren ermöglicht die erstmalige Herstellung von effizienten Typ-II Injektionslasern im Nahinfrarot-Bereich die Untersuchung der Auger Rekombination in diesen Systemen, was zu einer weiteren Optimierung von Halbleiterlasern in diesem Spektralbereich beitragen kann. Zudem vereinfachen die hier präsentierten Erkenntnisse die Ausweitung der erreichbaren Emissionswellenlänge auf weitere technologisch wichtige Wellenlängenbereiche mittels ähnlicher Materialsysteme. Einer der nächsten Schritte sollte daher die Untersuchung von Typ-II Heterostrukturen, welche die Demonstration von Injektionslasern mit einer Emissionswellenlänge von $1.55\text{ }\mu\text{m}$ ermöglichen, sein.

Contents

1	Introduction	1
2	Physical background	3
2.1	Fundamental semiconductor physics	3
2.2	Semiconductor lasers	7
2.2.1	Electrical injection lasers	7
2.2.2	Vertical-external-cavity surface-emitting lasers (VECSELs)	13
2.2.3	Loss channels	15
2.2.3.1	Charge carrier leakage	15
2.2.3.2	Shockley–Read–Hall recombination	17
2.2.3.3	Inter-band absorption	17
2.2.3.4	Auger recombination	19
2.3	Type-II heterostructures	20
2.3.1	Challenges	20
2.3.2	Advantages	22
3	Experimental methods	25
3.1	Metal organic vapor phase epitaxy (MOVPE)	25
3.2	High resolution X-ray diffraction (HR-XRD)	27
3.3	Photoluminescence (PL) spectroscopy	29
3.4	Laser studies	31
3.4.1	Electroluminescence (EL) spectroscopy	31
3.4.2	Laser characteristics	33
4	Results	35
4.1	Epitaxial growth and spectral coverage of “W”-QWHs	35
4.2	Electrical injection lasers emitting at 1.2 μm	37
4.2.1	Temperature-dependent properties	38
4.3	VECSELs emitting at 1.2 μm	41
4.4	Electrical injection lasers emitting at 1.3 μm	43
5	Conclusion and outlook	45

6	Scientific contributions	47
6.1	Publication 1	47
6.2	Publication 2	54
6.3	Publication 3	57
6.4	Publication 4	62
6.5	Further publications	69
6.6	Talks and posters	70
	Bibliography	71

CHAPTER 1

Introduction

Buzz words such as “Big Data”, “Cloud Storage”, and “Internet of Things” are often mentioned in recent years. While all of them are technological trends, they have something else in common. They require the transmission of increasing amounts of data at ever higher transmission rates. The transmission of such vast amounts of data is carried out using fiber-optic telecommunication systems utilizing semiconductor lasers as light source¹. Especially long-haul telecommunication systems need to operate at particular wavelengths, namely 1.3 μm and 1.55 μm , where the dispersion or absorption in silica fiber is minimal, respectively. Consequently, InP-based material systems such as (GaIn)(AsP)/InP² and (AlGaIn)As/InP^{3–7} are frequently chosen as active materials in these devices. However, their wall-plug efficiencies are – among other reasons – limited by Auger recombination^{2,3,5–8} and external coolers are required to stabilize the emission at the above mentioned wavelengths⁹.

The application of type-II heterostructures was suggested in order to suppress Auger recombination^{10,11}. Electrons and holes are spatially separated in these heterostructures and charge carrier recombination occurs across an interface. Consequently, at least two different quantum well materials are required in case of these active regions for the confinement of electrons and holes, respectively. While the spatial separation of charge carriers results in more flexible band structure engineering opportunities, it also results in a decreased wave function overlap between both charge carrier species. Therefore, so called “W”-quantum well heterostructures, where a hole quantum well is embedded in between two electron quantum wells, are an alternative that provides a good wave function overlap as well as a type-II band alignment. One particularly promising GaAs-based material system is the (GaIn)As/Ga(AsSb)/(GaIn)As material system, where the well-established growth conditions of (GaIn)As facilitate the fabrication of these heterostructures^{12–15}. The investigation of bilayer^{16–19} as well as “W”-quantum well heterostructures^{20–26} ultimately resulted in the demonstration of the first electrical injection lasers emitting at 1.2 μm based on both design concepts^{27,28}. Furthermore, the investigation of similar structures based on GaSb^{11,29–34} and InP substrates^{35–40} yielded a further extension of the emis-

sion wavelengths into the mid-infrared wavelength regime. These results are especially promising due to the recent demonstration of semiconductor lasers utilizing InP-based (GaIn)As/Ga(AsSb)/(GaIn)As “W”-quantum well heterostructures^{41–44}. However, despite these promising results, no detailed studies of lasers emitting at the above mentioned telecommunication wavelengths are available in the literature.

Consequently, the present work aims at the investigation of the epitaxial growth of GaAs-based (GaIn)As/Ga(AsSb)/(GaIn)As “W”-quantum well heterostructures as well as the demonstration and investigation of semiconductor lasers emitting at 1.3 μm grown on GaAs substrates. A more detailed introduction of the underlying physics and experimental methods is given in Cha. 2 and Cha. 3, respectively. The epitaxial growth of type-II “W”-quantum well heterostructures, edge-emitting lasers, and vertical-external-cavity surface-emitting lasers as well as their fundamental physical properties are discussed in Cha. 4. Additionally, an outlook on possible future experiments is given in Cha. 5 and the publications resulting from this work are provided in Cha. 6.

CHAPTER 2

Physical background

2.1 Fundamental semiconductor physics

The following section introduces the electronic properties of III/V compound semiconductors and their resulting interaction with light. These information will be used to explain the functional principle of semiconductor lasers in Sec. 2.2.

While the electronic structure of single atoms is dominated by discrete energy levels, the energetic structure of III/V semiconductors differs because they are crystalline solids. The crystal structure of all materials investigated in this thesis is a cubic Zincblende structure. It consists of two face-centered cubic (fcc) lattices which are shifted by a quarter of the space diagonal with respect to each other and each fcc sublattice is either occupied by group-III or group-V atoms. They can be considered as a periodic arrangement of N_a atoms where $N_a \rightarrow \infty$. The weakly bound outer valence electrons of these atoms interact with neighboring atoms resulting in a covalent bonding configuration and the corresponding wave functions are extended over the whole crystal. Consequently, the sharp energy levels of the constituent atoms are split up. However, due to the large amount of new states, the energetic separation between them is small and quasi-continuous bands of allowed energies are formed⁴⁵. It is also important to note that the difference in electronegativity between group-III and group-V atoms also results in a small ionic contribution to the bonding in III/V semiconductors⁴⁶.

The nomenclature of the energy bands is similar to the one used for atomic energy levels. The last fully filled energy band and the first completely empty energy band at a temperature T of 0 K are referred to as valence and conduction band, respectively. These bands are separated by a band gap energy E_g . The band gap defines an energy range in which no energy states exist in case of an ideal crystal. The existence of such a band gap distinguishes semiconductors from metals. The difference between semiconductors and insulators on the other hand is less well-defined. Materials with a band gap energy below $E_g \approx 4 \text{ eV}$ are referred to as semiconductors whereas materials with a larger band gap energy are referred to as insulators. Semiconductors are split up into two main categories:

direct and indirect semiconductors. In order to understand the difference between both types of semiconductors, the left-hand side of Fig. 2.1 can be considered. It illustrates the band structure of a semiconductor in reciprocal space. If the global band extrema of the conduction and the valence band are both located at $k = 0$, which is also referred to as Γ -point, the semiconductor is direct. Examples for direct semiconductors are GaAs and InP. If, however, the band extrema are located at different positions in reciprocal space, the semiconductor is indirect. Examples for indirect semiconductors are Si and Ge, but also III/V semiconductors such as AlAs and GaP exhibit an indirect band gap.

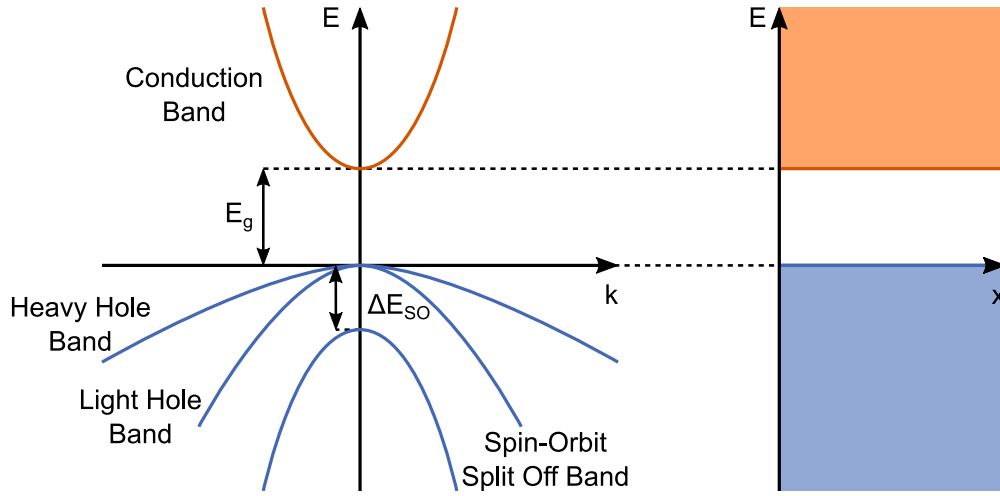


Figure 2.1: The left-hand side of the figure schematically illustrates the band structure of a direct III/V semiconductor in reciprocal space in the vicinity of the Γ -point. It includes the conduction band which is separated from the valence band by an energy gap of E_g . The valence band itself consists of three bands: the heavy hole, the light hole, and the spin-orbit split off band. The spin-orbit split off band is separated by the other two valence bands by an energy ΔE_{SO} at $k = 0$. The valence bands are the last fully filled bands at a temperature of 0 K while the conduction band is completely empty at this temperature. The right-hand side of the graphic schematically illustrates the band structure of a semiconductor in real space. In order to obtain this structure, only the extrema of the conduction and the valence band are considered.

The energy bands are often approximated as parabolas in the vicinity of their respective extrema. This simple approximation using Eq. (2.1) allows for the definition of the effective mass m^* which enables the description of transport in semiconductors in a free particle picture by substituting the mass of a free electron m_0 with m^* . In order to obtain a further facilitation of the theoretical description of charge carriers in these bands, holes are introduced as quasiparticles. They can be considered as missing electrons and are responsible for conduction in the valence band.

$$E = \frac{\hbar^2 \cdot k^2}{2 \cdot m^*} \quad (2.1)$$

An additional feature illustrated on the left-hand side of Fig. 2.1 is the fact that the valence band is more complex than the conduction band. It consists of a heavy hole, a

light hole, and a spin-orbit split-off band. The names heavy hole and light hole band refer to the different effective masses of holes in these bands as outlined above. The spin-orbit split off energy ΔE_{SO} between the spin-orbit split off band and the other valence bands at the Γ -point results from the interaction between the electrons' orbital and angular momentum. ΔE_{SO} scales with the atomic number of the group-V atoms. Consequently, it is almost negligible in III-nitrides and is predicted to be as large as $\Delta E_{SO} \approx 2\text{ eV}$ in III-bismides⁴⁷.

Another important band structure representation is the representation of the band structure in real space. It is particularly useful for the design of semiconductor devices since device dimensions are typically well-known and most of the important processes occurring in devices are based on charge carriers located close to the band extrema. It can be obtained from the reciprocal space representation by identifying the conduction and the valence band using their respective extrema as illustrated in the right-hand side of Fig. 2.1.

Light-matter interaction is typically discussed in the framework of three major processes. On the one hand, it is possible to excite electrons from the valence to the conduction band leaving behind a hole in the valence band by absorbing a photon carrying an energy E_{ph} that is at least as large as the band gap energy E_g . On the other hand, the recombination of an electron and a hole can result in the emission of a photon. In this case, two different processes have to be distinguished. The coincidental recombination of electrons and holes resulting in the emission of photons is referred to as spontaneous emission and the light emitted due to this process is incoherent. However, if the emission process is triggered by another photon of the same energy, the process is referred to as stimulated emission and results in the emission of coherent light. Absorption, spontaneous emission, and stimulated emission within a two-level system are illustrated in Fig. 2.2 a), b) and c), respectively.

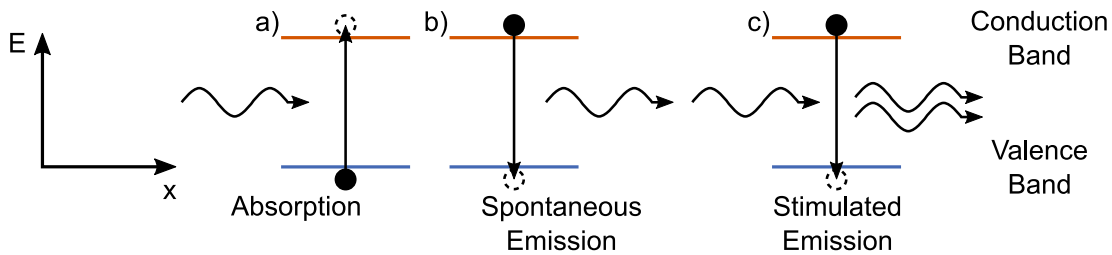


Figure 2.2: Light-matter interaction is schematically illustrated. a) In case of absorption, an incoming photon is absorbed and an electron is excited from the valence to the conduction band leaving behind a hole. b) In case of spontaneous emission, an excited electron recombines with a hole and a photon is emitted. c) In case of stimulated emission, the emission of a photon due to the recombination of an electron and a hole is stimulated by an incoming photon. As a result, both photons are coherent. Furthermore, it is important to note that energy and momentum are conserved in case of all processes.

A major advantage of III/V semiconductors with respect to applications in photonic devices is that their absorption and emission wavelengths can be tailored by using different alloys. Tab. 2.1 summarizes basic parameters that can be used to characterize the band

structure of GaAs, InAs, and GaSb. Since the band gap energies of GaAs and InAs are $E_g(\text{GaAs}) = 1.422 \text{ eV}$ and $E_g(\text{InAs}) = 0.354 \text{ eV}$, respectively, one can expect that the whole range in between these values can be covered using the ternary alloy (GaIn)As.

Table 2.1: Summary of band parameters of the binary III/V semiconductors GaAs, InAs, and GaSb⁴⁸.

Binary material	GaAs	InAs	GaSb
Lattice constant a (Å) [300 K]	5.65325	6.0583	6.0959
Band gap energy E_g (eV) [0 K]	1.519	0.417	0.812
Varshni parameter α (meV/K)	0.5405	0.276	0.417
Varshni parameter β (K)	204	93	140
Band gap energy E_g (eV) [300 K]	1.422	0.354	0.727
Spin-orbit split off energy ΔE_{SO} (eV)	0.341	0.39	0.76
Effective mass (electrons) m_e^* (m_0)	0.067	0.026	0.039
Effective mass (heavy holes) m_h^* [001] (m_0)	0.350	0.333	0.250
Effective mass (light holes) m_l^* [001] (m_0)	0.090	0.027	0.044
Effective mass (spin-orbit split off) m_{SO}^* (m_0)	0.172	0.14	0.12

However, the properties of an alloy cannot be obtained using a simple linear interpolation between its ternary constituents. A bowing parameter C is used in order to describe the deviation from the linear model. Thereby, it is possible to calculate a property P of an alloy which is created by mixing two different binary materials M^A and M^B . An example for the application of the bowing parameter in case of a ternary alloy formed between a mole fraction $(1-x)$ of M^A and a mole fraction x of M^B is given in Eq. (2.2).

$$P(M_{1-x}^A M_x^B) = (1-x) \cdot P(M^A) + x \cdot P(M^B) - x \cdot (1-x) \cdot C \quad (2.2)$$

A summary of bowing parameters for (GaIn)As and Ga(AsSb) is given in Tab. 2.2.

Table 2.2: Summary of bowing parameters of the ternary III/V semiconductors (GaIn)As and Ga(AsSb)⁴⁸.

Ternary alloy	(Ga _{1-x} In _x)As	Ga(As _{1-y} Sb _y)
Band gap energy E_g (eV)	0.477	1.43
Spin-orbit split off energy ΔE_{SO} (eV)	0.15	0.6
Effective mass (electrons) m_e^* (m_0)	0.0091	-
Effective mass (heavy holes) m_h^* [001] (m_0)	-0.145	-
Effective mass (light holes) m_l^* [001] (m_0)	0.0202	-

Direct band gaps are typically desired for any photonic application due to the more efficient radiative recombination. Thus, GaAs and InP are the most commonly used substrate materials and the majority of alloys applied in commercial semiconductor lasers emitting in the infrared wavelength regime are based on them. This circumstance results

from the small momentum of photons which implies that any transitions which result in the emission or the absorption of photons are vertical in reciprocal space, if no other quasiparticles are involved. Furthermore, it is possible to fabricate almost defect-free heterostructures, because a variety of zinc blende alloys with similar lattice constants can be designed and their band gap energy can be tuned over a wide energetic range as shown in Fig. 2.3. These alloys enable the fabrication of tailored devices that satisfy the spectral requirements of various applications.

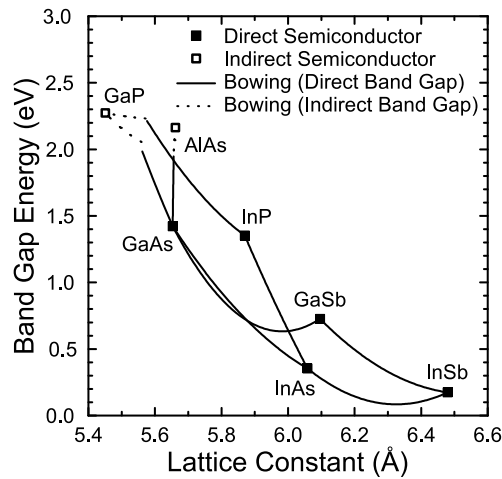


Figure 2.3: Plot of the band gap energy against the lattice constant of III/V semiconductors, which are utilized in the present thesis. A temperature of 300 K is assumed and all band gaps, bowing parameters and lattice constants were taken from Vurgaftman et al.⁴⁸.

2.2 Semiconductor lasers

After the first demonstration of an optically pumped laser using a ruby crystal as active medium in 1960⁴⁹, the application of semiconductors as active materials in lasers was of great interest. The first semiconductor lasers were demonstrated in 1962 and their development is ongoing⁵⁰, because they proved to be excellent laser systems if efficient, reliable, inexpensive, and compact devices are required.

2.2.1 Electrical injection lasers

The fundamental components of semiconductor lasers are similar to the components used for other laser systems. It requires a pump source that provides the energy for the excitation of charge carriers, a laser cavity including mirrors for optical feedback, and an active region in which light is generated. The active region typically consists of one or several quantum wells (QWs). While several material systems could be applied in semiconductor lasers, the choice of material systems is limited due to the high quality standards that are required for efficient and reliable laser devices. III/V compound semiconductors based on

GaAs or InP proved to be suitable materials for lasers emitting in the infrared wavelength regime as outlined in Sec. 2.1.

The purpose of the laser cavity is to guide the optical mode in close proximity to the active region in order to provide a sufficient feedback for laser operation. Optical confinement perpendicular to the QW plane is provided by stacking materials with different refractive indices n . Since the QW thickness is much smaller than the wavelength of the emitted light, it almost does not contribute to optical confinement. Therefore, the cavity used for the present devices is build of cladding layers consisting of $(\text{Al}_z\text{Ga}_{1-z})\text{As}$ ($z = 0.4$) and separate confinement heterostructures (SCH) consisting of GaAs as illustrated in Fig. 2.4 a). The resulting transverse optical mode ϵ is confined to the SCH which surrounds the active region. Since the thickness of the SCHs and thus, the spatial extent of the optical mode is larger than the thickness of the active region, an optical confinement factor Γ is introduced. It is defined as the fraction of the intensity of the optical mode that overlaps with the active region compared to the total intensity across the full structure as shown in Eq. (2.3).

$$\Gamma = \frac{\int_{\text{active}} \epsilon^2 dx}{\int_{\text{full}} \epsilon^2 dx} \quad (2.3)$$

Furthermore, one of the cladding layers is p-doped and the other one is n-doped in order to allow for electrical current injection as pump source. The band gap energy of all materials used to build the cavity is typically larger than the energy of photons emitted from the active region in order to prevent an absorption of the optical mode.

Confinement in one in-plane direction is obtained by exploiting the cleavage properties of III/V semiconductors. The surface energy per unit area is minimal in case of the $\{110\}$ planes⁴⁶ and thus, the cleavage of GaAs along these planes results in mirror-grade facets. Furthermore, the refractive indices of GaAs and $(\text{AlGa})\text{As}$ are larger than 3 in the infrared wavelength regime⁵¹ resulting in as-cleaved mirror reflectivities of $R \approx 0.3$. The distance between two mirrors defines the cavity length of the laser device. Typical cavity lengths between $L = 700 \mu\text{m}$ and $2000 \mu\text{m}$ are used in the present study in order to ensure that the device is operated using suitable charge carrier densities and to obtain high efficiencies. The above-mentioned device geometry resembles a Fabry–Pérot resonator resulting in longitudinal modes due to the standing wave condition defined in Eq. (2.4a) where m is an integer and λ is the wavelength of the light. The resulting modes are energetically separated as outlined for the light's wavelength $\Delta\lambda$ and frequency $\Delta\nu$ in Eqs. (2.4b) and (2.4c), respectively, where λ_0 is the peak wavelength of the luminescence spectrum.

$$L = \frac{m \cdot \lambda}{2 \cdot n} \quad (2.4a)$$

$$\lambda = \frac{2 \cdot n \cdot L}{m} \quad \Delta\lambda = \frac{\lambda_0^2}{2 \cdot n \cdot L} \quad (2.4b)$$

$$\nu = \frac{m \cdot c}{2 \cdot n \cdot L} \quad \Delta\nu = \frac{c}{2 \cdot n \cdot L} \quad (2.4c)$$

Confinement in the remaining direction is achieved by restricting the top contact and the highly p-doped GaAs cap to a certain width which is referred to as cavity width W . The p⁺-GaAs cap is used to ensure small contact resistances and to prevent an oxidation of the p-(AlGa)As cladding. The bottom contact covers the whole backside substrate surface of the device and the current flow is limited to the region underneath the top contact. Therefore, only the active region below the top contact can contribute photons to the laser emission as illustrated in Fig. 2.4 b). This confinement concept is referred to as gain-guiding and the present devices are referred to as broad-area edge-emitting lasers because large cavity widths of $W = 50 \mu\text{m}$ and $100 \mu\text{m}$ are used.

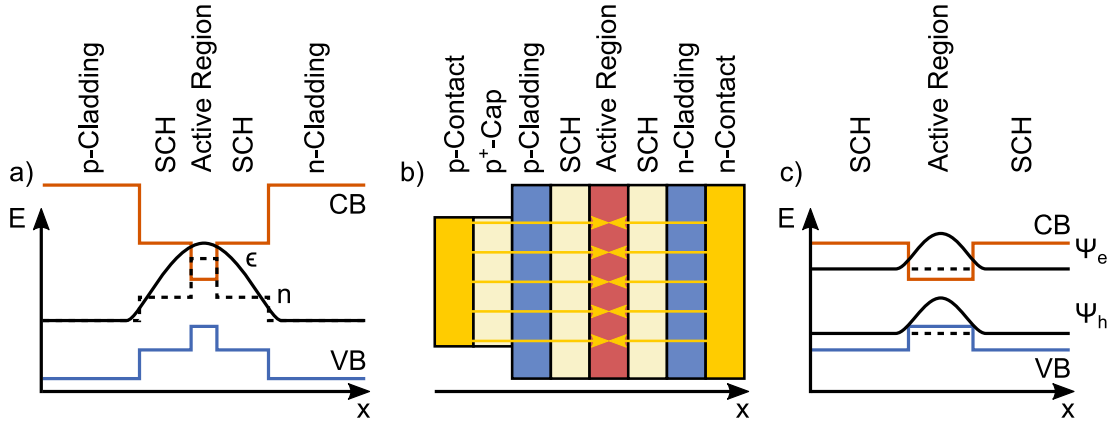


Figure 2.4: a) Illustration of optical confinement using the refractive index contrast between cladding layers and the separate confinement heterostructure. The resulting optical mode ϵ is confined to the separate confinement heterostructure region. b) Illustration of gain-guiding by restricting the contact area to certain regions of the laser bar. Consequently, current flow is only possible below the contact area. c) Illustration of electronic confinement using a quantum well. The wave functions of the ground state energy levels are indicated together with their energetic positions. The large wave function overlap between the electron and the hole wave functions results in efficient radiative recombination.

The active region is defined as the region where radiatively recombining charge carriers contribute to the gain and the photon emission of the device. It is typically the region of the devices with the smallest band gap energy as outlined above. While the first demonstrations of semiconductor lasers were achieved using bulk structures, present-day devices typically consist of QW active regions. A single or multiple QWs may be used as active region depending on the actual device design and the desired carrier density per QW. QW heterostructures (QWHs) became popular due to their strong electronic confinement of electrons and holes, which is illustrated in Fig. 2.4 c). It results in a large wave function

overlap and thus, efficient radiative recombination. The confinement in one dimension results in an altered density of states, an increased differential gain, and facilitated inversion compared to the bulk case leading to low laser thresholds^{52–54}, decreased temperature sensitivity⁵⁵, and narrower gain spectra⁵⁶. Furthermore, the application of thin QWs rather than thick bulk layers offers the possibility to access new spectral regimes because the strict strain limitations are avoided.

In order to evaluate and compare laser devices, it is necessary to develop a simple model that describes the optical output power of the device under operating conditions. In terms of its electrical characteristics, the devices behave like an ohmic resistor as soon as flat band conditions are established in the p-i-n junction. An increasing amount of electrons and holes is injected into the active region and starts to recombine. The total recombination rate R_{rec} can be described using Eq. (2.5). It includes radiative recombination, i.e. stimulated (R_{st}) and spontaneous emission (R_{sp}) (cf. Fig. 2.2 b) and c)), non-radiative recombination (R_{nr}), and charge carrier leakage (R_l). Non-radiative recombination includes all processes that do not result in the emission of a photon based on the desired transition and leakage processes include all processes that do not result in the injection of charge carriers into the active region.

$$R_{\text{rec}} = R_{\text{st}} + R_{\text{sp}} + R_{\text{nr}} + R_l \quad (2.5)$$

Light emission is dominated by spontaneous emission in case of low charge carrier densities because stimulated emission requires optical feedback, which is not provided due to the small field intensities. Therefore, the structure acts as a light-emitting diode before laser operation starts, i.e. before reaching the laser threshold. A simple description of the optical output power of a laser device below threshold P_{LED} can be obtained by assuming a linear relationship between the injection current I and the optical output power as shown in Eq. (2.6). The external quantum efficiency η_{ext} is used to describe that only a part of the injection current is actually used to generate photons that are coupled out of the laser cavity. Additionally, the Planck constant h and the elementary charge q are required to calculate how many photons of frequency ν are generated per second.

$$P_{\text{LED}}(I) = \eta_{\text{ext}} \cdot \frac{h \cdot \nu}{q} \cdot I \quad (2.6)$$

As more charge carriers are injected, the absorption coefficient of the active region becomes negative. It is then referred to as material gain g_{mat} and describes the ability of the active region to amplify incident light. The material gain is not sufficient for the description of the above mentioned laser structure, because the light mode is also extended to the SCH. Therefore, the modal gain g_{mod} is defined by multiplying the material gain with the optical confinement factor Γ as shown in Eq. (2.7).

$$g_{mod} = g_{mat} \cdot \Gamma \quad (2.7)$$

The loss channels introduced in Eq. (2.5) also need to be considered in order to obtain an accurate description of the device. The internal losses α_i include all scattering and absorptive losses that the optical mode experiences. Additionally, the light coupled out of the cavity is useful for the application of the laser, but it has to be considered as another loss channel, because the light that is coupled out of the cavity cannot provide any optical feedback. Thus, the total loss α is a combination of internal losses and the mirror loss α_m . Its definition is given in Eq. (2.8a) while the mirror loss is defined in Eq. (2.8b).

$$\alpha = \alpha_i + \alpha_m \quad (2.8a)$$

$$\alpha_m = \frac{1}{L} \cdot \ln\left(\frac{1}{R}\right) \quad (2.8b)$$

The definitions given above can now be used in order to define the laser threshold. On the one hand, population inversion is required in order to achieve material gain. This means that the separation of the quasi Fermi levels E_{FC} and E_{FV} of the electrons and holes has to be at least as large as the energetic separation between the transitions involved in the emission process. The latter defines the energy of the photons E_{ph} . On the other hand, the resulting modal gain at threshold $g_{mod,th}$ must be large enough to cancel the total loss. Both laser threshold conditions are summarized in Eqs. (2.9a) and (2.9b), respectively.

$$E_{FC} - E_{FV} > E_{ph} > E_g \quad (2.9a)$$

$$g_{mat,th} \cdot \Gamma = g_{mod,th} = \alpha \quad (2.9b)$$

A more demonstrative illustration of the second gain condition is given in Fig. 2.5. As soon as longitudinal laser modes resulting from a superposition of the modal gain and the Fabry–Pérot resonance exceeds the total loss, laser operation based on these modes is observed.

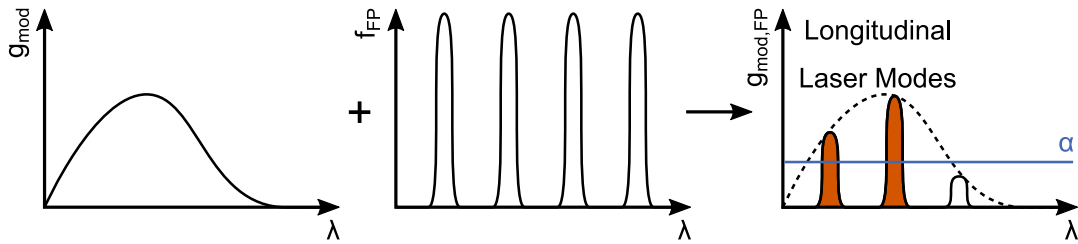


Figure 2.5: The origin of longitudinal laser modes observed in laser spectra is illustrated as a superposition of the modal gain and the Fabry–Pérot resonances. Longitudinal modes that exceed the total loss are shown in red and laser operation based on these modes will be observed.

Stimulated emission dominates the recombination of charge carriers above laser threshold. As a consequence, the modal gain above threshold is pinned (Eq. (2.10a)), because additional charge carriers introduced into the system recombine through stimulated emission resulting in a constant charge carrier density (Eq. (2.10b)). I_{th} is the threshold (injection) current which is defined as the current starting from which laser operation is observed. Furthermore, the narrowing of the emission spectrum resulting from the transition from spontaneous to stimulated emission is considered as an additional experimental indicator for laser operation.

$$g_{mod}(I > I_{th}) = g_{mod,th} \quad (2.10a)$$

$$n(I > I_{th}) = n_{th} \quad (2.10b)$$

The output power above threshold P_{laser} is described in a similar manner as the output power below threshold. It is assumed to be proportional to the excess current relative to the threshold current and the differential quantum efficiency η_d . The differential quantum efficiency includes the fraction of light that is coupled out of the laser cavity and the internal quantum efficiency η_i , which can be considered as a measure of how many electrons injected into the device contribute to the generation of laser emission.

$$P_{laser}(I) = \eta_d \cdot \frac{h \cdot \nu}{q} \cdot (I - I_{th}) = \eta_i \cdot \frac{\alpha_m}{\alpha} \cdot \frac{h \cdot \nu}{q} \cdot (I - I_{th}) \quad (2.11)$$

The differential efficiency can be determined by measuring laser characteristics, i.e. the optical output power as a function of the injection current.

$$\eta_d(I > I_{th}) = \frac{q}{h \cdot \nu} \cdot \frac{dP}{dI} \quad (2.12)$$

The determination of the internal quantum efficiency and the internal losses is more complicated because they cannot be determined by measuring a single device. Eq. (2.13) is obtained from Eqs. (2.8b) and (2.11) and shows that the differential efficiency depends on the cavity length. Furthermore, the internal quantum efficiency, the internal losses and the mirror reflectivities define the exact dependency of the differential efficiency. The mirror reflectivities are known and thus, the above mentioned properties can be determined by measuring a series of devices with different cavity lengths.

$$\frac{1}{\eta_d} = \frac{\alpha_i}{\eta_i \cdot \ln\left(\frac{1}{R}\right)} \cdot L + \frac{1}{\eta_i} \quad (2.13)$$

The temperature stability of semiconductor lasers is highly important for their technological application because a reliable operation must be ensured. Telecommunication lasers are typically required to operate up to temperatures of $T = 85^\circ\text{C}$ resulting in a large

range of operating conditions that need to be covered. An increasing device temperature results in an increase of the threshold current and a decrease of the differential efficiency. Exponential models are used to describe their behavior as shown in Eqs. (2.14a) and (2.14b). The characteristic temperatures T_0 and T_1 are used as a figure of merit for the thermal stability of the threshold current and differential efficiency, respectively. Large characteristic temperatures are desired as they correspond to a high thermal stability of the device.

$$I_{th}(T) = I_{th,0} \cdot \exp\left(\frac{T}{T_0}\right) \quad (2.14a)$$

$$\eta_d(T) = \eta_{d,0} \cdot \exp\left(-\frac{T}{T_1}\right) \quad (2.14b)$$

Typical characteristic temperatures of InP-based lasers emitting in the telecommunication regime reported in the literature are $T_0 = 50 - 80$ K and $T_0 = 100 - 120$ K for (GaIn)(AsP)/InP² and (AlGaIn)As/InP³⁻⁷, respectively.

2.2.2 Vertical-external-cavity surface-emitting lasers (VECSELs)

Edge-emitting lasers tend to be limited by their beam quality and the achievable optical output power due to thermal roll-over under continuous wave (CW) operating conditions. The beam quality of electrical injection lasers can be improved by using alternative cavity concepts that enable surface-emission. In order to achieve surface emission, an optical cavity is formed by sandwiching the active region in between two epitaxial distributed Bragg reflectors (DBRs), which are n- and p-doped, respectively. These lasers are referred to as vertical-cavity surface-emitting lasers (VCSELs). However, the highest CW optical output power based on a single device was achieved using optically pumped lasers⁵⁷, where only one undoped DBR and an additional external output mirror are used. The optical pumping scheme enables the application of thermal management techniques, which were developed for solid state disk lasers and thus, thermal roll-over can be delayed. These devices are referred to as vertical-external-cavity surface-emitting lasers (VECSELs) and are introduced in the following section.

The VECSEL design used in the present thesis consist of three main parts that are required to form a laser cavity in combination with the external output mirror. A monolithically integrated and highly reflective (AlGa)As/AlAs-based DBR serves as second mirror in order to provide the feedback required for stimulated emission. Its fabrication is enabled by the circumstance that AlAs and GaAs exhibit almost the same lattice constant while providing a large refractive index contrast. The layer thicknesses of (AlGa)As and AlAs correspond to $\lambda_{ph}/4$, where λ_{ph} is the VECSEL's emission wavelength in the respective medium in order to obtain a high reflectivity due to the constructive

interference of the reflected light wave. The amount of (AlGa)As/AlAs pairs depends on the desired reflectivity and is often larger than 20.

The active region typically consists of a periodic arrangement of multiple QWs which are separated by GaAs/Ga(AsP)/GaAs barriers. The distance between the center of two neighboring QWs is defined by $\lambda_{ph}/2$. Thus, the anti-nodes of the optical light field intensity of the standing wave, which results from highly reflective DBR and the large refractive index contrast to air, coincide with the QW positions. This arrangement is also referred to as resonant periodic gain (RPG). Consequently, a longitudinal confinement factor (LCF) Γ_z is defined analogously to the optical confinement factor Γ introduced in Sec. 2.2.1 for the calculation of the modal gain. In addition to their function as separating layers, which establish the above mentioned resonance, the barriers also serve as strain compensation layers for the typically compressively strained QWs and provide the hetero barrier for the electronic confinement in the QWs. Furthermore, a lattice matched $\lambda_{ph}/2$ (GaIn)P layer, which prevents surface-induced leakage of charge carriers, is added in between the outermost barrier and the ambient air. The resulting VECSEL structure, which is mounted on a diamond heat spreader and a copper heat sink, is schematically illustrated in Fig. 2.6 a) together with the optical light field intensity of the standing wave.

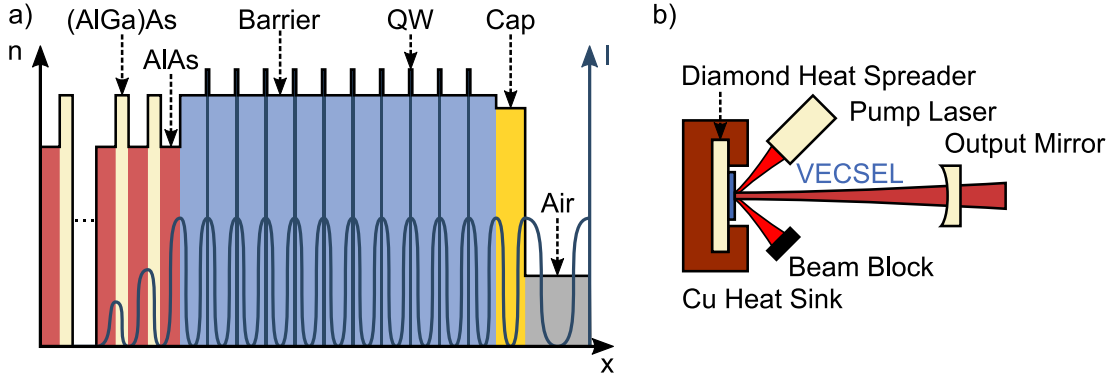


Figure 2.6: a) Illustration of the refractive index profile of a VECSEL based on an (AlGa)As/AlAs DBR, a RPG and a cap. The anti-nodes of the standing wave light field intensity coincide with the QW positions. b) Illustration of a linear VECSEL cavity in which the VECSEL chip is mounted on a copper heat sink and optically pumped using a laser. The second cavity mirror is an external output mirror.

The devices are optically pumped using a fiber-coupled diode laser with an emission wavelength of $\lambda = 808 \text{ nm}$ and typically arranged in a linear cavity, which is illustrated in Fig. 2.6 b). The absorption of pump light mostly occurs in the barriers because their total layer thickness is typically much larger than the overall thickness of the QWs. Furthermore, the photon energy of the pump light E_{pump} is larger than the energy of the emitted photons E_{ph} . Consequently, the relaxation of excited carriers into the confined states in the QWs requires the emission of phonons and results in a heating of the VECSEL. This circumstance is referred to as quantum defect and the fraction of the energy that is released as heat is defined by Eq. (2.15). The quantum defect amounts to about 33 % if

an emission wavelength of $1.2\mu\text{m}$ is assumed, which results in an increase of the VECSEL chip's temperature.

$$\eta_{QD} = 1 - \frac{E_{ph}}{E_{pump}} = 1 - \frac{\lambda_{pump}}{\lambda_{ph}} \quad (2.15)$$

The resonance condition described above only applies to one particular λ_{ph} and deviations strongly affect the VECSEL's performance⁵⁸. However, the LCF as well as the material gain exhibit a red shift with increasing temperature and their shift rates differ⁵⁹. A so-called detuning between the room temperature gain and LCF peak wavelength is deliberately introduced in order to ensure resonance under operating conditions. The actual estimation of the detuning is typically carried out using the room temperature photoluminescence peak wavelength under low-density excitation conditions λ_{PL} , because its experimental determination is independent of the threshold charge carrier density in the QWs. The formal definition of the detuning is given in Eq. (2.16) and negative values are typically chosen in case of regular QWH active regions.

$$\lambda_{det} = \lambda_{PL} - \lambda_{\Gamma_z} \quad (2.16)$$

The description given above only applies to one particular design concept for VECSELs. An excellent review of the underlying physics and design considerations is provided by Tropper and Hoogland⁶⁰ and a more detailed description and investigation of the devices presented in this thesis is given by Möller⁶¹.

2.2.3 Loss channels

So far, non-radiative recombination channels were only briefly introduced in Eq. (2.5) and phenomenologically described by internal losses in Eq. (2.8a). It is clear that these processes should be prevented in order to obtain highly efficient laser systems since no photons, which can actually contribute to the amplification process, are generated. However, it is important to understand the mechanisms behind these loss processes in more detail in order to be able to engineer the band structure in such a way that they are suppressed or attenuated. The following summary explains some of the most important loss processes in semiconductor lasers. It is by no means comprehensive and effects, such as surface- and interface-related recombination processes, are neglected since they only tend to play a minor role in gain-guided broad-area edge-emitting devices. It rather focuses on fundamental loss mechanisms related to the band structure and the quality of the materials used in this study.

2.2.3.1 Charge carrier leakage

It is typically desired to operate semiconductor lasers at room temperature or above since cooling requires additional energy which would decrease the wall-plug efficiency of a device.

However, elevated temperatures may also result in charge carrier leakage from a QW active region into the barriers^{8,62} as schematically illustrated in Fig. 2.7, where ΔE_C and ΔE_V denote the hetero band offsets in the conduction and the valence band, respectively. As leakage occurs over hetero barriers, a suitable countermeasure is to increase these hetero barriers. In order to understand the process in more detail, one can consider Fermi–Dirac statistics for an ideal laser system, where the quasi Fermi levels correspond to the band edges of the conduction and the valence band, respectively. The Fermi–Dirac distribution is given in Eq. (2.17), where k_B is the Boltzmann constant, T is the temperature and E is the energy.

$$f_{FD}(E, T) = \frac{1}{\exp\left(\frac{E}{k_B \cdot T}\right) + 1} \quad (2.17)$$

The Fermi–Dirac distribution resembles a mirrored Heaviside step function at a temperature of $T = 0$ K. As the temperature is increased, the sharp transition between a thermal occupation probability of 100 % and 0 % is smeared. A thermal energy contribution at room temperature of $E_{th,RT} = 25$ meV is deduced assuming room temperature of $T_R = 20$ °C. The hetero barriers are often given as multiples of $E_{th,RT}$ as a reference level and typical values of $4 E_{th,RT}$ are desired in order to obtain thermally stable laser systems. This value is justified since $f_{FD}(E, T)$ drops to 1.8 % in case of room temperature and 3.6 % at a temperature of $T = 85$ °C resulting in a minor contribution of charge carrier leakage. However, if a hetero barrier of only $1 E_{th,RT}$ is considered, $f_{FD}(E, T)$ only drops to about 26.9 % at room temperature resulting in a considerable contribution of charge carrier leakage for any given operating temperature.

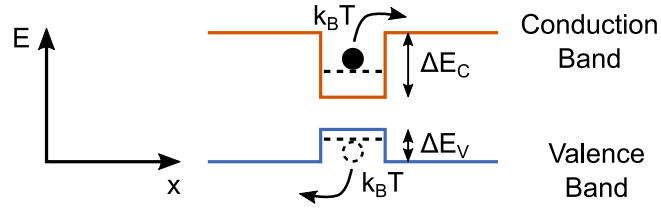


Figure 2.7: A schematic illustration of charge carrier leakage of electrons and holes over hetero barriers ΔE_C and ΔE_V , respectively, is given. The energy required for this process is provided thermally and can be estimated as $E_{th} = k_B \cdot T$

While these considerations illustrate the importance of a suitable hetero barrier design, it is important to note that the explanation given above has to be considered as a qualitative description. Additional contributions have to be taken into account in order to obtain a quantitative description of charge carrier leakage. These contributions include the densities of states of the QW and the barrier, quantization energies, and the dissimilar effective masses and hetero barriers of electrons and holes.

2.2.3.2 Shockley–Read–Hall recombination

Shockley–Read–Hall recombination was first described by Shockley and Read⁶³ and Hall⁶⁴. It is a trap-assisted recombination process involving intermediate states in the band gap of the materials used in the device. The trap-states are typically deep defect states resulting from defects or impurities. Shockley–Read–Hall recombination was originally assumed to be a non-radiative recombination mechanism, where electrons from the conduction band fall back into the valence band via the trap state. Energy and momentum conservation are satisfied by the emission of phonons in this case. Trap-assisted radiative recombination was also observed⁶⁵ and included into the theoretical model⁶⁶. It is important to note that trap-assisted radiative recombination is undesired in most optoelectronic devices and thus, also has to be considered as a loss mechanism since it does not contribute to the laser mode. Due to this variety of different recombination scenarios, the transitions are indicated by zigzag arrows in the schematic illustration of Shockley–Read–Hall recombination in Fig. 2.8. The optimization of epitaxy processes resulted in the possibility to fabricate almost defect-free heterostructures that contain only small amounts of impurities. Nevertheless, especially dilute-nitride materials may still be affected⁶⁷. Therefore, Shockley–Read–Hall recombination mainly contributes to the threshold current since the remaining amount of defect states is limited and can be saturated.

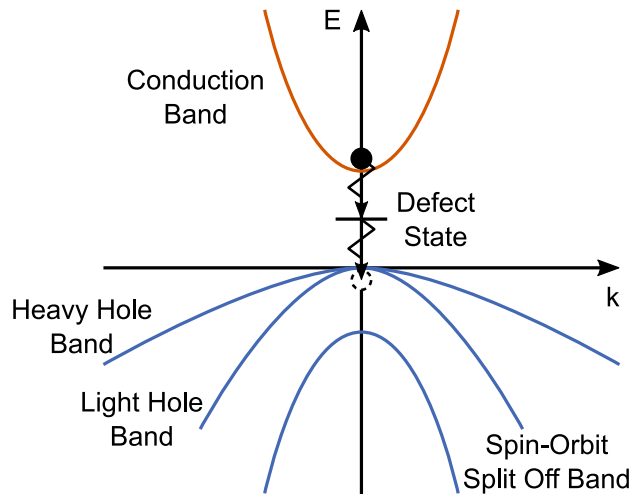


Figure 2.8: Recombination of charge carriers occurs via a defect state in case of Shockley–Read–Hall recombination. The transitions involved in Shockley–Read–Hall recombination may be radiative or non-radiative and therefore, they are indicated as zigzag arrows in order to indicate that energy and momentum conservation need to be satisfied via the emission of phonons and/or photons.

2.2.3.3 Inter-band absorption

Another intrinsic loss process, which is defined by the band structure, is inter-band absorption (IBA). IBA describes the absorption of a photon based on a transition of an excited charge carrier to a higher energy level. Assuming that only a photon and an

excited charge carrier are involved, IBA processes occur vertically in reciprocal space. They are divided into inter-conduction band absorption (ICBA) and inter-valence band absorption (IVBA), depending on whether they involve an excited electron or hole as shown in Fig. 2.9. ICBA (cf. Fig. 2.9, process 1) is typically neglected since the photon energy, which corresponds to the band gap energy of the active material, is not sufficient in order to excite an electron to the next free band and momentum conservation prevents the excitation to energetically higher states in the conduction band⁶⁸. Due to the more complex structure of the valence band, three different IVBA processes are possible (cf. Fig. 2.9, processes 2 – 4). Their occurrence strongly depends on the energy of the incident photon for a given valence band structure. Experimental studies of telecommunication lasers emitting in the near-infrared wavelength regime indicate that IVBA affects the performance of these devices^{69,70}. IVBA between the light hole band and heavy hole band (cf. Fig. 2.9, process 2) is considered to be irrelevant since the transition energies are too small for all states in the heavy hole band which exhibit a sufficiently high hole occupation probability⁷¹. The same applies to the transition between the spin-orbit split off band and the light hole band (cf. Fig. 2.9, process 3) because the density of states and the occupation probability of possible final states in the light hole band are too low⁷¹. IVBA between the spin-orbit split off band and heavy hole band (cf. Fig. 2.9, process 4), however, is enabled by the large density of states and hole occupation probability of possible final states in the heavy hole band.

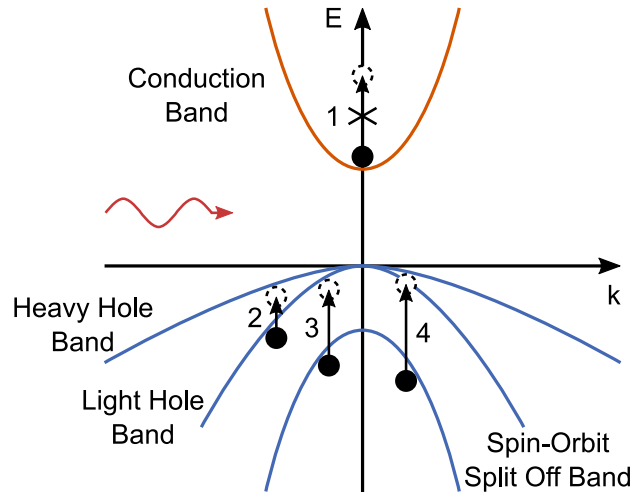


Figure 2.9: IBA processes occur when an incident photon is absorbed and the released energy is used to excite an already excited carrier to an energetically higher state. They include ICBA (1) as well as IVBA (2 – 4). ICBA is typically neglected due to a lack of appropriate final states.

A possible countermeasure is to engineer the strain of the active material in such a way that the strain-induced changes in the valence band prohibit IVBA⁷². Further absorptive loss processes include phonon-assisted IVBA⁷³ and transitions between energy bands and

impurity levels⁶⁹, which need to be considered for a more extensive description of such loss processes.

2.2.3.4 Auger recombination

Auger recombination is another intrinsic non-radiative recombination process. Auger processes are three-particle processes during which an electron–hole pair recombines. However, the energy released by this process is used to excite another charge carrier instead of emitting a photon. Thus, it is necessary that initial and final states are available which allow for simultaneous energy and momentum conservation for an Auger process to occur. The two most prominent Auger processes occurring in semiconductor lasers in the near- and mid-infrared wavelength regime are typically identified by the bands involved in the processes. Accordingly, they are referred to as conduction band – heavy hole band, conduction band – conduction band (CHCC) and conduction band – heavy hole band, spin-orbit split off band – heavy hole band (CHSH) Auger processes⁷⁴. The CHCC and CHSH Auger processes are illustrated in Fig. 2.10 a) and b), respectively.

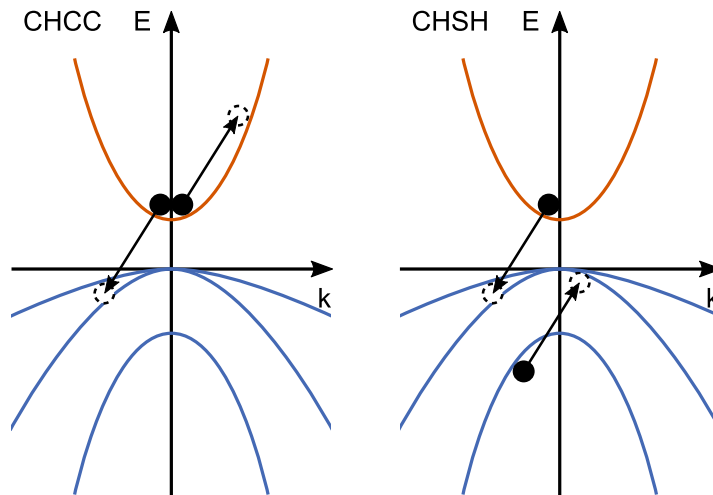


Figure 2.10: Illustration of the CHCC and CHSH Auger processes. The CHCC Auger process describes the recombination of an electron from the conduction band with a hole from the heavy hole band and the excitation of another electron from the conduction band to an energetically higher state in the conduction band. The CHSH Auger processes describes the recombination of an electron from the conduction band with a hole from the heavy hole band and the excitation of an electron from the spin-orbit split off band to the heavy hole band. Simultaneous energy and momentum conservation is required for both processes.

The theoretical description of Auger recombination proved to be difficult. Especially the assumption of parabolic bands^{75–77} is insufficient as the final states are often not sufficiently close to the Γ -point and thus, the band structures used for simulations of Auger processes are required to be more accurate^{78,79}. Auger processes are temperature dependent because the temperature-induced reduction of the band gap energy^{9,75} and the smearing of the Fermi–Dirac distribution outlined in Sec. 2.2.3.1⁴⁷.

Despite these theoretical difficulties, experimental studies indicate that Auger processes affect the performance of lasers emitting in the telecommunication regime^{2,3,5–8,67,80–82}. Experimental results indicate that the CHSH Auger process is the most dominant Auger process if the band gap energy E_g is larger than the spin-orbit split off energy ΔE_{so} which is true for telecommunication lasers^{8,47,83}. This effect becomes particularly devastating in GaSb, where E_g and ΔE_{so} are approximately in resonance⁸¹ and could be suppressed if E_g was smaller than ΔE_{so} ⁸³. The description given above neglects phonon-assisted Auger processes which are frequently discussed in the literature^{80–82,84}. Furthermore, the interplay between loss processes has to be considered in order to obtain an appropriate description⁷⁰. Even though extensive research efforts were made, the standard band structure engineering techniques do not sufficiently suppress Auger losses⁸² and alternative methods should be investigated.

2.3 Type-II heterostructures

The descriptions of light–matter interaction in Sec. 2.1 and active regions in Sec. 2.2 is based on the assumption that electrons and holes are located in one material. However, a band alignment between two materials where the energetic minima for electrons and holes are located in the same material is just one possible case. It is usually referred to as type-I band alignment and used for the fabrication of most QW systems. Typical examples for such a band alignment are the GaAs/(AlGa)As or (GaIn)As/GaAs material systems, which are frequently applied in near-infrared lasers. It is also possible to realize a situation where the conduction band minimum is located in one material and the valence band maximum is located in another material. This band alignment implies that electrons and holes are spatially separated and charge carrier recombination may occur across the interface. Such a band alignment is referred to as type-II band alignment. Examples for material systems which can exhibit a type-II band alignment are the (GaIn)As/Ga(AsSb)/GaAs¹⁶ or Ga(NAs)/(GaIn)As/GaAs⁸⁵ material systems. The third option is the existence of a broken band gap, which is also referred to as type-III band alignment. In this case the energy ranges which contain the band extrema of both materials do not overlap. An example for a material system exhibiting a type-III band alignment is the InAs/GaSb/AlSb⁸⁶ material system. A schematic illustration of type-I, -II, and -III band alignments are given in Fig. 2.11 a), b), and c), respectively. The energy bands which are typically involved in radiative transitions are marked as dashed line in case of type-I and type-II band alignments.

2.3.1 Challenges

The confinement of electrons and holes in a type-I QWH consisting of a single material typically results in a large wave function overlap of electrons and holes as illustrated

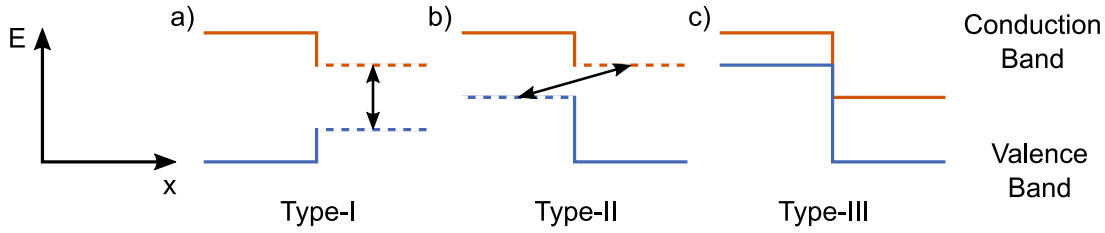


Figure 2.11: Schematic illustration of a) type-I, b) type-II and c) type-III band alignments. Charge carrier recombination in type-I and type-II material systems typically occurs between the dashed energy levels in a) and b), respectively.

in Fig. 2.4 c). Consequently, efficient radiative recombination can be expected in these systems. In case of type-II QWHs, electrons and holes are spatially separated and thus, their wave function overlap is decreased. Therefore, type-II heterostructures need to be designed thoroughly in order to obtain sufficiently large dipole matrix elements which allow for the fabrication of efficient lasers based on these material systems. While it is generally sufficient to stack two QWs to fabricate a type-II active region, it is possible to optimize the structure by embedding a hole QW in between two electron QWs resulting in an increased wave function overlap. The resulting band structure is illustrated in Fig. 2.12 together with the energetic positions of the electron and hole ground states as well as the respective wave functions. These heterostructures are also referred to as “W”-quantum well heterostructures (“W”-QWH) due to the characteristic shape of their conduction band confinement potential.

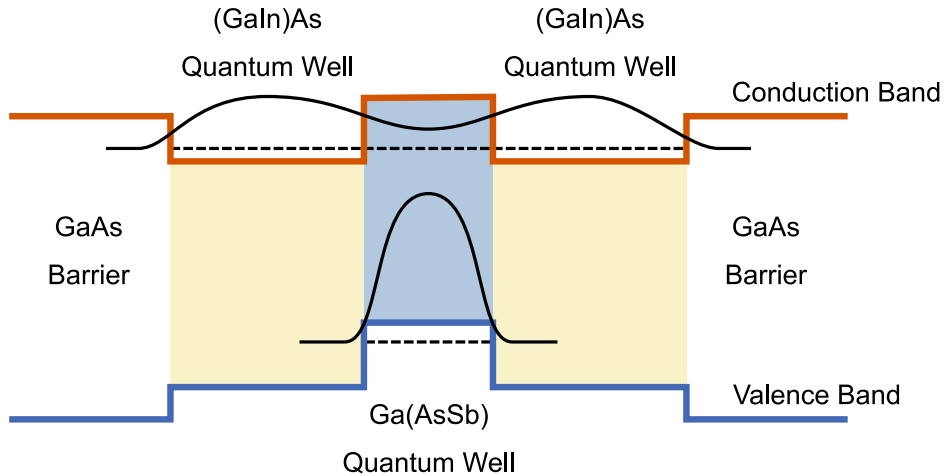


Figure 2.12: Schematic illustration of type-II “W”-quantum well heterostructure consisting of a Ga(AsSb) hole QW embedded in between two (GaIn)As electron QWs. The energetic position of the electron and the hole ground states are illustrated as dashed black lines. Furthermore, the respective wave functions are illustrated as black lines.

Another challenge is the fabrication of high-quality type-II heterostructures, because the materials which are used for the fabrication of type-II heterostructures are less established than the active materials of type-I heterostructures. Strained (GaIn)As/GaAs is frequently

applied in devices such as lasers emitting at $\lambda = 980 \text{ nm}$ ^{12–15}. It can be considered as well-established and the achievable material quality is very high resulting in narrow spectral line widths. However, strained Ga(AsSb)/GaAs is less frequently used and known to be more challenging due effects such as segregation^{87–92}. Consequently, the development of highly efficient type-II heterostructures includes the development of improved epitaxial processes for the fabrication of its constituent materials.

On the other hand, the structural complexity of the active region is increased compared to a type-I QWH. While type-I heterostructures consist of a single QW, “W”-QWHs consist of three QWs. Thus, it requires the stacking of well-defined QWs during the epitaxial growth and strain-related limitations have to be considered more thoroughly since (GaIn)As and Ga(AsSb) are both compressively strained on GaAs substrate.

2.3.2 Advantages

While the increased structural complexity outlined in Sec. 2.3.1 is challenging, it may also be considered as a chance. The confinement potentials of electrons and holes are dominated by different materials. Therefore, they can be tailored independently which introduces a new degree of freedom during the design process of an active region, because the hetero band offsets and band gap energies of each constituent material can be modified. The latter argument also applies to “W”-QWHs because theoretical models typically assume both electron QWs to have identical structural properties^{20,21,23,93–96}.

The (GaIn)As/Ga(AsSb)/(GaIn)As “W”-QWHs introduced in Sec. 2.3.1 can be grown on GaAs substrate⁹⁷ which implies that large hetero band offsets can be achieved which may be used in order to rule out charge carrier leakage as loss process and the strain may be engineered in order to prevent IVBA⁷². Additionally, an interesting feature of type-II heterostructures is the possible suppression of Auger losses. This effect is theoretically predicted for devices emitting in the mid-infrared wavelength regime^{10,98} and experimental investigations indicate a successful application¹¹. It results from the possibility to independently tune the energetic position of electrons and holes as well as their effective masses as outlined in Sec. 2.1. However, Auger recombination was never studied in case of type-II lasers emitting in the near-infrared wavelength regime due to a lack of efficient devices that can be used for these studies.

It is also important to mention that the illustration of the band structure of a “W”-QWH given in Fig. 2.12 only applies for perfectly abrupt QWs in the limit of low excitation densities. As soon as the bands are filled with spatially separated electrons and holes, band bending effects, which result in a charge carrier density dependency of the wave function overlap between electrons and holes, occur. Consequently, the wave function overlap increases as a function of charge carrier density and the gain values of type-II “W”-QWHs are predicted to be similar to gain values obtained using type-I heterostruc-

tures. Furthermore, the band bending effect results in a characteristic blue shift of the luminescence and the gain spectra^{20,21,96}.

CHAPTER 3

Experimental methods

3.1 Metal organic vapor phase epitaxy (MOVPE)

Efficiency and reliability are introduced as important characteristics of semiconductor lasers in Sec. 2.2. In order to achieve these properties, it is necessary to fabricate almost defect- and impurity-free heterostructures. Additionally, the interfaces between the constituent materials need to be well-defined in order to obtain high-quality quantum wells with layer thicknesses of only few nanometers. The general method of choice is epitaxy. The term epitaxy comes from the greek words epi (“above”) and taxis (“an ordered manner”). Metal organic vapor phase epitaxy (MOVPE) and molecular beam epitaxy (MBE) are typically applied when the quality requirements are as strict as mentioned above. MOVPE is applied in the present thesis since it is typically utilized for the industrial production of semiconductor devices. However, both methods have distinctive advantages and could be used for the growth of (GaIn)As/Ga(AsSb)/(GaIn)As “W”-QWHs, which are introduced in Sec. 2.3. The following description of a growth process focuses on microscopic processes occurring during the MOVPE growth of a heterostructure.

The name MOVPE results from the metal organic precursors used in this process, which are transported to the growth surface in the vapor phase. The sample growth is carried out in an Aixtron AIX 200 GFR (Gas Foil Rotation[®]) reactor system using high-purity hydrogen as carrier gas for the precursor transport. The reactor pressure is set to $p_R = 50$ mbar and a total gas flow of $f_{\text{tot}} = 6.81/\text{min}$ is used. Triethylgallium (TEGa), trimethylaluminum (TMAI), and trimethylindium (TMIn) are used as group-III, tertiarybutylarsine (TBAs), tertiarybutylphosphine (TBP), and triethylantimony (TESb) are used as group-V, and tetrabromomethane (CBr_4) as well as diethyltellurium (DETe) are used as dopant sources. The sample growth is carried out at typical growth temperatures between $T_g = 500$ and 625°C on semi-insulating or n-doped GaAs (001) ($\pm 0.1^\circ$) substrates in case of type-II heterostructures and lasers, respectively.

A schematic overview of processes occurring during the MOVPE growth is given in Fig. 3.1. The growth process is initiated by the transport of precursors to the growth surface

(1). They start to decompose due to the thermal energy, which is available at the above mentioned growth temperatures (2). Elementary group-III, group-V and dopant atoms are adsorbed (3) and start to diffuse on the surface (4) until they are eventually incorporated into the crystal (5). Additionally, the growth temperature may result in bulk diffusion of atoms (6) and atoms, which are not incorporated into the solid, may segregate (7) resulting in non-abrupt interfaces. These processes are sometimes undesired, but cannot be fully prevented. Therefore, the optimization of epitaxial processes aims at controlling these processes to a degree that enables the fabrication of efficient heterostructures. Surface reactions may occur in addition to gas phase reactions. They include the saturation of waste products (8) but other reactions such as the surface catalytic decomposition of precursors are possible. Any residuals, which include desorbed organic adsorbates (9), group-III, group-V and dopant atoms, which are not incorporated into the solid as well as decomposition products (10), are transported into the exhaust systems, where they are chemically bound in order to prevent environmental contamination.

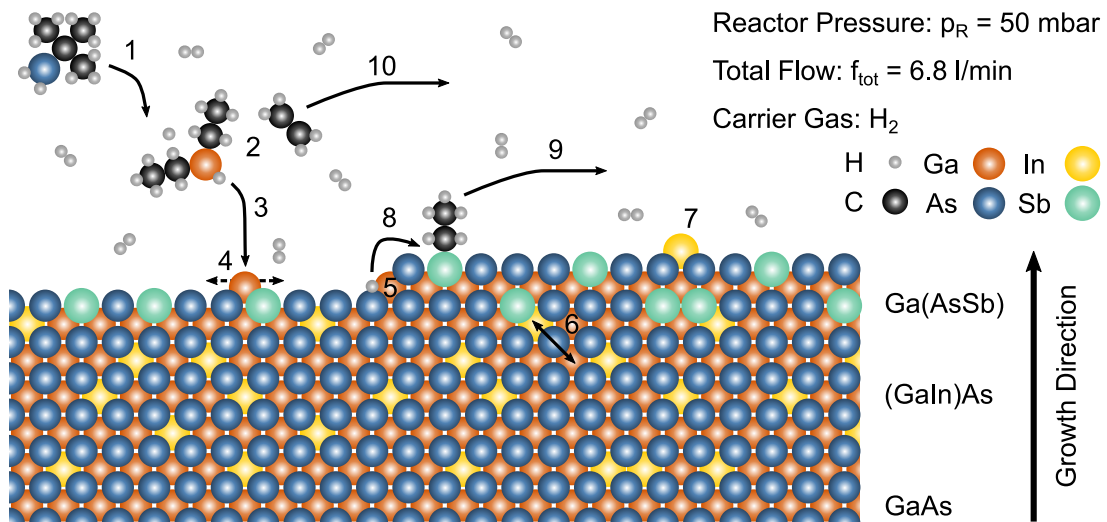


Figure 3.1: Microscopic processes occurring during the epitaxial growth of heterostructures include the transport of metal organic precursors to the growth surface (1), the decomposition of the precursors (2), the adsorption (3), and diffusion (4) of atoms on the growth surface and their incorporation into the solid (5). Atoms, which are already incorporated into the solid, may diffuse in the bulk material (6) and atoms, which are not incorporated into the material, may segregate on the growth surface (7). Furthermore, surface reactions (8) may occur, adsorbates may desorb (9), and waste products are transported into the exhaust system (10).

Another important characteristic of epitaxial growth is the stability and the reproducibility of epitaxial processes. Therefore, it is for example necessary to be able to precisely control the amount of precursor materials transported to the reactor system. An excellent in-depth description of the technique is given by Stringfellow⁹⁹.

3.2 High resolution X-ray diffraction (HR-XRD)

Especially the growth of highly resonant structures such as VECSELs requires the exact control of optical layer thicknesses. Therefore, it is necessary to be able to analyze the material thicknesses and compositions based on given growth conditions. High-resolution X-ray diffraction (HR-XRD) is a non-destructive technique that enables the structural characterization of heterostructures. It is carried out in a Panalytical X'Pert Pro HR-XRD system using the Cu $K\alpha_1$ line. The wavelength of the Cu $K\alpha_1$ line is $\lambda_{\text{XRD}} = 0.154\,05\text{ nm}$ ¹⁰⁰, which enables diffraction experiments for crystals with the lattice constants given in Tab. 2.1. The distance between two lattice planes defined by Miller indices h , k and l is given by Eq. (3.1) in case of cubic crystal structures with a lattice constant a ¹⁰¹.

$$d_{(hkl)} = \frac{a}{\sqrt{h^2 + k^2 + l^2}} \quad (3.1)$$

HR-XRD measurements of the ω - 2ϑ diffraction patterns around the (004)-reflection are carried out. In this geometry, ω is the angle between the incident monochromatic X-rays and the crystal plane that is chosen for the experiment and 2ϑ , which corresponds to 2ω , is the angle between the incident monochromatic X-rays and the detector. The difference of the path length of monochromatic X-rays reflected by a given plane and its nearest neighboring plane is defined as δs . The measurement geometry for the case of the substrate is illustrated on the left-hand side of Fig. 3.2, where the index s indicates that the geometry of HR-XRD in the substrate material is illustrated.

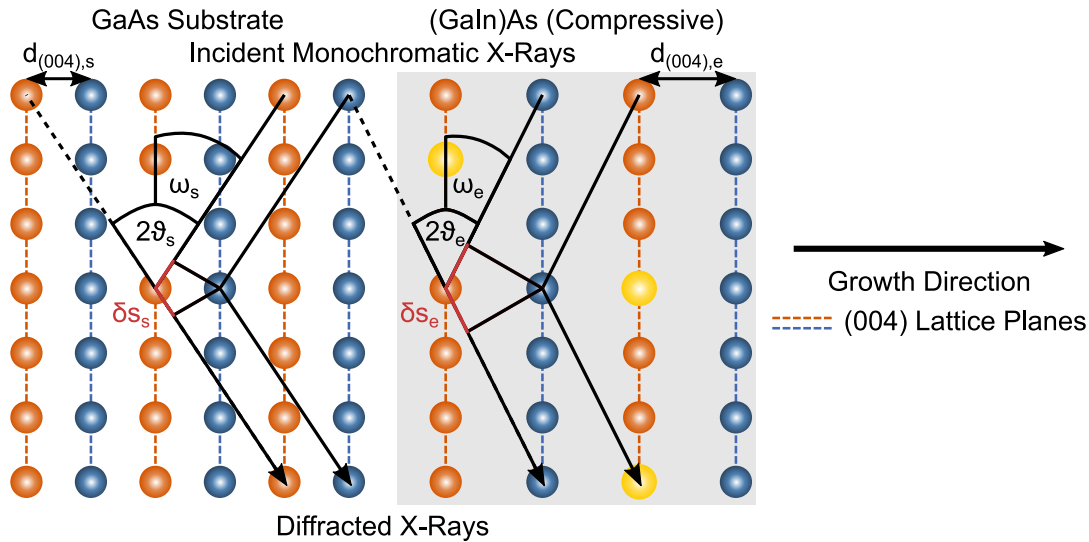


Figure 3.2: Schematic illustration of ω - 2ϑ HR-XRD measurements around the (004)-reflection of GaAs for the unstrained substrate material (left-hand side) and a strained epitaxial (GaIn)As layer (right-hand side). The Bragg angles of the substrate and the epitaxial layer differ due to the larger relaxed lattice constant of (GaIn)As as well as tetragonal distortion. Consequently, the peak positions in the HR-XRD pattern are different, which allows for a quantitative evaluation of the epitaxial layer's structural properties.

The difference of the path lengths δs has to match the wavelength of the X-rays λ_{XRD} used for the experiment (cf. Eq. (3.2a)) in order to obtain constructive interference. The angle under which Eq. (3.2a) is fulfilled can be calculated using Bragg's law, which is given in Eq. (3.2b), where $n \in \mathbb{N}$ is the diffraction order. Consequently, a peak in the diffraction pattern will occur at this angle.

$$\delta s = \lambda_{XRD} \quad (3.2a)$$

$$2 \cdot d \cdot \sin(\vartheta) = n \cdot \lambda_{XRD} \quad (3.2b)$$

The relaxed lattice constant of ternary alloys based on the binary materials introduced in Tab. 2.1 is assumed to be a linear combination of the constituent materials. This behavior is mathematically expressed in Eq. (3.3) and referred to as Vegard's law.

$$a(M_{1-x}^A M_x^B) = (1-x) \cdot a(M^A) + x \cdot a(M^B) \quad (3.3)$$

The relaxed lattice constant of the alloy is the lattice constant that is observed in case of an infinitely large bulk crystal. However, the heterostructures investigated in the present thesis are pseudomorphically grown on GaAs substrate. This means that the alloy's lattice constant in the growth plane a_e^{\parallel} is defined by the substrate's lattice constant a_s . The alloy's lattice constant perpendicular to the growth plane a_e^{\perp} is either larger or smaller than its relaxed lattice constant depending on whether its relaxed lattice constant is larger or smaller than the substrate's lattice constant. This effect is referred to as tetragonal distortion¹⁰². Alloys with larger relaxed lattice constants compared to the substrate's lattice constant are said to be compressively strained while alloys with smaller relaxed lattice constants compared to the substrate's lattice constant are said to be tensilely strained. Tetragonal distortion results in an altered condition for constructive interference as illustrated on the right-hand side of Fig. 3.2. In case of the compressively strained epitaxial (GaIn)As layer, which is denoted by the index e, the distance between the (004) lattice planes in (001) direction is increased. Thus, the corresponding Bragg angle obtained from Eq. (3.2b) is smaller than the Bragg angle obtained for the substrate and a second peak in the HR-XRD pattern is observed. Characteristic quantities for the description of the difference between the lattice constants of a substrate and an epitaxial layer are the strain ε and the lattice mismatch $\frac{\Delta a}{a_s}$, which are defined in Eqs. (3.4a) and (3.4b), respectively. They can be obtained from HR-XRD patterns by considering tetragonal distortion using the elastic constants C_{11} and C_{12} ⁴⁸.

$$\varepsilon = \frac{a_s - a_e^{relaxed}}{a_e^{relaxed}} \quad (3.4a)$$

$$\frac{\Delta a}{a_s} = \frac{a_e^{relaxed} - a_s}{a_s} = \frac{C_{11}}{C_{11} + 2 \cdot C_{12}} \cdot \frac{a_e^{\perp} - a_s}{a_s} \quad (3.4b)$$

Additional features in HR-XRD patterns arise when more layers are added due to multiple interference processes occurring in such structures. Alloy compositions and layer thicknesses are obtained by fitting a full dynamical X-ray model to the experimental results^{103,104}. This approach allows for a full characterization of the above mentioned properties, because the heterostructures investigated in the present thesis are composed of binary and ternary materials.

3.3 Photoluminescence (PL) spectroscopy

The structural information provided by HR-XRD measurements are important parameters for the design of optoelectronic devices. However, they do not necessarily provide an appropriate feedback regarding the optical efficiency of a device since defects and impurities may not have a major impact on HR-XRD patterns. A standard method that is used to gather these information is CW photoluminescence (PL) spectroscopy. PL spectroscopy is a non-destructive method where the sample is excited using a laser. If the energy of the photons emitted by the excitation laser E_{exc} is only sufficiently high for the excitation of charge carriers in the active region, the excitation is said to be resonant. If E_{exc} is also large enough to excite charge carriers in the barrier, it is said to be non-resonant. Fig. 3.3 illustrates microscopic processes occurring during a PL spectroscopy measurement of a type-II (GaIn)As/Ga(AsSb)/(GaIn)As “W”-QWH in case of a non-resonant excitation scheme. The majority of charge carriers are excited in the barrier material, because it is typically considerably thicker than the active region. The excited charge carriers quickly relax towards their energetic minima as intraband and intersubband scattering rates are higher than spontaneous emission rates¹⁰⁵. Therefore, the PL signal based on spontaneous emission of photons (cf. Sec. 2.1) results from transitions between the quantized electron and hole states in the active region. Excitation conditions are chosen in such a way that additional contributions such as sample heating due to the quantum defect between the exciting and the emitted photons do not contribute to the spectra.

The PL setup used for the experiments presented here is - if not otherwise stated - a custom-built setup in which a frequency-doubled Nd:YAG laser (Laser Quantum Opus 532, $P_{\text{max}} = 6 \text{ W}$) is used as excitation source. It is fed through a prism monochromator (Spectrolab Laserspec III) in order to filter out the fundamental laser mode at $\lambda = 1064 \text{ nm}$. The excitation power of the resulting beam ($\lambda_{\text{exc}} = 532 \text{ nm}$) is controlled using a photodetector (Coherent Model 212) in combination with a 1:1000 attenuator and a powermeter (EΦMR LM-04a). A grey scale is used to adjust the laser power to the desired power level and the beam is chopped (Stanford Research Systems SR540) before it is used to excite the sample, which is mounted in a cryostat. The resulting PL signal is coupled into a grating monochromator (Jobin-Yvon THR 1000) using an achromatic lens with a focal length of $f_c = 120 \text{ mm}$ to collimate the PL signal and a second achromatic lens

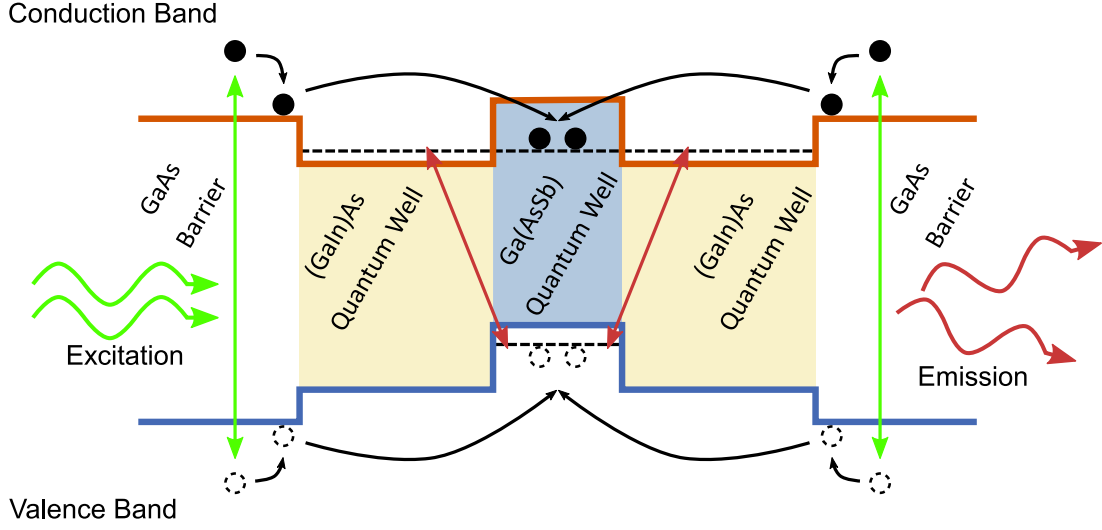


Figure 3.3: PL spectroscopy is a method that can be used for the optical characterization of samples. The sample is excited using a laser. The charge carriers relax into their energetic minima and spontaneous emission between the quantized states in the active region is observed.

with a focal length of $f_f = 400$ mm to focus the PL signal onto the entrance slit of the monochromator. A long pass filter with a cutoff frequency of $\lambda_{co} = 570$ nm is introduced to prevent that scattered laser light from the excitation source enters the monochromator and thus, to prevent the detector from being saturated or even destroyed. The monochromator is computer-operated via a controller and the resulting monochromatic signal is guided through a second slit before it is detected using a liquid nitrogen cooled Ge detector (Applied Detector Corporation 403L) in combination with a lock-in amplifier (Stanford Research Systems SR510) in order to improve the signal to noise ratio. The chopper frequency serves as reference for the lock-in amplifier and the measured value is acquired using a computer. The spectral range covered by this setup is defined by the sensitivity of the Ge detector and reaches from approximately 700 to 1700 nm. Additionally, the PL measurements can be carried out for sample temperatures ranging from $T_s \approx 10$ to 400 K. The setup is illustrated in Fig. 3.4.

PL spectra can be used to draw conclusions regarding the sample quality since defects and disorder may result in non-radiative recombination and an energetic broadening of the energy states. High peak intensities and small linewidths are desired since they are a hint towards high sample qualities. Furthermore, the emission wavelength of a given active region can be determined and conclusions regarding the electronic structure of the active region may be drawn since multiple transitions may be involved in the spontaneous emission process⁹⁶. However, it is important to note that PL spectra need to be analyzed with great care since the emission properties of active regions may be charge carrier density dependent and the exact charge carrier density is typically unknown. This remark particularly applies to type-II heterostructures, where band bending effects have a great influence on the emission properties.

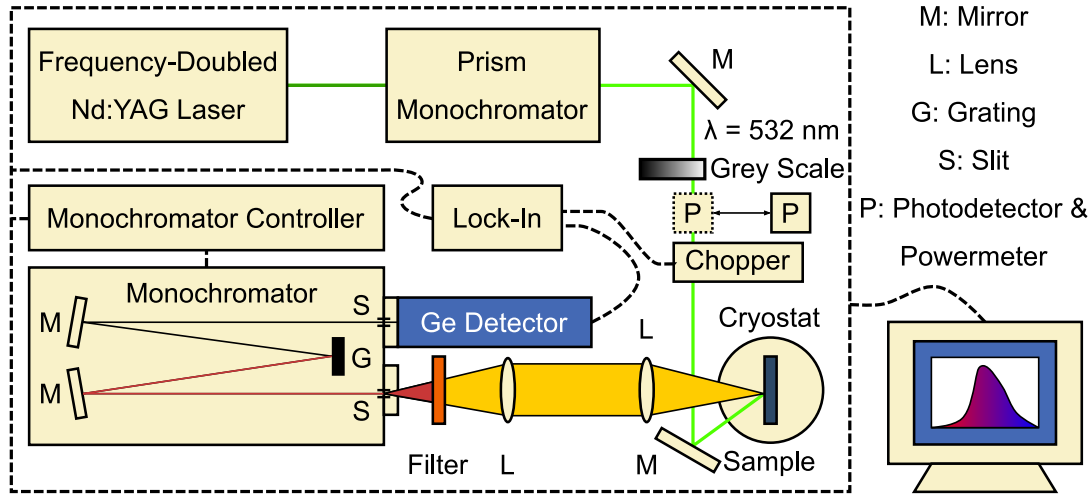


Figure 3.4: Schematic illustration of the CW PL setup used for the present experiments. The sample is excited using a frequency-doubled Nd:YAG laser and the spectral resolution is obtained using a grating monochromator. The detection of the signal is carried out using a liquid nitrogen cooled Ge detector in combination with a lock-in amplifier.

3.4 Laser studies

While optical pumping of semiconductor lasers is possible, electrical injection is required for various applications. Therefore, it is also necessary to characterize the optical properties of devices which are designed for such applications. The experimental setups required for these experiments are introduced in Secs. 3.4.1 and 3.4.2 and the theoretical model introduced in Sec. 2.2.1 is used for the evaluation of the laser characteristics.

3.4.1 Electroluminescence (EL) spectroscopy

The injection of excited charge carriers into the active region is a directional process in case of electroluminescence (EL) spectroscopy as opposed to the excitation scheme in PL experiments. Electrons and holes are injected into the the SCH from the n- and p-contact, respectively, before they start to relax into the type-II (GaIn)As/Ga(AsSb)/(GaIn)As “W”-QWH as shown in Fig. 3.5. Charge carrier recombination is dominated by spontaneous or stimulated emission depending on whether the luminescence signal is recorded below or above laser threshold, respectively.

The electrical contacts between the setup and the device are established by placing the sample with its large area n-contact on a gold coated copper mount. The p-contact is connected using a custom probe card (Semi-Probes) consisting of 25 equally spaced contact needles. The distance between two needles is as small as 100 μm in order to allow for a homogeneous current injection. A pulsed excitation scheme is used in order to prevent resistive heating of the devices. Thus, it is possible to carry out measurements using different injection currents at a fixed temperature which is adjusted using a computer-

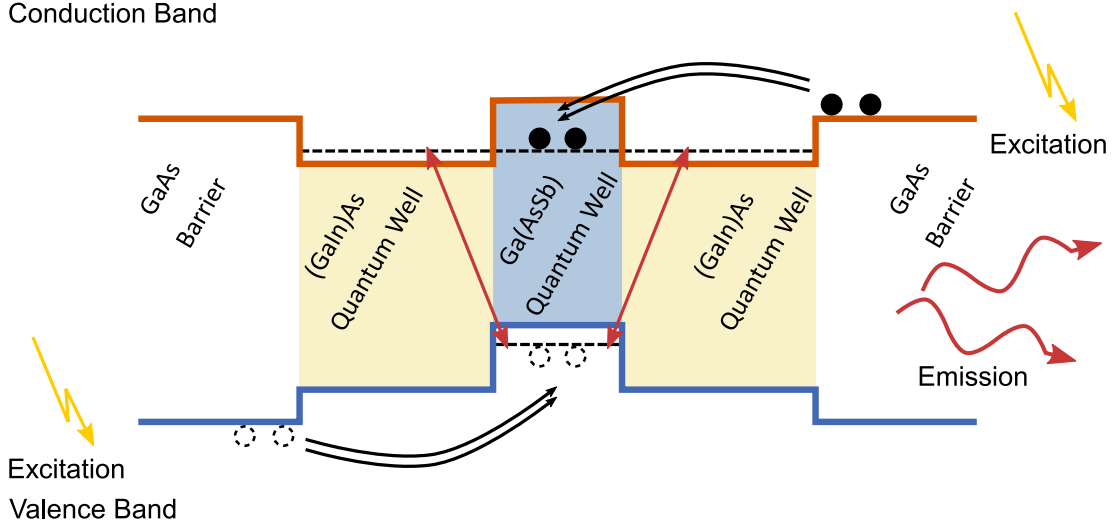


Figure 3.5: EL spectroscopy is a method that can be used for the optical characterization of samples. The sample is excited using charge carriers, which are electrically injected into the active region from the n- and the p-contact. The excited charge carriers relax into their energetic minima and spontaneous or stimulated emission between the quantized states in the active region is observed depending on whether the device is operated below or above laser threshold.

controlled Peltier element (EΦMR TEC-05-1). The setup allows temperatures between $T = 10$ and 100°C . The lower limit is chosen to prevent the condensation of air humidity and the upper limit is chosen to prevent the probe card from taking damage. The excitation pulses are generated using a pulse source (EΦMR UR19GR05). If not otherwise stated, pulse lengths of 400 ns and a pulse repetition rate of 10 kHz are used in these experiments. The signal detection is carried out using a setup that is similar to the one used for the PL experiments (cf. Sec. 3.3) in case of measurements below laser threshold. The only differences are that a long pass filter is not required and the lock-in amplifier is triggered by the pulse source.

As the laser reaches its threshold, its output power is dramatically increased while the spectral width of the EL signal is strongly decreased. Therefore, an optical spectrum analyzer (OSA, Yokogawa AQ6370B) is used to record the laser spectra because it is more suitable for the respective power levels. The EL signal is coupled into the OSA using an optical fiber in combination with a single lens. The setup is illustrated in Fig. 3.6.

The analysis of the resulting EL spectra yields the same characteristic properties as outlined in Sec. 3.3. However, it is important to note that they are affected by the cavity design while PL spectra are exclusively defined by the properties of the active region at a given charge carrier density.

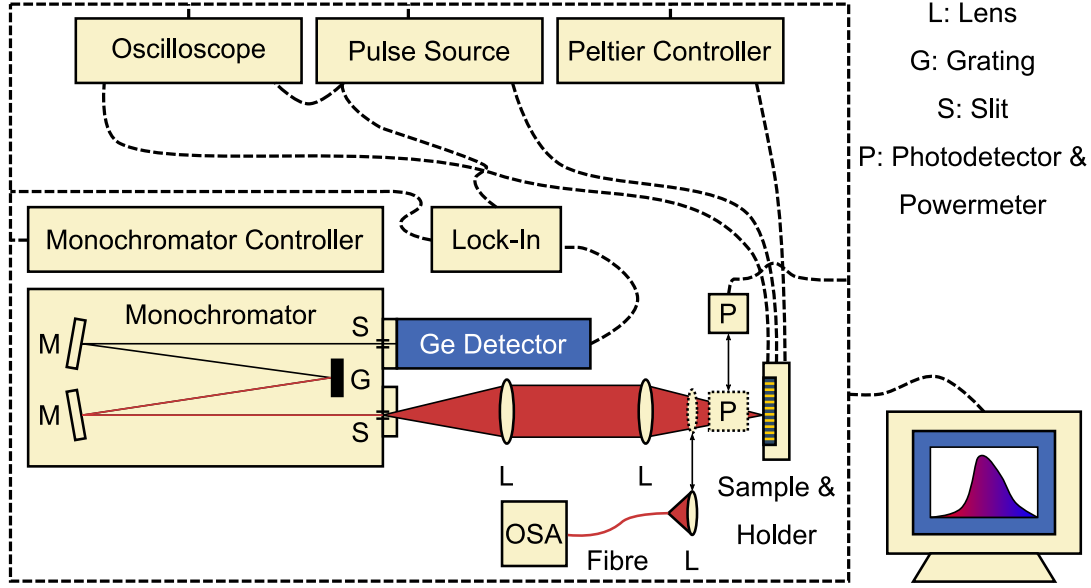


Figure 3.6: Schematic illustration of the EL setup used for the present experiments. The sample is excited using a pulse source. In case of measurements below laser threshold, the spectral resolution is obtained using a grating monochromator. The detection of the signal is carried out using a liquid nitrogen cooled Ge detector in combination with a lock-in amplifier. Measurements above laser threshold are carried out with an optical spectrum analyzer. Furthermore, it is possible to measure laser characteristics by measuring the single facet output power as a function of injection current density using a large-area Ge photodetector in combination with a powermeter and an oscilloscope.

3.4.2 Laser characteristics

The setup introduced in Sec. 3.4.1 can also be used to measure laser characteristics, i.e. the single facet output power as a function of injection current density. All laser characteristics in the present thesis are obtained using as-cleaved gain-guided broad-area edge-emitting lasers. The output power of the device is measured using a large-area Ge photodetector (Newport 818-ST2-IR) in combination with a powermeter (Newport 1835-C). The current pulses are measured using an oscilloscope (Tektronix TDS220) and the pulse height and length are experimentally determined in order to obtain the real values of the injection current density as well as the optical output pulse power. The characteristics are evaluated using the simple theory described in Sec. 2.2.1. These evaluations provide insights into the properties of actual devices consisting of a given cavity and active region.

CHAPTER 4

Results

4.1 Epitaxial growth and spectral coverage of “W”-QWHs

Various theoretical studies predict significant material gain values in the 1.3 μm wavelength regime based on (GaIn)As/Ga(AsSb)/(GaIn)As “W”-QWHs^{20,21,24,25}. However, detailed studies of type-II lasers based on bilayer QWHs²⁷ and “W”-QWHs²⁸ are only available for the 1.2 μm wavelength regime. A MOVPE growth study is carried out in order to determine whether the realization of high-quality “W”-QWHs is possible in this particular wavelength regime and to determine how far the emission wavelength can be extended into the near-infrared wavelength regime. A growth temperature of 550 °C is chosen based on detailed growth studies of (GaIn)As/GaAs and Ga(AsSb)/GaAs test structures in the wider temperature range between 500 °C and 600 °C.

The structures investigated in this growth study consist of three “W”-QWHs separated by 50 nm thick GaAs barriers and the uppermost “W”-QWH is capped by a 5 nm thick GaAs cap. Layer thicknesses of 6 nm and 4 nm are chosen for (GaIn)As and Ga(AsSb), respectively. Furthermore, the indium concentration is adjusted to 20 % using a V/III gas phase ratio of 3.9 for all samples while the antimony concentration is varied in order to determine its influence on the emission wavelength. This variation is carried out by using a fixed V/III gas phase ratio of 7.5, where $V = \text{TBA} + \text{TESb}$, while sweeping the TESb/V gas phase ratio between 0.830 and 0.870. The corresponding HR-XRD patterns are shown in Fig. 4.1 a). Well defined fringes are observed up to diffraction angles as high as $-8000''$ indicating a high structural quality of the samples. Only the sample grown with the highest TESb/V ratio exhibits a broadening of the HR-XRD fringes. A quantitative analysis of the HR-XRD patterns results in antimony concentrations between 19.3 % and 30.2 % corresponding to strain values between 1.5 % and 2.3 % depending on the TESb/V ratio. Thus, the broadening of the HR-XRD fringes described above most probably results from a strain-induced roughening of the growth surface during the growth of Ga(AsSb).

In addition to the structural characterization described above, the low-excitation density PL peak wavelengths are determined using a commercial PL mapper system (ACCENT

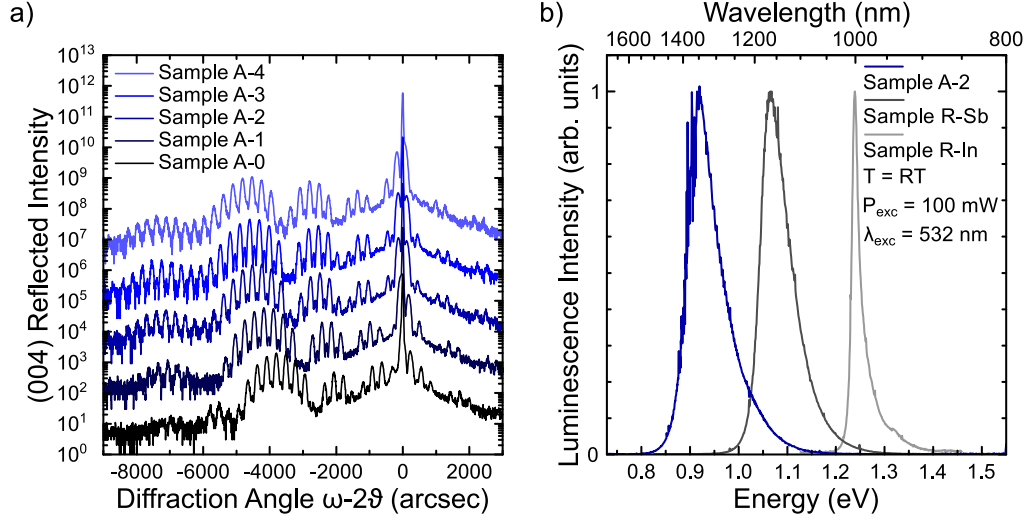


Figure 4.1: a) HR-XRD patterns of “W”-QWH samples grown at a temperature of 550 °C using a fixed V/III gas phase ratio of 7.5. The utilization of different TESb/V gas phase ratios results in antimony concentrations between 19.3 % and 30.2 %. The HR-XRD patterns of samples A-1 – A-4 are shifted on the intensity scale for clarity. b) Room temperature PL spectra of sample A-2 (“W”-QWH) as well as reference samples R-Sb (Ga(AsSb)/GaAs) and R-In ((GaIn)As/GaAs). The spectral position of the PL peak intensity of sample A-2 with respect to the reference samples indicates a type-II band alignment.

rpm2000). The measurements reveal that the antimony concentrations between 19.3 % and 30.2 % correspond to PL peak wavelengths between 1.22 μm and 1.47 μm , respectively. Thus, the “W”-QWHs presented here are spectrally well suited as active media in telecommunication lasers designed for the O-band (1.26 μm – 1.36 μm). The growth conditions as well as the structural and optical properties of the samples investigated in this study are summarized in Tab. 4.1.

Table 4.1: Overview of important growth-related, structural, and optical parameters of samples discussed in Sec. 4.1.

Sample	V/III	T_g (°C)	TESb/V	c_{Sb} (%)	ϵ_{Sb} (%)	λ (μm)
A-0	7.5	550	0.830	19.3	1.5	1.22
A-1	7.5	550	0.850	24.0	1.8	1.30
A-2	7.5	550	0.853	27.4	2.1	1.36
A-3	7.5	550	0.860	28.2	2.2	1.40
A-4	7.5	550	0.870	30.2	2.3	1.47
R-Sb	1.9	500	0.320	26.0	2.0	1.17
R-In	3.9	550	-	-	-	0.99

Further PL measurements of sample A-2 as well as (GaIn)As/GaAs and Ga(AsSb)/GaAs reference samples R-In and R-Sb are carried out using the experimental setup described in Sec. 3.3 in order to verify that the emission observed here is based on a type-II transition. Sample A-2 is chosen because of its PL peak wavelength of 1.36 μm , which is required for

emission at 1.3 μm due to the well described blue shift of type-II heterostructures (see Sec. 2.3.2). Reference samples are chosen in such a way that their structural properties are similar to the ones which are arranged as “W”-QWH in sample A-2. The resulting spectra, which are shown in Fig. 4.1 b), show that the PL peak wavelength of the “W”-QWH is clearly red shifted compared to the type-I QWH reference samples. Consequently, the type-II character of the PL emission of the “W”-QWH is proven, because this energetic arrangement indicates that energy states from both materials are involved in the emission process occurring in the “W”-QWH.

A series of samples exhibiting their PL peak wavelengths at approximately 1.36 μm reveals that the PL peak intensity is independent of the V/III gas phase ratio, which is used for the growth of Ga(AsSb). Furthermore, an average antimony concentration of approximately 27 % is required in order to obtain a PL peak wavelength of 1.36 μm . The full publication and more details concerning the MOVPE growth process can be found in Sec. 6.1.

4.2 Electrical injection lasers emitting at 1.2 μm

In order to demonstrate the suitability of “W”-QWH as active region in semiconductor lasers, electrical injection lasers designed for emission in the 1.2 μm wavelength regime are fabricated. The single “W”-QWH active region is grown under the growth conditions outlined in Sec. 4.1 using a V/III ratio of 7.5 and by adapting the TESb/V ratio for achieving a low-excitation density EL peak wavelength of 1.2 μm . The (AlGa)As claddings and the GaAs SCH as well as the GaAs cap are grown at a temperature of 625 $^{\circ}\text{C}$. Gold is chosen as contact metal in order to allow for an electrical injection of charge carriers.

The device analysis at room temperature is carried out using a laser with a cavity length of 930 μm and a cavity width of 100 μm . The EL spectra obtained from this device for current densities between 0.10 kA/cm^2 and 0.48 kA/cm^2 are shown in Fig. 4.2 a). EL spectra below laser threshold are colored in red, while spectra above threshold are colored in blue. As expected, the EL peak wavelength blue shifts below laser threshold with an average shift rate of $(93 \pm 14) \text{ meV}/(\text{kA}/\text{cm}^2)$ between 0.10 kA/cm^2 and 0.38 kA/cm^2 . However, the charge carrier density is pinned above threshold as outlined in Sec. 2.2.1 resulting in a constant emission wavelength of 1.16 μm above laser threshold.

The laser characteristic shown in Fig. 4.2 b) reveals a distinct threshold behavior at a current density of 0.4 kA/cm^2 that coincides with the mode narrowing observed in Fig. 4.2 a). Furthermore, an optical efficiency of 0.35 W/A per facet corresponding to a differential efficiency of 66 % and an optical output pulse power of 1.4 W per facet at a power supply-limited current density of 4.6 kA/cm^2 are observed. These excellent results highlight the general potential of semiconductor lasers based on a type-II band alignment and provide the opportunity to carry out an advanced analysis of “W”-QWH

active regions. The full publication including the longitudinal laser mode spectrum can be found in Sec. 6.2.

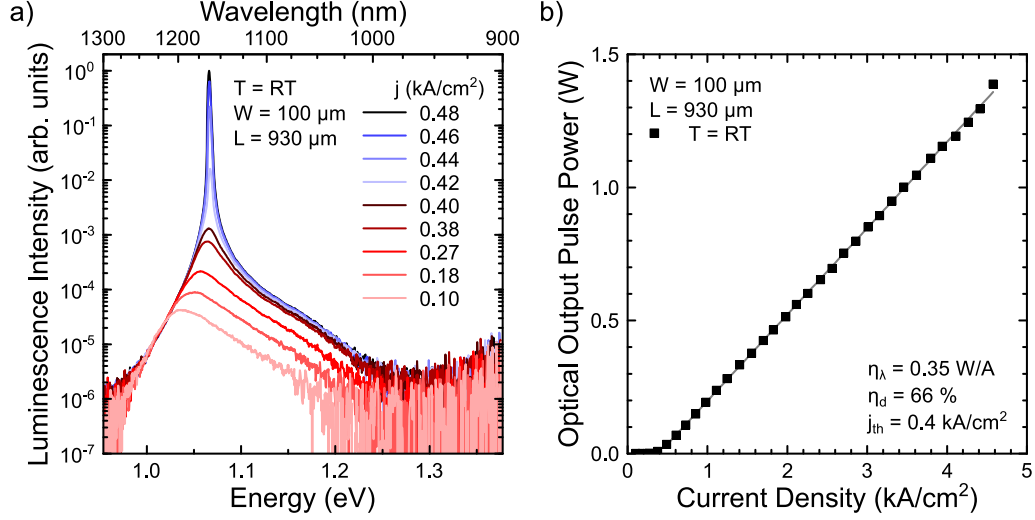


Figure 4.2: a) Current density-dependent EL spectra below and above laser threshold of a single “W”-QWH laser emitting at $1.2 \mu\text{m}$. Red spectra indicate operation below and blue spectra indicate operation above laser threshold. b) Laser characteristic of the same single “W”-QWH laser. All measurements are carried out at room temperature.

4.2.1 Temperature-dependent properties

Near-infrared semiconductor lasers are frequently utilized in areas of application where reliable operation under changing environmental conditions is a key concern. In case of fiber-optic telecommunication, it should be possible to apply a laser device up to a temperature of at least 85°C . Consequently, the following investigation aims at investigating the temperature-dependent properties of “W”-QWH lasers. These investigations are carried out using the sample introduced in Sec. 4.2 as well as another sample with a double “W”-QWH. It utilizes the same cavity design and both active regions, which are separated by a 20 nm thick GaAs barrier, are grown under the same conditions as the active region of the single “W”-QWH laser. Furthermore, a cavity length of $975 \mu\text{m}$ and a cavity width of $100 \mu\text{m}$ are chosen in order to ensure that the results of both devices are comparable. The double “W”-QWH design results in a decrease of the charge carrier density per “W”-QWH for a given current density and thus, temperature- as well as charge carrier density-induced effects can be analyzed.

EL measurements below laser threshold at room temperature reveal a similar behavior and both devices operate based on the fundamental type-II transition as shown in Fig. 4.2 a) for the single “W”-QWH laser. However, the transition between the first excited electron and hole state starts to dominate the EL spectra of the single “W”-QWH at high temperatures as shown in Fig. 4.3 a). Consequently, laser emission based on this higher order type-II transition is observed starting from temperatures of 78°C . These results

clearly indicate that the modal gain contributed by the fundamental type-II transition saturates before the total loss is exceeded at these temperatures. Excess charge carriers start to populate the higher order states until the modal gain contributed by this transition is eventually sufficient to overcome the total loss and laser operation is observed. This behavior was predicted for similar active regions operated at high charge carrier densities²¹ and its occurrence is facilitated by the small energetic separation between the electron states¹⁰⁶.

The introduction of a second “W”-QWH should increase the saturation level of the modal gain based on the fundamental type-II transition, because the modal gain is now generated by both “W”-QWHs and the optical confinement factor is increased. Consequently, no sign of higher order type-II transitions is observed in the entire investigated temperature range up to 97 °C as shown in Fig. 4.3 b). These results highlight that it is important to operate “W”-QWH lasers at suitable charge carrier densities per “W”-QWH. Furthermore, the excellent thermal stability of the double “W”-QWH points out the application potential of “W”-QWH active regions.

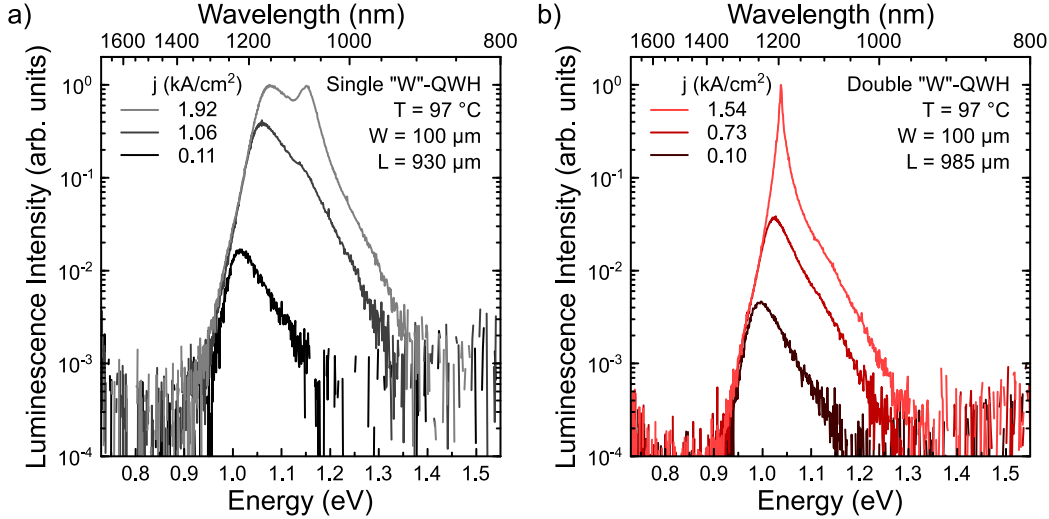


Figure 4.3: a) Current density-dependent EL spectra below laser threshold of a single “W”-QWH laser emitting at 1.2 μm . b) Current density-dependent EL spectra below laser threshold of a double “W”-QWH laser emitting at 1.2 μm . Both measurement series are recorded at a temperature of 97 °C.

While operation based on the fundamental type-II transition has to be considered as a prerequisite for the application of “W”-QWHs, temperature-induced changes of their threshold current density as well as differential efficiency are also important properties. Therefore, laser characteristics of both devices are recorded for temperatures between 11 °C and 97 °C. Both devices exhibit similar properties over the whole temperature range as shown in Fig. 4.4, where operation based on the fundamental type-II transition are indicated by filled symbols and operation based on the higher order type-II transition is indicated by open symbols. Consequently, exponential fits of these regimes yield similar

characteristic temperatures of $T_0 = (56 \pm 2) \text{ K}$ and $T_1 = (105 \pm 6) \text{ K}$ for the single and $T_0 = (60 \pm 2) \text{ K}$ and $T_1 = (107 \pm 12) \text{ K}$ for the double “W”-QWH laser. Thus, the characteristic temperatures appear to be independent of the charge carrier density per “W”-QWH. It is particularly interesting to note that the temperature-dependent behavior of the threshold current density as well as the differential efficiency is not negatively affected by the switching from the fundamental to the higher order type-II transition. This result indicates that the switching can be considered as a fundamental property of these type-II heterostructures rather than a result of material imperfections.

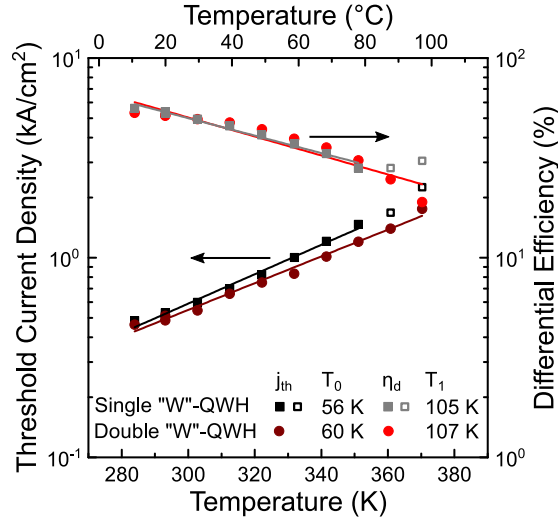


Figure 4.4: Temperature-dependence of the threshold current density and the differential efficiency of a single and a double “W”-QWH laser. Exponential fits yield characteristic temperatures of $T_0 = (56 \pm 2) \text{ K}$ and $T_1 = (105 \pm 6) \text{ K}$ for the single as well as $T_0 = (60 \pm 2) \text{ K}$ and $T_1 = (107 \pm 12) \text{ K}$ for the double “W”-QWH laser.

A further investigation of the loss mechanisms occurring in these lasers is required in order to obtain a more detailed understanding of the devices and to determine why the characteristic temperatures are rather small. However, these low values of T_0 may also be considered as particularly interesting since they could result in a canceling of the temperature-induced red shift and the charge carrier density-induced blue shift of the emission wavelength. The temperature dependence of the laser emission wavelengths of different type-II lasers as well as a type-I (GaIn)(NAs) double QWH laser emitting in the $1.2 \mu\text{m}$ regime is summarized in Fig. 4.5, where filled symbols indicate operation based on the fundamental type-II transition and open symbols indicate operation based on the higher order type-II transition. As expected, the emission wavelength of the type-I (GaIn)(NAs) double QWH laser exhibits a temperature-induced red shift of the emission wavelength and a linear fit yields a shift rate of $(0.41 \pm 0.01) \text{ nm/K}$, which is a typical value for type-I QWH laser systems. In contrast, the emission wavelength of the “W”-QWH lasers only amounts to $(0.04 \pm 0.02) \text{ nm/K}$ and $(0.17 \pm 0.01) \text{ nm/K}$ for the single and “W”-QWH laser, respectively. These values confirm that a modification of the shift rate

of the emission wavelength is possible. Additionally, the difference between the single and double “W”-QWH laser support the hypothesis that a charge carrier-density induced effect is observed. A third type-II laser, where the single “W”-QWH active region is embedded in GaP interlayers¹⁰⁷, exhibits a characteristic temperature of $T_0 = (50 \pm 3) \text{ K}$. Consequently, a negative shift rate of $(-0.10 \pm 0.04) \text{ nm/K}$ is observed.

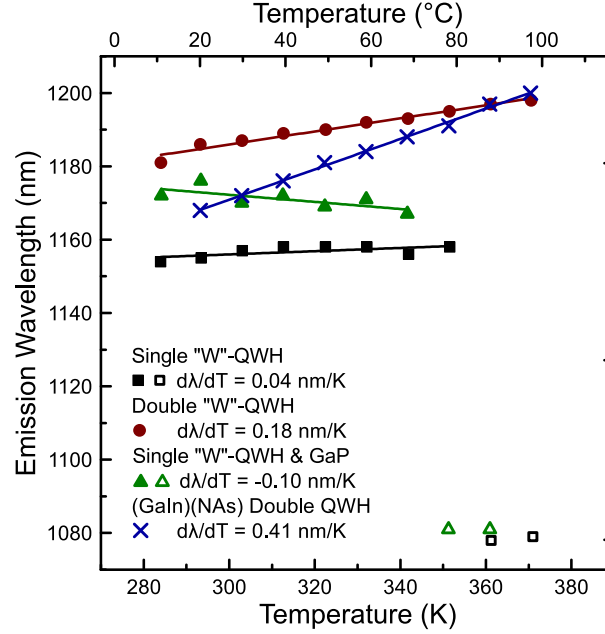


Figure 4.5: Temperature-dependence of the laser emission wavelength of the single “W”-QWH laser, the double “W”-QWH laser, the single “W”-QWH laser with GaP interlayers, and a (GaIn)(NAs) double QWH laser. Linear fits yield shift rates of $(0.04 \pm 0.02) \text{ nm/K}$, $(0.17 \pm 0.01) \text{ nm/K}$, $(-0.10 \pm 0.04) \text{ nm/K}$, and $(0.41 \pm 0.01) \text{ nm/K}$, respectively.

Thus, it is possible to modify the shift rate over a large range starting from shift rates, which are similar to type-I heterostructures, down to negative shift rates. A device-specific tailoring of the emission wavelength may result in improved characteristics of various devices and is a highly promising property of type-II heterostructures. The classical design rules, which demand large characteristic temperatures in order to decrease the power dissipation, may not be applicable to these novel device concepts, because the modifications may decrease the demand for external cooling since the laser emission wavelength remains constant irrespective of the chosen operating temperature. A manuscript describing these key properties of type-II “W”-QWH systems is under preparation and will be submitted after the clarification of possible patent applications.

4.3 VECSELs emitting at 1.2 μm

High-precision applications such as laser surgery require light sources with high beam qualities in order to be applicable. Consequently, the application of “W”-QWHs in VECSELs is investigated by incorporating the active regions introduced in Sec. 4.2 as

active region into RPGs. VECSELs based on type-I QWHs are typically designed to exhibit a negative detuning in order to account for the different temperature-induced shift rates of the cavity resonance and the material gain spectrum⁵⁹. However, the situation is more complex in case of a type-II VECSEL since the results presented in Sec. 4.2.1 show that the temperature-induced red shift can be overcompensated by the charge carrier density-induced blue shift. Thus, the type-II VECSEL presented here is designed with a positive detuning of approximately 35 nm in order to account for the charge carrier density-induced blue shift of the material gain. While this configuration is detrimental for type-I VECSELs, it leads to a slope efficiency of 7.6 %, a maximum optical output power of 4.0 W, and a threshold pump intensity of 1.2 kW/cm² at a heat sink temperature of -15°C as shown in Fig. 4.6 a). Even though these properties deteriorate with increasing temperature, the device can be operated up to heat sink temperatures of at least 30°C which is promising for applications under ambient conditions. Nevertheless, further studies are required to determine the factors limiting the device performance in order to improve the slope efficiencies of these devices.

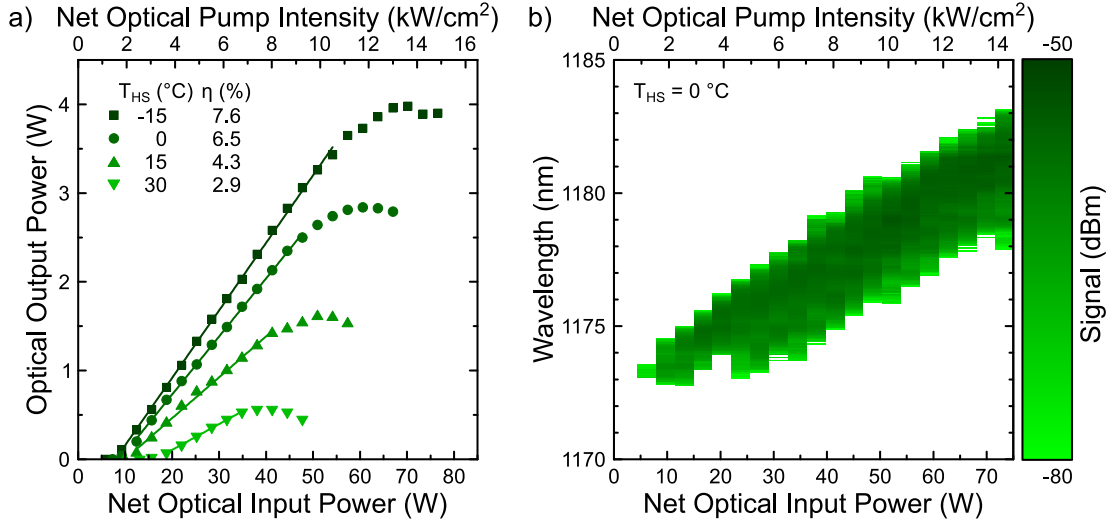


Figure 4.6: a) Temperature-dependent VECSEL characteristics for heat sink temperatures ranging from -15°C to 30°C . b) Pump power-dependent EL spectra above laser threshold for a heat sink temperature of 0°C .

As outlined in Sec. 4.2, the spectral response to an increasing pump density may vary below and above laser threshold. While a considerable blue shift of the emission peak is observed below threshold, the emission above threshold red shifts for an increasing net optical input power as shown in Fig. 4.6 b) for a heat sink temperature of 0°C . This behavior can be explained by considering a pinned charge carrier density preventing a further blue shift of the system for a given temperature of the active region. The temperature of the active region is increased due to the quantum defect between the pump light and the laser emission resulting in a red shift of the LCF. Furthermore, the material gain may shift red or blue depending on whether the temperature-induced red shift of the

band gaps or the loss-induced blue shift due to an increase of the charge carrier density as a function of net optical input power dominates. However, broad material gain spectra are predicted for the “W”-QWH active regions⁹⁶ and narrow LCF peaks are obtained using this resonant design¹⁰⁸. These findings indicate that the red shift of the LCF dominates the modal gain. The full publication including a more detailed discussion of the design characteristics of the present VECSEL based on a type-II “W”-QWH active region can be found in Sec. 6.3.

4.4 Electrical injection lasers emitting at 1.3 μm

Another important optimization is the tailoring of the emission wavelength of semiconductor lasers. A particularly interesting wavelength regime is the O-band (1.26 μm to 1.36 μm) which is used for fiber-optic telecommunication. The growth conditions of the cavity, which were outlined in Sec. 4.2, remain unchanged and the double “W”-QWH design is chosen in order to prevent the temperature-induced switching to higher order type-II transitions. Furthermore, the microscopic theory described by Berger et al.⁹⁶ is used to optimize the active region in order to improve its gain characteristics. This design study suggests the application of 4 nm thick (GaIn)As and Ga(AsSb) QWs containing 28 % indium and antimony, respectively. This design is predicted to improve the peak gain value by 66 % for a given charge carrier density of $3.0 \times 10^{12}/\text{cm}^2$ compared to a reference sample consisting of 6 nm thick (GaIn)As and 4 nm thick Ga(AsSb) QWs containing 22 % indium and 28 % antimony, respectively.

The following results verify the first realization of a type-II “W”-QWH laser in this technologically important wavelength regime (see also Sec. 6.4 for the full submitted manuscript). EL measurements below and above laser threshold of a 975 μm long and 100 μm wide device reveal that laser operation based on the fundamental type-II transition is achieved at room temperature. A further investigation of the EL signal above laser threshold for temperatures between 10 °C and 100 °C confirms this finding over the whole temperature range. The laser mode shifts from 1.272 μm to 1.296 μm corresponding to a shift rate of $(0.28 \pm 0.01) \text{ nm/K}$ as the temperature is increased, because the charge carrier density-induced blue shift does not compensate the temperature-induced red shift due to the double “W”-QWH design as shown in Fig. 4.7 a).

The device exhibits a threshold current density of 1.0 kA/cm², a differential efficiency of 41 %, and a power-supply limited maximum optical output pulse power of 0.68 W per facet at a temperature of 20 °C as shown in Fig. 4.7 b). Laser characteristics are recorded for the whole temperature range mentioned above and an optical output pulse power of 0.18 W per facet is achieved at a temperature as high as 100 °C. Exponential fits reveal characteristic temperatures of $T_0 = (132 \pm 3) \text{ K}$ and $T_1 = (109 \pm 12) \text{ K}$. A comparison of these characteristic temperatures with literature values of InP-based material systems is difficult, because they depend on the actual device design⁴. Typical T_0 values

reported in the literature are 50 K – 80 K and 100 K – 120 K for (GaIn)(AsP)/InP² and (AlGaIn)As/InP³⁻⁷, respectively. These excellent results show that type-II “W”-QWH lasers can be operated at typical operating conditions of telecommunication lasers, which are required to operate up to 85 °C. Furthermore, they enable the investigation of the role of Auger recombination in these devices and the integration of these active regions in device designs that enable their application in actual telecommunication systems in the future.

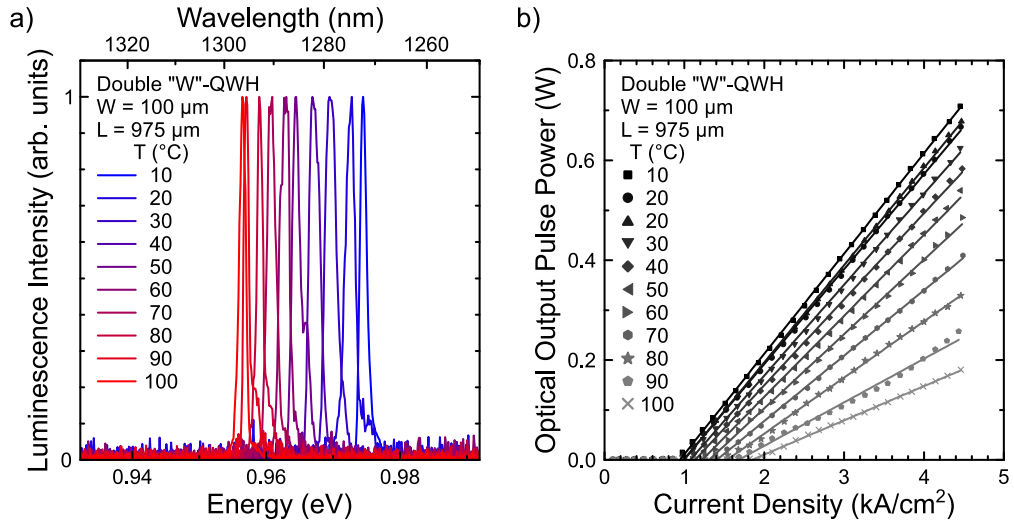


Figure 4.7: a) Temperature-dependent EL spectra above laser threshold of a double “W”-QWH laser emitting at 1.3 μm. Laser operation based on the fundamental type-II transition is observed in the entire temperature range. b) Temperature-dependent laser characteristics of the same double “W”-QWH laser. Both measurement series are carried out for temperatures ranging from 10 °C to 100 °C.

CHAPTER 5

Conclusion and outlook

The present investigation of “W”-QWH heterostructures and lasers provides various arguments for further investigations of the (GaIn)As/Ga(AsSb)/(GaIn)As material system grown on GaAs substrates. On the one hand, its large spectral coverage allows the fabrication of heterostructures, which are tailored for emission in the whole O-band. On the other hand, the demonstration of VECSELs emitting at 1.2 μm as well as electrical injection lasers emitting at 1.2 μm and 1.3 μm provide evidence for their applicability. Especially the opportunity to tailor the temperature-induced shift rate of the emission wavelength allows for the design of novel device concepts that utilize “W”-QWHs as active regions. Examples for such device concepts could be distributed feedback (DFB) and DBR lasers, where the shift rate of the grating and the gain spectrum are matched in order to obtain more stable devices. Another particularly interesting investigation is the operation of “W”-QWH lasers under CW operating conditions, because the interplay between the resistive heating of the device and the charge carrier density should result in decreased shift rates of the emission wavelength, too. Further work is also required to demonstrate that lasers emitting in the whole O-band can be designed and whether it is possible to tailor the shift rate in these devices.

While the work presented here utilizes one particular material system, other alloys may also be considered as candidates for further investigations. The compressive strain of (GaIn)As and Ga(AsSb) grown on GaAs substrates ultimately limits the emission wavelength. Consequently, novel material combinations will be required to achieve emission at even longer wavelengths such as 1.55 μm and in the mid-infrared regime. Possible material choices include dilute nitrogen-containing Ga(NAs), (GaIn)As, Ga(AsSb), dilute bismuth-containing Ga(AsBi) as well as various alloys containing four or more constituent atoms. Especially dilute nitride-based^{85,94,95,109–114} and dilute bismide-based^{115,116} type-II heterostructures are promising since their lattice parameters can be used to avoid strain limitations. Additionally, the band structure characteristics of dilute bismides may support the suppression or reduction of IVBA and CHSH Auger recombination^{47,83}. A careful

design of such active regions could even enable the fabrication of fully strain-compensated heterostructures^{117,118}.

CHAPTER 6

Scientific contributions

The following sections outline the scientific contributions made by Christian Fuchs. The content of this thesis, which is summarized in Cha. 4, is presented in published and submitted manuscripts in Secs. 6.1 to 6.4. Additionally, further publications are summarized in Sec. 6.5 and talks and posters are summarized in 6.6.

The present work was carried out in the framework of Sonderforschungsbereich 1083 - “Structure and Dynamics of Internal Interfaces” funded by Deutsche Forschungsgemeinschaft and includes the cooperation of various groups. The design of “W”-quantum well heterostructures using a fully microscopic theory was carried out in the group of Prof. Dr. Stephan W. Koch by Dr. Ada Bäumner, Dr. Christian Berger and Maria J. Weseloh. The microscopic investigation of the “W”-quantum well heterostructures using scanning transmission electron microscopy was carried out by Dr. Andreas Beyer and Pirmin Kükelhan in the group of Prof. Dr. Kerstin Volz. The work in the group of Prof. Dr. Wolfgang Stolz is split into the epitaxial growth of (GaIn)As/Ga(AsSb)/(GaIn)As “W”-quantum well heterostructures and lasers carried out by Christian Fuchs, the spectroscopic investigation of vertical-external-cavity surface-emitting lasers carried out by Dr. Christoph Möller, and the spectroscopic investigation of electrical injection lasers carried out by Christian Fuchs and Anja Brüggemann.

6.1 Publication 1

Citation

C Fuchs, A Beyer, K Volz, and W Stolz. MOVPE growth of (GaIn)As/Ga(AsSb)/(GaIn)As type-II heterostructures on GaAs substrate for near infrared laser applications. *J. Cryst. Growth*, 464:201 – 205, 2017. doi: 10.1016/j.jcrysgro.2016.10.052⁹⁷

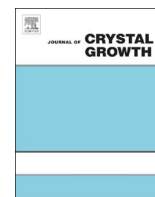
Reproduced with the permission of Elsevier.

Abstract

The growth of high quality (GaIn)As/Ga(AsSb)/(GaIn)As “W”-quantum well heterostructures is discussed with respect to their application in 1300 nm laser devices. The structures are grown using metal organic vapor phase epitaxy and characterized using high-resolution X-ray diffraction, scanning transmission electron microscopy and photoluminescence measurements. The agreement between experimental high-resolution X-ray diffraction patterns and full dynamical simulations is verified for these structurally challenging heterostructures. Scanning transmission electron microscopy is used to demonstrate that the structure consists of well-defined quantum wells and forms the basis for future improvements of the optoelectronic quality of this materials system. By altering the group-V gas phase ratio, it is possible to cover a large spectral range between 1200 nm and 1470 nm using a growth temperature of 550 °C and a V/III ratio of 7.5. A comparison of a sample with a photoluminescence emission wavelength at 1360 nm with single quantum well material reference samples proves the type-II character of the emission. A further optimization of these structures for application in 1300 nm lasers by applying different V/III ratios yields a stable behavior of the photoluminescence intensity using a growth temperature of 550 °C.

Contributions

Christian Fuchs carried out the epitaxial growth, the structural characterization using HR-XRD, and the optical characterization using PL spectroscopy of the “W”-QWHs. Andreas Beyer investigated the sample using scanning transmission electron microscopy (STEM). Christian Fuchs wrote the manuscript except for the STEM section, which was contributed by Andreas Beyer. Kerstin Volz and Wolfgang Stolz supervised the work and secured the funding to support this study. All authors reviewed the manuscript.



Si: 18th int. conf. on movpe

MOVPE growth of (GaIn)As/Ga(AsSb)/(GaIn)As type-II heterostructures on GaAs substrate for near infrared laser applications



C. Fuchs*, A. Beyer, K. Volz, W. Stolz

Materials Sciences Center and Department of Physics, Philipps-Universität Marburg, Hans-Meerwein-Str., 35032 Marburg, Germany

ARTICLE INFO

Communicated by Dr. T.F. Kuech

Keywords:

A1 Characterization
 A3 Low press.
 A3 Metalorganic vapor phase epitaxy
 B1 Antimonides
 B2 Semiconducting III-V materials
 B2 Semiconducting gallium arsenide
 B3 Laser diodes

ABSTRACT

The growth of high quality (GaIn)As/Ga(AsSb)/(GaIn)As “W”-quantum well heterostructures is discussed with respect to their application in 1300 nm laser devices. The structures are grown using metal organic vapor phase epitaxy and characterized using high-resolution X-ray diffraction, scanning transmission electron microscopy and photoluminescence measurements. The agreement between experimental high-resolution X-ray diffraction patterns and full dynamical simulations is verified for these structurally challenging heterostructures. Scanning transmission electron microscopy is used to demonstrate that the structure consists of well-defined quantum wells and forms the basis for future improvements of the optoelectronic quality of this materials system. By altering the group-V gas phase ratio, it is possible to cover a large spectral range between 1200 nm and 1470 nm using a growth temperature of 550 °C and a V/III ratio of 7.5. A comparison of a sample with a photoluminescence emission wavelength at 1360 nm with single quantum well material reference samples proves the type-II character of the emission. A further optimization of these structures for application in 1300 nm lasers by applying different V/III ratios yields a stable behavior of the photoluminescence intensity using a growth temperature of 550 °C.

1. Introduction

While GaAs-based semiconductor laser technology has enabled the realization of highly efficient semiconductor lasers at technologically important wavelengths such as 808 nm and 980 nm, present-day telecommunications systems typically apply InP-based technology. Novel GaAs-based type-I material systems such as (GaIn)(NAs)/GaAs [1] and Ga(AsSb)/GaAs [2] were suggested as possible candidates for more efficient telecommunications systems at 1300 nm, but their respective material properties have proven to be challenging obstacles.

Additionally, Auger losses are a limiting factor in terms of the performance of type-I laser systems [3]. As a consequence, type-II laser systems were suggested in order to improve device performances at even longer emission wavelengths [3,4]. In these systems, electrons and holes are spatially separated in different quantum wells (QWs). Thus, it is possible to separately tune the conduction and valence band states that contribute to the emission of light from these structures. This additional degree of freedom can be used to optimize possible devices and for a more flexible band gap engineering.

A possible materials combination that exhibits a type-II band alignment consists of (GaIn)As as electron QW material and Ga(AsSb) as hole QW material. Both of these materials can be

pseudomorphically grown on GaAs substrate. Early investigations of this materials system typically employed bilayer structures [5] and electrical injection lasing was demonstrated in the near-infrared regime by Klem et al. [6] and Ryu and Dapkus [7]. However, the performance of these devices was limited to 140 mW output power per facet at a wavelength of 1170 nm under pulsed excitation conditions.

One approach to optimize these structures is the application of “W”-type band alignments. In these structures, the hole QW is embedded between two electron QWs in order to optimize the wave function overlap [8,9]. Different groups have recently applied this materials system on InP and demonstrated electrical injection lasing in the mid-infrared wavelength regime [10]. Recently, we have applied metal organic vapor phase epitaxy (MOVPE) in order to grow on GaAs substrate a vertical-external-cavity laser surface-emitting in the 1.2 μm region. The device exhibited a maximum continuous wave output power of 4 W and laser emission based on the type-II transition in these structures was proven [11]. Additionally, an electrical-injection edge-emitting laser with a maximum output power of 1.4 W was demonstrated in this wavelength region [12].

In the present publication, the epitaxial growth of (GaIn)As/Ga(AsSb)/(GaIn)As “W”-QW heterostructures (“W”-QWHs) is discussed with respect to laser applications at 1300 nm. Since the highly

* Corresponding author.

E-mail address: christian.fuchs@physik.uni-marburg.de (C. Fuchs).

strained “W”-QWHs represent a structurally challenging system, the high-resolution X-ray diffraction (HR-XRD) pattern of a sample is compared to the simulation based on a full dynamical X-ray theory. In order to support the HR-XRD pattern modeling and because interface characteristics are particularly important in these type-II structures, structural analysis by scanning transmission electron microscopy (STEM) is performed. Since (GaIn)As is a more established alloy than Ga(AsSb), the following investigation of the growth conditions of the “W”-QWH aims at optimizing the growth conditions of Ga(AsSb) as hole QW in “W”-QWHs. An investigation of the potential of the (GaIn)As/Ga(AsSb)/(GaIn)As materials system is carried out by varying the TESb/V ratio and the V/III ratio ($V = \text{TbAs} + \text{TESb}$).

2. Growth and characterization of (GaIn)As/Ga(AsSb)/(GaIn)As “W”-type structures

The sample growth is carried out in a commercial AIXTRON AIX 200 GFR (Gas Foil Rotation) reactor system using triethylgallium (TEGa) and trimethylindium (TMIn) as group-III and tertiarybutylarsine (TBAs) and triethylantimony (TESb) as group-V sources, respectively. The reactor pressure is set to 50 mbar and high-purity H_2 is used as carrier gas. The native oxide layer is removed from the semi-insulating GaAs (001) ($\pm 0.1^\circ$) substrate by applying a TBAs-stabilized bake-out procedure. The growth process of the “W”-QWH active region as well as the 50 nm GaAs barrier is carried out at a temperature of 550 °C. This growth temperature was chosen after performing detailed growth investigations in the temperature range of 500–600 °C for (GaIn)As/GaAs- and Ga(AsSb)/GaAs-test structures. At this growth temperature record laser performances for both type-II surface- as well as edge-emitting laser structures [11,12] were demonstrated. The active region includes one 4 nm $\text{Ga}(\text{As}_{1-x}\text{Sb}_x)$ hole QW and two 6 nm $(\text{Ga}_{0.8}\text{In}_{0.2})\text{As}$ electron QWs. The “W”-QWH and the barrier are repeated three times and a 5 nm GaAs cap is grown on top of the uppermost “W”-QWH. The layer structures are deposited by continuous growth, applying no specific interface switching schemes. All layer thicknesses are kept constant in order to ensure that changes in the photoluminescence signal can be attributed to changes in TESb/V and V/III ratios. A schematic illustration of the resulting sample structure can be found in the inset of Fig. 1.

HR-XRD measurements are carried out using a Panalytical X’Pert

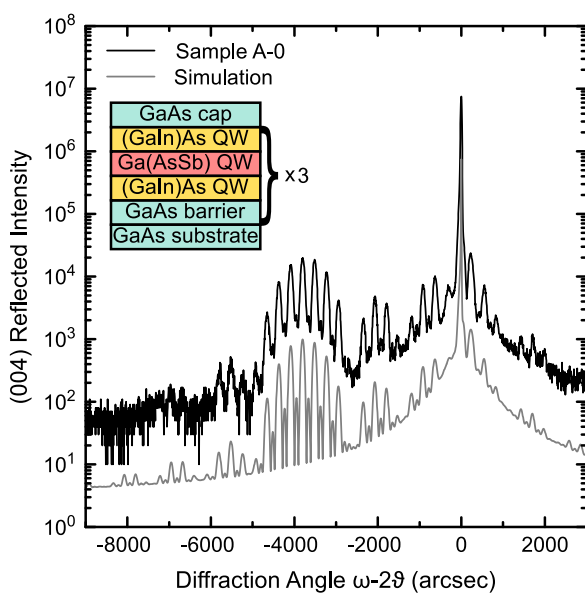


Fig. 1. Exemplary comparison of the HR-XRD measurement of sample A-0 and the respective full dynamical simulation result. The inset illustrates the sample structure of all samples (except for the reference samples R-Sb and R-In) discussed in the present work.

Pro system. Compositions and layer thicknesses are determined from measurements of the ω -2 θ diffraction patterns around the (004)-reflection of GaAs. The modeling of the HR-XRD patterns is carried out based on a full dynamical X-ray theory as outlined in [13,14]. For simplicity, constant chemical compositions in the respective (GaIn)As- and Ga(AsSb)-constituent layers are assumed. As the structure only consists of ternary materials, these simulations allow a complete determination of all relevant average material compositions and strain values as well as average layer thicknesses.

The detailed analysis of the active (GaIn)As/Ga(AsSb)/(GaIn)As “W”-QWH is performed by atomic resolution STEM applying the high-angle annular dark field (HAADF) technique using a double-aberration-corrected JEOL 2200FS microscope operating at 200 kV. A convergence semi-angle of 24 mrad is chosen and the angular detector collects electrons scattered in the range between 72 and 174 mrad. To improve the signal-to-noise ratio, series of 14 individual images are acquired and aligned non-rigidly using the Smart-Align software [15].

Photoluminescence (PL) measurements are carried out in a custom-built setup by non-resonantly exciting the samples using a frequency-doubled Nd:YAG laser ($\lambda_{\text{exc}} = 532$ nm). The excitation power was set to 100 mW using a spot size of approximately 20 μm . The resulting PL signal is dispersed by a grating monochromator (Jobin-Yvon THR 1000) and detected using a liquid nitrogen cooled germanium detector in combination with a lock-in amplifier. In addition to this setup, a commercial ACCENT rpm2000 PL mapper system is used to measure low excitation density PL from these samples. The samples are excited using a frequency-doubled Nd:YAG laser ($\lambda_{\text{exc}} = 532$ nm), too. However, the excitation power is set to 6.5 mW and the resulting PL signal is detected with an (InGa)As or a CCD detector for peak wavelengths above and below 1000 nm, respectively.

3. Results and discussion

In order to prove that it is possible to determine compositions as well as thicknesses from HR-XRD measurements, the experimental data of sample A-0 is compared to the simulation in Fig. 1. The comparison yields an excellent agreement between the experimental data and the simulation and thus, ensures a reliable determination of the structural properties, i.e. average layer thicknesses and average compositions. Furthermore, the sharp fringes in the diffraction pattern, which are observed up to diffraction angles of $\sim 7000''$, indicate a high structural sample quality.

An overview of all properties obtained from HR-XRD evaluations as well as the growth conditions can be found in Table 1. The thickness of a single repetition of the “W”-QWH together with the GaAs barrier (D_{SLs}) is also given in Table 1 in order to verify the constant layer thickness in the active region for the samples under investigation.

The successful realization of the “W”-QWH is proven by atomic resolution HAADF STEM measurements as shown in Fig. 2a). The

Table 1

Overview of all samples discussed in the present work. The Sb concentrations, Ga(AsSb) strain values (ε_{Sb}) as well as the thickness of a single repetition of the “W”-QWH together with the GaAs-barrier (D_{SLs}) are determined using HR-XRD measurements. The PL peak wavelength values are obtained using the PL mapper system.

Sample	V/III	T_g [°C]	TESb/V	c_{Sb} [%]	ε_{Sb} [%]	D_{SLs} [nm]	λ [nm]
A-0	7.5	550	0.830	19.3	1.5	65.3	1215
A-1	7.5	550	0.850	24.0	1.8	64.9	1295
A-2	7.5	550	0.853	27.4	2.1	64.8	1360
A-3	7.5	550	0.860	28.2	2.2	63.7	1400
A-4	7.5	550	0.870	30.2	2.3	65.1	1470
B-0	4.0	550	0.730	25.5	2.0	64.5	1340
C-0	2.0	550	0.500	26.2	2.0	65.0	1370
R-Sb	1.9	500	0.320	26.0	–	–	1170
R-In	3.9	550	–	–	–	–	990
R-STEM	7.6	550	0.787	19.0	–	–	1205

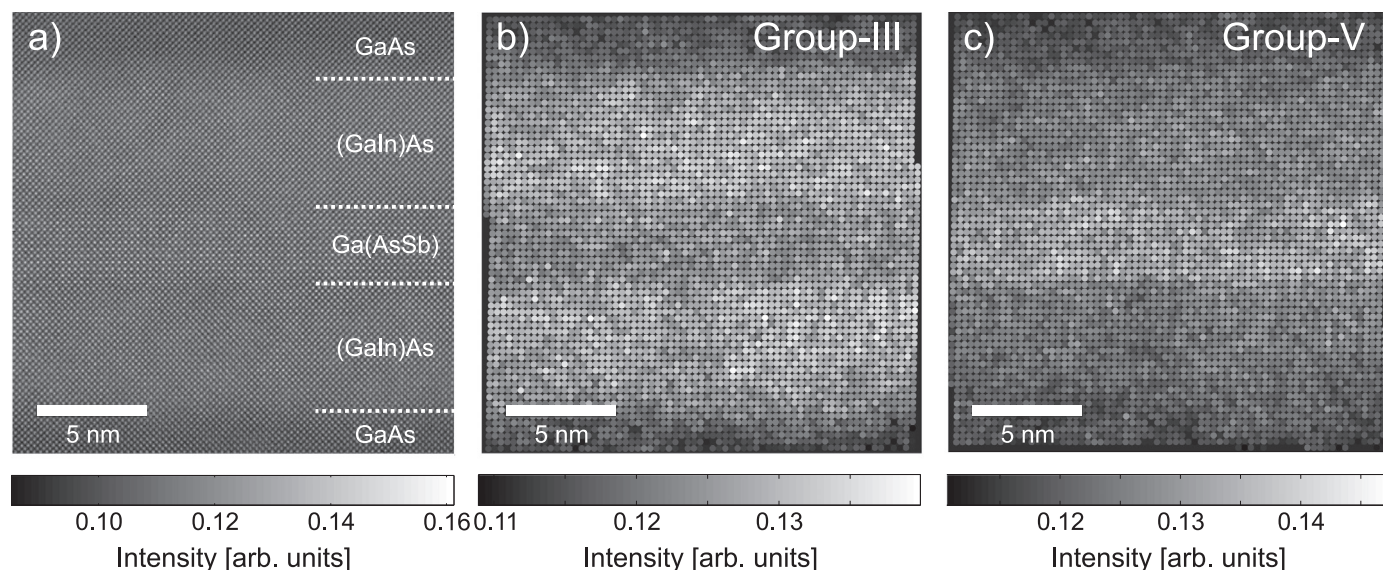


Fig. 2. a) Atomic resolution HAADF STEM image of the the “W”-QWH active region of reference sample R-STEM. In order to increase the visibility of the individual layers, the intensity of the group-III and group-V sublattices are shown separately in b) and c), respectively.

MOVPE-growth direction is from bottom to top in this image. As the electron scattering is proportional to the atomic number of the scattering material, the HAADF intensity is sensitive to the chemical composition of the material. The visibility of the individual layers is increased by separating the intensities of the group-III and group-V sublattices as shown in Fig. 2b) and c), respectively. In these maps, the intensity of each atomic column is derived by averaging the HAADF intensity in a circular region with a radius of 2 pixels (≈ 0.04 nm) around its center. The slightly increased intensity in the antimony (Sb)-containing region with respect to the GaAs barrier in Fig. 2b) is most likely caused by “cross scattering” between the two sublattices [16] rather than indium (In)-diffusion into the Ga(AsSb) QW. The same behavior can be observed in the In-containing region in Fig. 2c). Overall, these investigations clearly show that the “W”-QWH active region consists of three separated and well-defined QWs. It is important to note that clearly In- as well as Sb-segregation effects are detected in the evaluated STEM micrographs.

In the future, a further quantitative chemical analysis of the individual compositions in the “W”-QWH utilizing complementary contrast simulations [17] can allow for a precise determination of the actual chemical composition in each and every atomic column of all of the constituent layers for all of the studied samples. This real quantification on the atomic scale will on one side serve as the input for more sophisticated HR-XRD modeling in the future. On the other side this quantification will lead to the clarification of the actual band profile of the deposited “W”-QWH, which is of key importance for a realistic modeling of the optoelectronic properties of these type-II “W”-QWHs.

The samples analyzed in Fig. 1 and Fig. 2 exhibit PL peaks at approximately 1200 nm. A first attempt to extend the emission wavelength obtained from the “W”-QWH samples is carried out changing the Sb concentration in the Ga(AsSb) hole QW. A variation of the TESb/V ratio from 0.83 to 0.87 at a constant V/III ratio of 7.5 results in PL peaks between 1215 nm and 1470 nm measured in the PL mapper system. An evaluation of the HR-XRD patterns shown in Fig. 3 indicates that this large spectral coverage corresponds to Sb concentrations between 19.3% and 30.2%. Furthermore, the HR-XRD patterns yield well defined fringes in the diffraction pattern up to diffraction angles above $-8000''$ indicating good structural sample qualities. This is particularly promising due to the laser results based on these growth conditions as reported in Ref [12]. A line broadening of the HR-XRD pattern for the highest diffraction orders is only

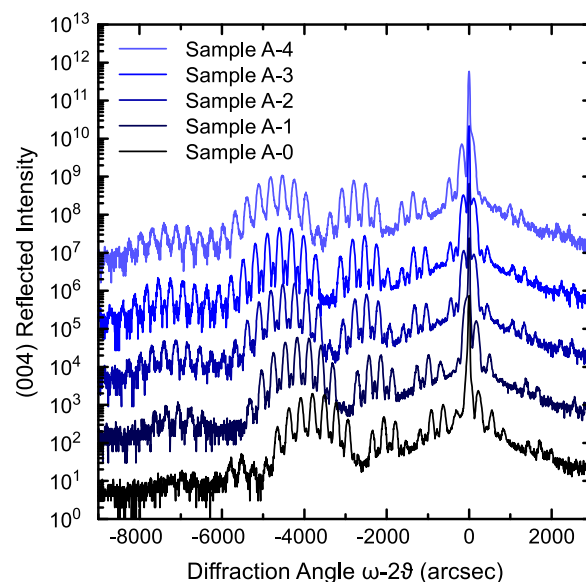


Fig. 3. HR-XRD patterns of a series of “W”-QWH samples grown at a temperature of 550 °C using a constant V/III ratio of 7.5 and different TESb/V ratios. The HR-XRD pattern of the samples A-0 to A-4, arranged from bottom to top, are shifted on the intensity scale for clarity. The growth conditions of (GaIn)As remain unchanged. TESb/V ratios between 0.830 and 0.870 result in Sb concentrations ranging from 19.3–30.2%. Consequently, the PL peak wavelength varies from 1215 nm to 1470 nm ($P_{\text{exc}}=6.5$ mW).

observed in case of sample A-4 with the highest Sb-concentration of 30.2%. This is a clear indication of an inhomogeneous broadening of the interface configuration presumably caused by a strain-induced roughening of the growth surface of the Ga(AsSb) at this high strain value of 2.3%.

While these structural results are promising, it is necessary to demonstrate that the PL emission from the structures discussed here is actually based on type-II transitions. Therefore, the normalized PL spectra of a reference structure R-In that only contains $(\text{Ga}_{0.792}\text{In}_{0.208})$ As QWHs, of a reference structure R-Sb that only contains $\text{Ga}(\text{As}_{0.740}\text{Sb}_{0.260})$ QWHs and of “W”-QWH sample A-2 are plotted together in Fig. 4. The PL signal of sample A-2 is clearly red-shifted compared to both of the reference samples. This indicates that energy states from both materials contribute to this emission and thus, implies a type-II character of the emission.

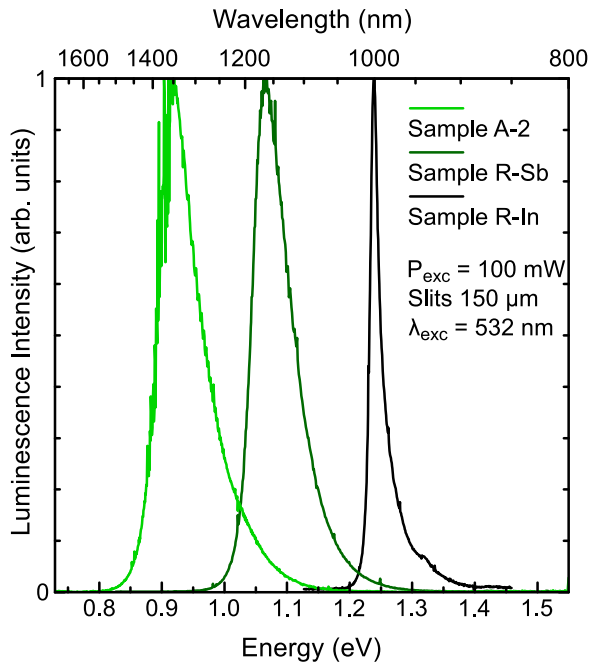


Fig. 4. Room temperature PL spectra of samples A-2 (left), R-Sb (center) and R-In (right). The spectral position of the “W”-QWH PL is red shifted compared to the spectral position of the single QWH PL of the (GaIn)As as well as the Ga(AsSb) reference sample indicating a type-II band alignment.

While the analysis of samples grown with different TESb/V ratios described above is promising due to the high structural quality of the samples and the large spectral variation in the emission wavelengths, it also shows that minor changes of the growth conditions can result in large changes in the incorporation behavior of Sb. This finding is in good agreement with the literature [18]. As a result, a further optimization is carried out in order to find stable growth conditions that result in high PL intensities at a wavelength of approximately 1300 nm. Due to the well described blue shift in these structures between PL and lasing wavelengths [12,19–21], the PL peak wavelength is set to about 1350 nm in order to enable laser operation at 1300 nm in future devices.

In order to find such growth conditions, different V/III ratios of 7.5, 4.0 and 2.0 are chosen. As summarized in Table 1, the required TESb/V ratios are greatly reduced if lower V/III ratios are applied. This finding also agrees with previous studies [18]. The HR-XRD patterns of the correspondent samples A-2, B-0 and C-0 are illustrated in Fig. 5 together with A-0 as reference. While the quality of these HR-XRD patterns is generally similar, the Pendellösung fringes of sample B-0 are more pronounced. The evaluation yields a Sb concentration of approximately 26.5% that is required for future application in 1300 nm lasers.

Since the properties of laser devices are dominated by structural as well as optoelectronic properties of the constituent materials, PL measurements of the structures designed for 1300 nm laser emission are carried out. The measurements are illustrated in Fig. 6.

All samples exhibit a peak intensity that is about a factor of 3 lower than the peak intensity of the structure designed for emission around 1200 nm. In contrast to type-I structures, where this could most certainly be connected to the material quality, this result can be explained by the reduced wave function overlap in the case of the type-II structures. It results from a deeper hole QW which corresponds to a stronger localization of the hole wave function and thus, a reduced wave function overlap of electrons and holes. All samples show an almost constant behavior and only small changes can be observed in terms of the peak intensities and peak widths. Wave function overlap is a key parameter for the performance of type-II “W”-QW lasers. It is important to note, however, that this overlap is not constant as a

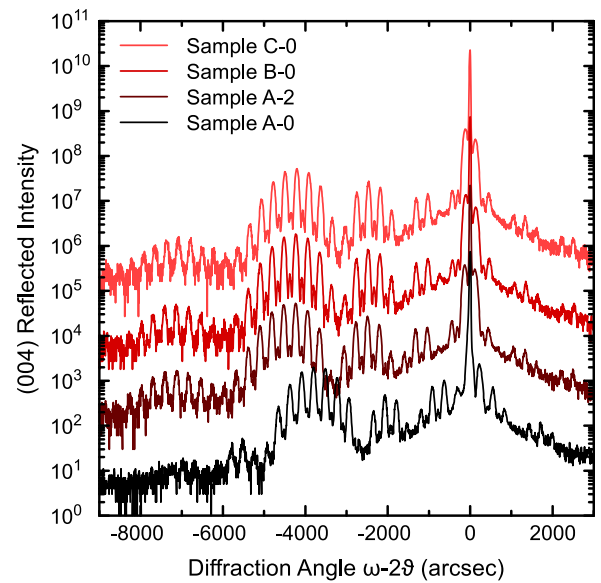


Fig. 5. HR-XRD patterns of a series of “W”-QWH samples designed for laser emission at 1300 nm and reference sample A-0. The HR-XRD pattern of the samples A-0, A-2, B-0 and C-0, arranged from bottom to top, are shifted on the intensity scale for clarity. Samples A-2, B-0 and C-0 are grown at a temperature of 550 °C using V/III ratios of 7.5, 4.0 and 2.0, respectively. The growth conditions of (GaIn)As remain unchanged. Due to the well described blue shift in type-II heterostructures, the structures are tailored to exhibit a PL peak wavelength of approximately 1350 nm.

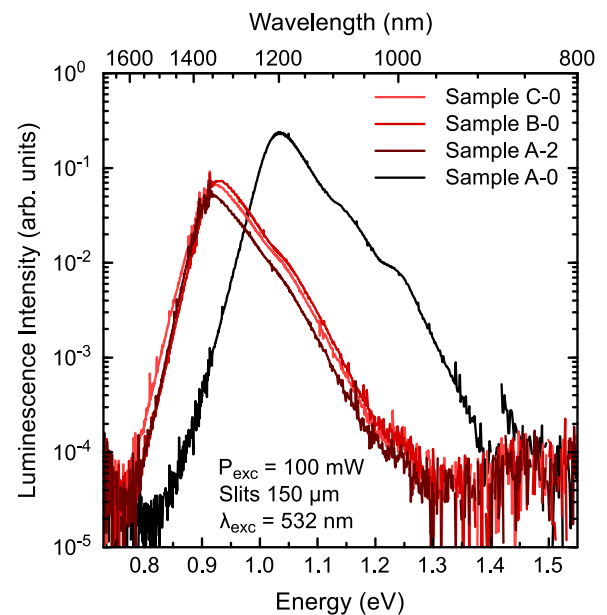


Fig. 6. Room temperature PL spectra of a series of “W”-QWH samples designed for laser emission at 1300 nm and reference sample A-0. Samples A-2 (lowest peak intensity at 1350 nm), B-0 (highest peak intensity at 1350 nm) and C-0 (medium peak intensity at 1350 nm) are grown at a temperature of 550 °C using V/III ratios of 7.5, 4.0 and 2.0, respectively.

function of injected carrier density as in a type-I system, but increases with higher carrier densities due to the band bending resulting from the charge separation of electrons and holes in the “W”-structures. Thus, low-excitation density PL studies in type-II systems have to be treated with even greater care as compared to type-I structures, if one would like to draw any predictive conclusion for laser performance. Future work will concentrate on the realization and characterization of actual edge-emitting laser structures applying the active (GaIn)As/Ga(AsSb)/(GaIn)As “W”-QWHs as optimized in this study for the emission wavelength range around 1300 nm.

4. Conclusion and outlook

The MOVPE growth of $(\text{Ga}_{0.8}\text{In}_{0.2})\text{As}/\text{Ga}(\text{As}_{1-x}\text{Sb}_x)/(\text{Ga}_{0.8}\text{In}_{0.2})\text{As}$ “W”-QWHs has resulted in well-defined QWH systems as shown by HR-XRD and STEM. The QW thicknesses chosen in this study were 6 nm for $(\text{GaIn})\text{As}$ and 4 nm for $\text{Ga}(\text{AsSb})$. Furthermore, by changing the group-V gas phase ratio at a fixed V/III ratio of 7.5 and growth temperature of 550 °C, it was possible to grow high quality “W”-QWHs that exhibit PL peak intensities between 1200 nm and 1470 nm corresponding to a Sb content between 19.3% and 30.2%, respectively. An optimization of the structures for laser applications at 1300 nm was carried out with samples that exhibit PL peak intensities at approximately 1350 nm. The V/III ratio does not show a significant influence on the optoelectronic quality in case of samples grown at 550 °C. Further work will concentrate on realizing actual laser devices based on these “W”-QWHs at 1300 nm.

Acknowledgements

The authors gratefully acknowledge the funding provided by Deutsche Forschungsgemeinschaft (DFG) in the framework of Sonderforschungsbereich 1083 – Structure and Dynamics of Internal Interfaces.

References

- [1] F. Höhnsdorf, J. Koch, S. Leu, W. Stolz, B. Borchert, M. Druminski, Reduced threshold current densities of $(\text{GaIn})(\text{NAs})/\text{GaAs}$ single quantum well lasers for emission wavelengths in the range 1.28–1.38 μm , *Electron. Lett.* 35 (7) (1999) 571–572. <http://dx.doi.org/10.1049/el:19990421>.
- [2] M. Yamada, T. Anan, K. Tokutome, A. Kamei, K. Nishi, S. Sugou, Low-threshold operation of 1.3- μm GaAsSb quantum-well lasers directly grown on GaAs substrates, *IEEE Photon.- Technol. Lett.* 12 (7) (2000) 774–776. <http://dx.doi.org/10.1109/68.853496>.
- [3] J.R. Meyer, C.L. Felix, W.W. Bewley, I. Vurgaftman, E.H. Aifer, L.J. Olafsen, J.R. Lindle, C.A. Hoffmann, M.J. Yang, B.R. Bennett, B.V. Shanabrook, H. Lee, C.H. Lin, S.S. Pei, R.H. Miles, Auger coefficients in type-II $\text{InAs}/\text{Ga}_{1-x}\text{In}_x\text{Sb}$ quantum wells, *Appl. Phys. Lett.* 73 (20) (1998) 2857–2859. <http://dx.doi.org/10.1063/1.122609>.
- [4] G.G. Zegrya, A.D. Andreev, Mechanism of suppression of Auger recombination processes in type-II heterostructures, *Appl. Phys. Lett.* 67 (18) (1995) 2681–2683. <http://dx.doi.org/10.1063/1.114291>.
- [5] M. Peter, K. Winkler, M. Maier, N. Herres, J. Wagner, D. Fekete, K.H. Bachem, D. Richards, Realization and modeling of a pseudomorphic $(\text{GaAs}_{1-x}\text{Sb}_x-\text{In}_x\text{Ga}_{1-x}\text{As})/\text{GaAs}$ bilayer-quantum well, *Appl. Phys. Lett.* 67 (18) (1995) 2639–2641. <http://dx.doi.org/10.1063/1.114321>.
- [6] J.F. Klem, O. Blum, S.R. Kurtz, I.J. Fritz, K.D. Choquette, $\text{GaAsSb}/\text{InGaAs}$ type-II quantum wells for long-wavelength lasers on GaAs substrates, *J. Vac. Sci. Technol. B* 18 (3) (2000) 1605–1608. <http://dx.doi.org/10.1116/1.591437>.
- [7] S.W. Ryu, P.D. Dapkus, Room temperature operation of type-II $\text{GaAsSb}/\text{InGaAs}$ quantum well laser on GaAs substrates, *Electron. Lett.* 38 (12) (2002) 564–565. <http://dx.doi.org/10.1049/el:20020410>.
- [8] M. Kudo, K. Ouchi, J. Kasai, T. Mishima, Low-lattice-strain long-wavelength $\text{GaAsSb}/\text{GaInAs}$ type-II quantum wells grown on GaAs substrates, *Jpn. J. Appl. Phys.* 41 (2) (2002) 1040–1042. <http://dx.doi.org/10.1143/JJAP.41.L1040>.
- [9] N. Tansu, L.J. Mawst, Design analysis of 1550-nm $\text{GaAsSb}-(\text{In})\text{GaAsn}$ type-II quantum-well laser active regions, *IEEE J. Quantum Electron.* 39 (10) (2003) 1205–1210. <http://dx.doi.org/10.1109/JQE.2003.817235>.
- [10] S. Sprengel, C. Grasse, P. Wiecha, A. Andrejew, T. Gruendl, G. Boehm, R. Meyer, M.C. Amann, InP-based Type-II quantum-well lasers and LEDs, *IEEE J. Sel. Top. Quantum Electron.* 19 (4) (2013) 1900909. <http://dx.doi.org/10.1109/JSTQE.2013.2247572>.
- [11] C. Möller, C. Fuchs, C. Berger, A. Ruiz Perez, M. Koch, J. Hader, J.V. Moloney, S.W. Koch, W. Stolz, Type-II vertical-external-cavity surface-emitting laser with Watt level output powers at 1.2 μm , *Appl. Phys. Lett.* 108 (7) (2016) 071102. <http://dx.doi.org/10.1063/1.4942103>.
- [12] Fuchs, C., Berger, C., Möller, C., Weseloh, M., Reinhard, S., Hader, J., Moloney, J. V., Koch, S.W. and Stolz, W., Electrical injection type-II $(\text{GaIn})\text{As}/\text{Ga}(\text{AsSb})/(\text{GaIn})\text{As}$ single W-quantum well laser at 1.2 μm , *Electron. Lett.*, accepted for publication, doi: 10.1049/el.2016.2851.
- [13] L. Tapfer, K. Ploog, X-ray interference in ultrathin epitaxial layers: a versatile method for the structural analysis of single quantum wells and heterointerfaces, *Phys. Rev. B* 40 (14) (1989) 9802–9810. <http://dx.doi.org/10.1103/PhysRevB.40.9802>.
- [14] L. De Caro, C. Giannini, L. Tapfer, Determination of the lattice strain and chemical composition of semiconductor heterostructures by high-resolution x-ray diffraction, *J. Appl. Phys.* 79 (8) (1996) 4101–4110. <http://dx.doi.org/10.1063/1.361773>.
- [15] L. Jones, H. Yang, T.J. Pennycook, M.S.J. Marshall, S. Van Aert, N.D. Browning, M.R. Castel, P.D. Nellist, Smart Align – a new tool for robust non-rigid registration of scanning microscope data, *Adv. Struct. Chem. Imag.* 1 (1) (2015) 1–16. <http://dx.doi.org/10.1186/s40679-015-0008-4>.
- [16] P.D. Nellist, S.J. Pennycook, Incoherent imaging using dynamically scattered coherent electrons, *Ultramicroscopy* 78 (1–4) (1998) 111–124. [http://dx.doi.org/10.1016/S0304-3991\(99\)00017-0](http://dx.doi.org/10.1016/S0304-3991(99)00017-0).
- [17] A. Beyer, A. Stegmüller, J.O. Oelerich, K. Jandieri, K. Werner, G. Mette, W. Stolz, S.D. Baranovskii, R. Tonner, K. Volz, Pyramidal structure formation at the interface between III/V semiconductors and silicon, *Chem. Mater.* 28 (10) (2016) 3265–3275. <http://dx.doi.org/10.1021/acs.chemmater.5b04896>.
- [18] G.B. Stringfellow, M.J. Cherng, OMVPE growth of $\text{GaAs}_{1-x}\text{Sb}_x$: solid composition, *J. Cryst. Growth* 64 (2) (1983) 413–415. [http://dx.doi.org/10.1016/0022-0248\(83\)90156-2](http://dx.doi.org/10.1016/0022-0248(83)90156-2).
- [19] W.W. Chow, H.C. Schneider, Charge-separation effects in 1.3 μm GaAsSb type-II quantum-well laser gain, *Appl. Phys. Lett.* 78 (26) (2001) 4100–4102. <http://dx.doi.org/10.1063/1.1379784>.
- [20] W.W. Chow, O. Blum Spahn, H.C. Schneider, J.F. Klem, Contributions to the large blue emission shift in a GaAsSb type-II laser, *IEEE J. Quantum Electron.* 37 (9) (2001) 1178–1182. <http://dx.doi.org/10.1109/3.945323>.
- [21] C. Berger, C. Möller, P. Hens, C. Fuchs, W. Stolz, S.W. Koch, A. Ruiz Perez, J. Hader, J.V. Moloney, Novel type-II material system for laser applications in the near-infrared regime, *AIP Adv.* 5 (4) (2015) 047105. <http://dx.doi.org/10.1063/1.4917180>.

6.2 Publication 2

Citation

C Fuchs, C Berger, C Möller, M Weseloh, S Reinhard, J Hader, J V Moloney, S W Koch, and W Stolz. Electrical injection type-II (GaIn)As/Ga(AsSb)/(GaIn)As single ‘W’-quantum well laser at 1.2 μm . *Electron. Lett.*, 52(22):1875 – 1877, 2016. doi: 10.1049/el.2016.2851¹¹⁹
 Reproduced with the permission of the Institution of Engineering & Technology.

Abstract

Highly efficient interface-dominated electrical injection lasers in the near-infrared regime based on the type-II band alignment in (GaIn)As/Ga(AsSb)/(GaIn)As single “W”-quantum wells are realised. The structure is designed by applying a fully microscopic theory, grown by metal organic vapour phase epitaxy, and characterised using electroluminescence measurements and broad-area laser studies. A characteristic blue shift of 93 meV/(kA/cm²) with increasing charge carrier density is observed and compared with theoretical investigations. Low threshold current densities of 0.4 kA cm⁻², high differential efficiencies of 66 %, optical output powers of 1.4 W per facet, and internal losses of only 1.9 cm⁻¹ are observed at a wavelength of 1164 nm for a cavity length of 930 μm . For a cavity length of 2070 μm , the threshold current density is reduced to 0.1 kA cm⁻². No indication for type-I related transitions for current densities up to 4.6 kA cm⁻² is observed.

Contributions

Christian Fuchs designed and carried out the epitaxial growth of the laser structures, the experimental device analysis, and the data evaluation. Christoph Möller supported the spectroscopic experiments. Stefan Reinhard fabricated broad-area edge-emitting lasers. Christian Berger and Maria J. Weseloh carried out the theoretical studies. Jörg Hader, Jerome V. Moloney, Stephan W. Koch, and Wolfgang Stolz supervised the work and secured the funding to support this study. All authors reviewed the manuscript.

Electrical injection type-II (GaIn)As/Ga(AsSb)/(GaIn)As single 'W'-quantum well laser at 1.2 μm

C. Fuchs[✉], C. Berger, C. Möller, M. Weseloh, S. Reinhard, J. Hader, J.V. Moloney, S.W. Koch and W. Stolz

Highly efficient interface-dominated electrical injection lasers in the near-infrared regime based on the type-II band alignment in (GaIn)As/Ga(AsSb)/(GaIn)As single 'W'-quantum wells are realised. The structure is designed by applying a fully microscopic theory, grown by metal organic vapour phase epitaxy, and characterised using electroluminescence measurements and broad-area laser studies. A characteristic blue shift of 93 meV/(kA/cm²) with increasing charge carrier density is observed and compared with theoretical investigations. Low threshold current densities of 0.4 kA/cm², high differential efficiencies of 66%, optical output powers of 1.4 W per facet, and internal losses of only 1.9 cm⁻¹ are observed at a wavelength of 1164 nm for a cavity length of 930 μm . For a cavity length of 2070 μm , the threshold current density is reduced to 0.1 kA/cm². No indication for type-I related transitions for current densities up to 4.6 kA/cm² is observed.

Introduction: The development of highly efficient semiconductor lasers in the near-infrared (NIR) wavelength regime is of great interest due to their application, e.g. in fibre-optic telecommunication systems [1]. While present-day systems typically apply InP-based technology, the development of GaAs-based devices is still desirable because of the availability of the mature GaAs-based technology as well as an improved carrier confinement. Type-I lasers in the 1.3 μm wavelength regime were demonstrated on GaAs substrate using different active material systems. However, the performance of these NIR lasers is, among other reasons, limited by Auger losses [2].

As a result, type-II band alignments were suggested in order to suppress Auger losses [3] and to enable a more flexible band structure engineering. The charge carrier recombination in such quantum mechanical systems occurs across an interface between two adjacent materials. An example for such a type-II band alignment is the (GaIn)As/Ga(AsSb) material system where the electrons are confined in the (GaIn)As quantum well (QW) and the holes are confined in the Ga(AsSb) QW.

Type-II electrical injection lasing from these structures was reported in the NIR regime on GaAs substrates [4]. However, laser devices in the NIR regime exhibited a low output power of 140 mW per facet [4] or laser emission from a type-I instead of a type-II transition [5]. These results highlight the necessity of a careful device design using suitable microscopic models.

In addition to structures based on double QWs, an approach employing a 'W'-type structure in which a Ga(AsSb) QW is embedded in between two adjacent (GaIn)As QWs was proposed for laser applications in the NIR regime. First broad-area laser devices with threshold current densities of $j_{\text{th}} = 0.37 \text{ kA/cm}^2$ as well as internal efficiencies of $\eta_i = 42\%$ and internal losses of $\alpha_i = 11 \text{ cm}^{-1}$ at 1.3 μm were realised using molecular beam epitaxy [6].

Our recent experiments applying metal organic vapour phase epitaxy (MOVPE) have shown great promise due to a strong photoluminescence from these structures as well as a good agreement between experimental spectroscopic data and a fully microscopic theory [7]. Furthermore, the theoretical investigation predicted significant material gain values. In addition, the predicted type-II transitions between the electron and the hole ground state (e1h1), the first excited electron and the first excited hole state (e2h2), and the electron ground state and the second excited hole state (e1h3) in 'W'-QWs, were confirmed [8]. The characterisation of an optically pumped vertical-external-cavity surface-emitting laser (VECSEL) yielded a successful demonstration of lasing from the e1h1 type-II transition with a maximum continuous wave output power of 4 W [9].

In this publication, highly efficient electrical injection (GaIn)As/Ga(AsSb)/(GaIn)As single 'W'-QW lasers are designed based on a fully microscopic theory and realised using MOVPE. The electroluminescence (EL) as well as the laser characteristics are evaluated in detail.

Theoretical modelling and experimental setup: The theoretical analysis of the samples is carried out using a fully microscopic theory as described by Berger *et al.* in [7]. The only input parameters required

for this theoretical approach are the nominal material parameters like thicknesses and concentrations in the specific QWs which can be extracted directly from high-resolution X-ray diffraction measurements.

The growth process is carried out in an AIXTRON AIX 200 GFR (Gas Foil Rotation) reactor system using triethylgallium, trimethylindium, and trimethylaluminium as group III, tertiarybutylarsine (TBAs) and triethylantimony as group V, and tetrabromomethane (CBr₄) and diethyltellurium as dopant sources, respectively. The reactor pressure is set to 50 mbar and high-purity H₂ is used as carrier gas. The native oxide layer is removed from the n-GaAs (001) ($\pm 0.1^\circ$) substrate by applying a TBAs-stabilised bake-out procedure.

While the (GaIn)As/Ga(AsSb)/(GaIn)As single 'W'-QW active region is grown at a temperature of 550°C, the n-GaAs buffer, the n- and p-(AlGa)As claddings, the undoped GaAs separate confinement heterostructures (SCH), and the p⁺-GaAs cap are grown at a temperature of 625°C. The p-(AlGa)As layer is carbon-doped by employing a decreased V/III ratio instead of using CBr₄ as dopant source.

The 1.4 μm (Al_{0.4}Ga_{0.6})As cladding layers together with the 0.2 μm GaAs SCH layers serve as waveguide structure in order to confine the optical mode towards the active region. The active region itself consists of a 4 nm Ga(As_{0.8}Sb_{0.2}) and two 6 nm (Ga_{0.8}In_{0.2})As QWs. A highly doped p⁺-GaAs cap serves as contact layer in order to ensure small contact resistances. Gain guided devices are processed by thinning the sample to 150 μm , evaporating 100 μm wide gold strips onto the p⁺-GaAs cap, and a large-area gold contact onto the n-GaAs substrate. In addition, the remaining part of the p⁺-GaAs cap in between the top metal contacts is wet chemically etched off in order to prevent lateral current spreading. The resulting sample is cleaved to laser bars with cavity lengths between 800 and 2070 μm . A schematic illustration of the resulting device structure can be found in the inset of Fig. 1.

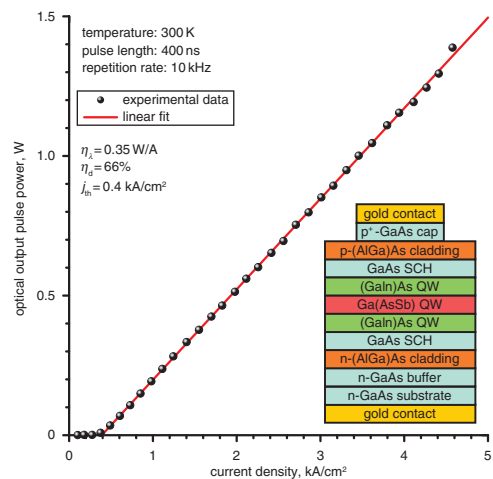


Fig. 1 Optical output pulse power per facet at room temperature of a 930 μm long (GaIn)As/Ga(AsSb)/(GaIn)As single 'W'-QW laser as function of current density. Inset schematically illustrates device structure

An in-depth characterisation is carried out using devices with varying cavity length. All experiments are performed using a pulsed excitation of 400 ns long pulses at a repetition rate of 10 kHz. A large-area germanium photodetector is used to measure the integral single-facet output power as a function of the current. Spectrally resolved EL measurements are carried out using a Yokogawa AQ6370B optical spectrum analyser.

Results: The theoretical analysis is carried out assuming the layer thicknesses and concentrations stated above. In comparison to earlier investigations of 'W'-QW heterostructures employing the (GaIn)As/Ga(AsSb)/(GaIn)As material system [6], different compositions as well as a reduced hole QW thickness are chosen in order to optimise the wave function overlap. Low excitation charge carrier density results in a luminescence peak at 1.19 μm , whereas high excitation charge carrier density generates a gain peak at 1.16 μm .

The optical pulse power measurements of a 930 μm long (GaIn)As/Ga(AsSb)/(GaIn)As single 'W'-QW laser reveal a distinct threshold behaviour at a low threshold current density of $j_{\text{th}} = 0.4 \text{ kA/cm}^2$ at room temperature as shown in Fig. 1. Furthermore, an optical efficiency of $\eta_d = 0.35 \text{ W/A}$ per facet is observed resulting in a differential efficiency of $\eta_d = 66\%$, and a pump-limited maximum optical output

power of $P_{\max} = 1.4$ W at a current density of 4.6 kA/cm^2 . In case of a $2070 \text{ }\mu\text{m}$ long laser, an even lower threshold current density of $j_{\text{th}} = 0.1 \text{ kA/cm}^2$ is achieved. These properties are similar to values obtained using type-I (GaIn)As lasers at a similar wavelength [10].

To prove that the laser emission is based on the e1h1 type-II transition spectrally resolved EL measurements are presented in Fig. 2. The considerable blue shift observed below laser threshold is in agreement with our theoretical results as well as those published in the literature [6]. An average blue shift of $(93 \pm 14) \text{ meV/(kA/cm}^2)$ is observed between 0.10 and 0.38 kA/cm^2 due to the charge carrier separation in type-II heterostructures [6, 7].

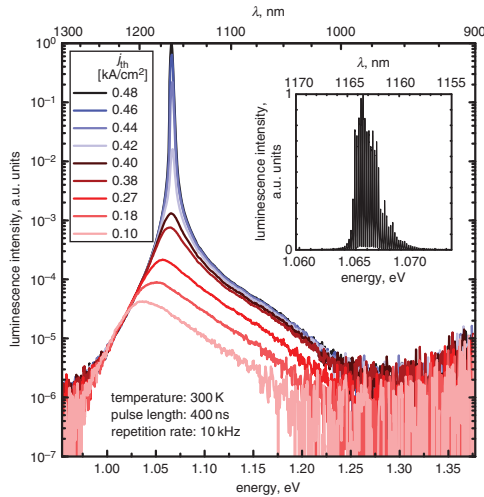


Fig. 2 Spectrally resolved EL measurements at room temperature of a $930 \text{ }\mu\text{m}$ long (GaIn)As/Ga(AsSb)/(GaIn)As single 'W'-QW laser for different current densities directly below (0.10 – 0.40 kA/cm^2 , red) and above (0.42 – 0.48 kA/cm^2 , blue) laser threshold. High resolution measurement of laser mode at 0.48 kA/cm^2 is presented in the inset

The predicted material gain is corroborated by the low threshold laser operation starting from a current density of 0.4 kA/cm^2 for a cavity length of $930 \text{ }\mu\text{m}$ and 0.1 kA/cm^2 for a cavity length of $2070 \text{ }\mu\text{m}$, respectively. No type-I transitions are observed for the entire current range in the LED or laser operation regime up to current densities of 4.6 kA/cm^2 . A shoulder on the high energy side of the spectra occurs as shown in Fig. 2. This transition is several orders of magnitude weaker than the actual laser mode and the spectral position is in good agreement with the e2h2 type-II transition around $1.08 \text{ }\mu\text{m}$ that was calculated for this particular active region.

Laser operation is confirmed by measuring the high-resolution mode spectrum at 0.48 kA/cm^2 which is shown in the inset of Fig. 2. The measurement reveals a laser mode at 1164 nm and a mode spacing of 0.193 nm for the laser cavity length of $930 \text{ }\mu\text{m}$.

In addition, the internal losses α_i of these lasers are determined by analysing the cavity length dependence of the differential efficiencies. For this purpose, devices of different cavity lengths are characterised assuming an end-mirror reflectivity of $R = 0.3$. Multiple measurements of different laser devices are carried out for each cavity length and the results are averaged. The evaluation is performed using these average values and results in internal losses of only $\alpha_i = (1.9 \pm 0.5) \text{ cm}^{-1}$ and an internal efficiency of $\eta_i = (66 \pm 4) \%$.

Conclusion: The careful device design and optimisation using a fully microscopic theory has resulted in highly efficient interface-dominated lasers in the $1.2 \text{ }\mu\text{m}$ wavelength regime based on the type-II band alignment in (GaIn)As/Ga(AsSb)/(GaIn)As 'W'-QWs. An average blue shift of $93 \text{ meV/(kA/cm}^2)$ in the LED regime was observed which is in agreement with theoretical modelling. The MOVPE-grown single 'W'-QW

edge-emitting lasers exhibited a high differential efficiency of 66% , a low threshold current density of 0.4 kA/cm^2 , a pump-limited maximum optical output pulse power of 1.4 W as well as internal losses of only 1.9 cm^{-1} for a cavity length of $930 \text{ }\mu\text{m}$. A threshold current density of only 0.1 kA/cm^2 was observed in case of a cavity length of $2070 \text{ }\mu\text{m}$. No indications for type-I related transitions are observed in this optimised single 'W'-QW material system in the studied operation regime up to 4.6 kA/cm^2 . Due to these promising properties at $1.2 \text{ }\mu\text{m}$, a further optimisation and adjustment of these structures should be carried out in order to demonstrate improved performance also at a wavelength of $1.3 \text{ }\mu\text{m}$.

Acknowledgments: The Marburg work was a project of Sonderforschungsbereich 1083 funded by Deutsche Forschungsgemeinschaft (DFG). The work at Nonlinear Control Strategies Inc. was supported by the Air Force Office of Scientific Research under the STTR Phase II, Grant # FA9550-16-C-0021. The work at the University of Arizona was supported by the U.S. Air Force Office of Scientific Research, Contract # FA9550-14-1-0062.

© The Institution of Engineering and Technology 2016

Submitted: 3 August 2016 E-first: 11 October 2016

doi: 10.1049/el.2016.2851

One or more of the Figures in this Letter are available in colour online.

C. Fuchs, C. Berger, C. Möller, M. Weseloh, S. Reinhard, S.W. Koch and W. Stolz (Materials Sciences Center and Department of Physics, Philipps-Universität Marburg, Renthof 5, 35032 Marburg, Germany)

✉ E-mail: christian.fuchs@physik.uni-marburg.de

J. Hader and J.V. Moloney (Nonlinear Control Strategies Inc., 7040 N Montecatina Drive, Tucson, AZ 85704, USA)

J. Hader and J.V. Moloney: Also with College of Optical Sciences, University of Arizona, Tucson, AZ 85721, USA

References

- Murphy, E.: 'The semiconductor laser: Enabling optical communication', *Nat. Photon.*, 2010, **4**, (5), p. 287, doi: 10.1038/nphoton.2010.107
- Meyer, J.R., Felix, C.L., Bewley, W.W., *et al.*: 'Auger coefficients in type-II InAs/Ga $^{1-x}$ In x Sb quantum wells', *Appl. Phys. Lett.*, 1998, **73**, (20), pp. 2857–2859, doi: 10.1063/1.122609
- Zegrya, G.G., and Andreev, A.D.: 'Mechanism of suppression of Auger recombination processes in type-II heterostructures', *Appl. Phys. Lett.*, 1995, **67**, (18), pp. 2681–2683, doi: 10.1063/1.114291
- Klem, J.F., Blum, O., Kurtz, S.R., Fritz, I.J., and Choquette, K.D.: 'GaAsSb/InGaAs type-II quantum wells for long-wavelength lasers on GaAs substrates', *J. Vac. Sci. Technol. B*, 2000, **18**, (3), pp. 1605–1608, doi: 10.1116/1.591437
- Zvonkov, B.N., Nekorkin, S.M., Vikhrova, O.V., and Dikareva, N.V.: 'Emission properties of heterostructures with a (GaAsSb-InGaAs)/GaAs bilayer quantum well', *Semiconductors*, 2013, **47**, (9), pp. 1219–1223, doi: 10.1134/S1063782613090261
- Chow, W.W., Blum Spahn, O., Schneider, H.C., and Klem, J.F.: 'Contributions to the large blue emission shift in a GaAsSb type-II laser', *J. Quant. Electron.*, 2001, **37**, (9), pp. 1178–1182, doi: 10.1109/3.945323
- Berger, C., Möller, C., Hens, P., *et al.*: 'Novel type-II material system for laser applications in the near-infrared regime', *AIP Adv.*, 2015, **5**, (4), p. 047105, doi: 10.1063/1.4917180
- Gies, S., Kruska, C., Berger, C., *et al.*: 'Excitonic transitions in highly efficient (GaIn)As/Ga(AsSb) type-II quantum-well structures', *Appl. Phys. Lett.*, 2015, **107**, (18), p. 182104, doi: 10.1063/1.4935212
- Möller, C., Fuchs, C., Berger, C., *et al.*: 'Type-II VECSEL with watt level output powers at $1.2 \text{ }\mu\text{m}$ ', *Appl. Phys. Lett.*, 2016, **108**, (7), p. 071102, doi: 10.1063/1.4942103
- Tansu, N., Chang, Y.L., Takeuchi, T., *et al.*: 'Temperature analysis and characteristics of highly strained InGaAs-GaAsP-GaAs ($\lambda > 1.17 \text{ }\mu\text{m}$) quantum-well lasers', *J. Quant. Electron.*, 2002, **38**, (6), pp. 640–651, doi: 10.1109/JQE.2002.1005415

6.3 Publication 3

Citation

C Möller, C Fuchs, C Berger, A Ruiz Perez, M Koch, J Hader, J V Moloney, S W Koch, and W Stolz. Type-II VECSEL with Watt Level Output Powers at 1.2 μm . *Appl. Phys. Lett.*, 108(7):071102, 2016. doi: 10.1063/1.4942103¹⁰⁸

Reproduced with the permission of AIP Publishing.

Abstract

Semiconductor laser characteristics based on type-II band-aligned quantum well heterostructures for the emission at 1.2 μm are presented. Ten “W”-quantum wells consisting of GaAs/(GaIn)As/Ga(AsSb)/(GaIn)As/GaAs are arranged as resonant periodic gain in a vertical-external-cavity surface-emitting laser. Its structure is analyzed by X-ray diffraction, photoluminescence, and reflectance measurements. The laser’s power curves and spectra are investigated. Output powers at Watt level are achieved, with a maximum output power of 4 W. It is confirmed that laser operation only involves the type-II transition. A blue shift of the material gain is observed while the modal gain exhibits a red shift.

Contributions

Christoph Möller carried out the VECSEL design process, the processing, and the spectroscopic characterization of the type-II VECSEL chip. Christian Fuchs realized the RPG structure using MOVPE based on the design proposal and structurally analyzed it using HR-XRD. Christian Berger supported the work by applying a fully microscopic theory in order to calculate gain and luminescence spectra. Antje Ruiz Perez performed the MOVPE growth of the cap and the DBR based on the design proposal. Christoph Möller wrote the manuscript. Martin Koch, Jörg Hader, Jerome V. Moloney, Stephan W. Koch, and Wolfgang Stolz supervised the work and secured the funding to support this study. All authors reviewed the manuscript.

Type-II vertical-external-cavity surface-emitting laser with Watt level output powers at 1.2 μm

C. Möller,^{1,a)} C. Fuchs,¹ C. Berger,¹ A. Ruiz Perez,² M. Koch,¹ J. Hader,³ J. V. Moloney,³ S. W. Koch,¹ and W. Stolz^{1,2}

¹Department of Physics and Material Sciences Center, Philipps-Universität Marburg, Renthof 5, 35032 Marburg, Germany

²NAsP_{III/IV} GmbH, Hans-Meerwein-Straße, 35032 Marburg, Germany

³Nonlinear Control Strategies, Inc., 7040 N Montecatina Drive, Tucson, Arizona 85704, USA

(Received 3 December 2015; accepted 4 February 2016; published online 16 February 2016)

Semiconductor laser characteristics based on type-II band-aligned quantum well heterostructures for the emission at 1.2 μm are presented. Ten “W”-quantum wells consisting of GaAs/(GaIn)As/Ga(AsSb)/(GaIn)As/GaAs are arranged as resonant periodic gain in a vertical-external-cavity surface-emitting laser. Its structure is analyzed by X-ray diffraction, photoluminescence, and reflectance measurements. The laser’s power curves and spectra are investigated. Output powers at Watt level are achieved, with a maximum output power of 4 W. It is confirmed that laser operation only involves the type-II transition. A blue shift of the material gain is observed while the modal gain exhibits a red shift. © 2016 AIP Publishing LLC. [<http://dx.doi.org/10.1063/1.4942103>]

Many applications have a demand for lasers in the infrared regime. Prominent examples are telecommunication and optical data transfer where the wavelength of light sources has to be adapted to the available propagation media.¹ For instance, a minimum absorption in optical fibers is around 1.3 μm .² Other examples are frequency doubling for red emitters in digital projectors, where wavelengths above 1.2 μm are of particular interest, or medical applications.³ In the latter case, eye-safe emitters with wavelengths above 1.4 μm are desired where the corneal absorption can provide a natural protection of the retina.⁴

In the infrared, above 1.2 μm , conventional semiconductor lasers with gain media based on type-I quantum well heterostructures suffer from significant non-radiative Auger losses.⁵ In recent years, type-II band-aligned quantum wells have become a promising alternative. Especially, “W”-quantum well heterostructures have been considered which, despite the spatial separation of electrons and holes, still provide sufficient overlap between the electron and hole wave functions.^{6–9} In comparison to type-I systems, a type-II band alignment enables a more flexible band structure engineering in order to reduce intrinsic losses while the emission wavelength can be kept constant. Thus, such type-II lasers are promising candidates to surpass conventional type-I lasers with respect to wavelength versatility and performance in the infrared regime. To date, first lasers based on type-II quantum well heterostructures have been reported based on the InP, GaSb, and GaAs material systems with emission wavelengths even in the mid infrared.^{10–13} Particularly, at an emission wavelength of 1.2 μm , an edge emitter with a maximum output power of 50 mW at 20 °C was demonstrated.¹⁰

Recently, we have evaluated the potential of the GaAs/(GaIn)As/Ga(AsSb)/(GaIn)As/GaAs material system as gain medium for vertical-external-cavity surface-emitting lasers (VECSELs) with an emission wavelength of 1.2 μm .¹⁴

Photoluminescence (PL) spectra of such type-II multiple quantum well heterostructures (MQWHs) were measured and compared with the results from a fully microscopic theory. The involved excitonic transitions could be identified in an experiment–theory comparison for photomodulation reflectance spectroscopy measurements.¹⁵ Based on the good agreement between the experimental and theoretical results, also the absorption and gain properties were calculated using the semiconductor Bloch equations. Gain values as high as for type-I systems were predicted. Overall, it is expected that the previously investigated “W”-design will perform well as gain medium in optically pumped semiconductor lasers.

In this letter, we demonstrate a continuous wave pumped type-II semiconductor disk laser with an emission wavelength of 1.2 μm at room temperature. Therefore, we take on our previous approach and implement a GaAs/(Ga_{0.8}In_{0.2})As/Ga(As_{0.8}Sb_{0.2})/(Ga_{0.8}In_{0.2})As/GaAs 10× MQWH as resonant periodic gain structure. The sample growth is carried out by metalorganic vapor phase epitaxy (MOVPE) using a commercial horizontal AIXTRON AIX 200 Gas Foil Rotation (GFR) system.¹⁴ In preparation for the growth of the laser structure, a type-I (Ga_{0.8}In_{0.2})As/GaAs MQWH and a Ga(As_{0.8}Sb_{0.2})/GaAs MQWH are grown, in order to determine the individual growth conditions which are used for the growth of the type-II MQWH. The laser structure is grown bottom-up onto (001) GaAs substrate, starting with a (Ga_{0.52}In_{0.48})P capping layer and followed by the resonant periodic gain containing the “W”-quantum wells separated by Ga(AsP) strain compensating layers. The optical layer thicknesses of the capping layer and the barriers are matched to $\lambda/2$ with respect to the lasing wavelength. Finally, a distributed Bragg reflector (DBR) is grown, with 22 1/2 pairs of (Al_{0.1}Ga_{0.9})As/AlAs.

As in our previous work, the MQWHs are characterized using high resolution X-ray diffraction (HR-XRD). The determined In and Sb concentrations as well as the (GaIn)As and Ga(AsSb) layer thicknesses are summarized in Table I.

^{a)}Electronic mail: christoph.moeller@physik.uni-marburg.de

TABLE I. Measured In and Sb concentrations and layer thicknesses of the investigated MQWHs (i) (GaIn)As/GaAs, (ii) Ga(AsSb)/GaAs, and (iii) GaAs/(GaIn)As/Ga(AsSb)/(GaIn)As/GaAs.

	(i)	(ii)	(iii)
QW thickness (nm)	5.2	4.1	5.5/4.0/5.5
In concentration (%)	20.8	0	20.3/0/20.3
Sb concentration (%)	0	19.8	0/19.8/0

Furthermore, we record the PL spectra of all three structures. Regular PL measurements are performed with the (GaIn)As/GaAs and the Ga(AsSb)/GaAs MQWHs, where excitation and detection are carried out perpendicular to the surface of the sample. However, for VECSELs, it is more meaningful to record the edge PL, where the filtering by the Fabry-Pérot resonances from the microcavity, which is formed by the capping layer and the DBR, is avoided.¹⁶ Therefore, we excite through the ternary DBR using an 808 nm diode laser and detect the PL under an angle of 90°, i.e., only the PL emitted from the edge of the sample, with an optical spectrum analyzer (Yokagawa AQ6370B). The normalized spectra are presented in Fig. 1. It is observed that the characteristic PL of the type-I transitions according to recombinations inside an individual layer in the “W”-structure is suppressed. Overall, the HR-XRD and edge PL measurement of the VECSEL show that a MQWH very similar to the previously investigated structures was realized. Hence, the observed luminescence can be related to type-II transitions for which gain is expected.^{14,15}

One important requirement for VECSELs is to match the material gain peak wavelength and the microcavity resonance. For type-I setups, it is known that the red shift of the material gain is stronger than the red shift of the microcavity. Thus, following the definition of Hader *et al.*,¹⁷ a negative detuning is usually introduced for type-I VECSELs in order to achieve an efficient laser operation. This detuning can be used as design parameter to achieve a low threshold or high output power.

Due to the importance of the microcavity, the reflectivity of a processed laser chip is measured in order to evaluate the longitudinal confinement factor, i.e., the average light field intensity at the quantum wells. For the reflection measurement, a

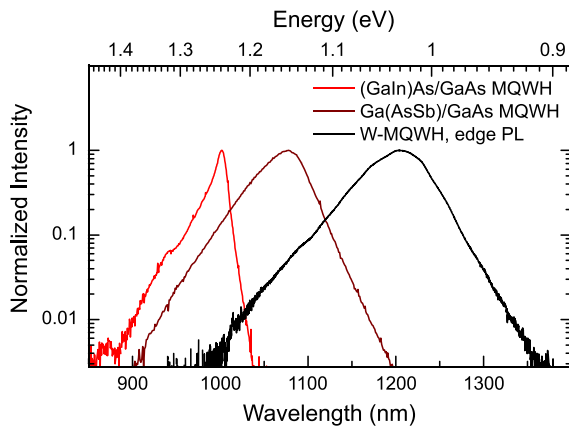


FIG. 1. Photoluminescence of the (GaIn)As/GaAs (red line) and Ga(AsSb)/GaAs (dark red line) $10 \times$ MQWH test structures as well as the edge PL of the laser sample with 10 GaAs/(GaIn)As/Ga(AsSb)/(GaIn)As/GaAs “W”-quantum wells arranged as resonant periodic gain (black line).

sample from an adjacent wafer position of the edge PL sample is flip-chip bonded onto a 350 μm thick chemical vapor deposition (CVD) diamond heat spreader via solid liquid interdiffusion bonding based on Au and In. Then, the substrate is removed by selective chemical wet etching onto the Ga(InP) capping layer. The processed VECSEL chip is mounted on a temperature controlled copper heat sink. To measure the reflectivity white light is focussed perpendicular to the processed chip and a beamsplitter is used to collect the reflected light in a spectrum analyzer.

The reflectivity measurement is shown as grey-shaded area in Fig. 2. An absorption dip within the DBR stop band is observed at 1168 nm. For the reflectivity simulation, the barrier and QW thicknesses are extracted from the HR-XRD results. The capping layer and the DBR layer thicknesses are varied in order to fit the experimental data by the transfer-matrix method.¹⁶ Consequently, the intensity distribution of the light field within the structure can be calculated, and the longitudinal confinement factor is determined. It is found that the drop of the measured reflectance at the short-wavelength side of the stop band is in agreement with the maximum of the longitudinal confinement factor. This also explains the deviation of the simulated reflectivity where the absorption of the QWs is not considered.

The comparison between the edge PL (cf. Fig. 1) and the reflectance as well as the simulation of the longitudinal confinement factor reveals that a large positive detuning of about 35 nm is present in this particular type-II VECSEL structure. This is in contrast to common type-I VECSELs where no laser operation should be achieved with such a detuning.¹⁷ However, for type-II quantum wells the exact carrier density and temperature dependent shift rates are not yet established. Still, it has been reported that a significant blue shift is obtained with increasing pump densities despite the simultaneous heating of the gain structure.^{10,18} These observations are also consistent with our recent investigations concerning the GaAs/(GaIn)As/Ga(AsSb)/(GaIn)As/GaAs material system.¹⁴

An outcoupling mirror with -100 mm radius of curvature is used to arrange a linear laser cavity with a length of 64 mm. The VECSEL is driven by an 808 nm diode pump laser (JenOptik JOLD-400-CAXF-6P2) under a 30° angle of incidence. A CCD camera was utilized to record the pump spot

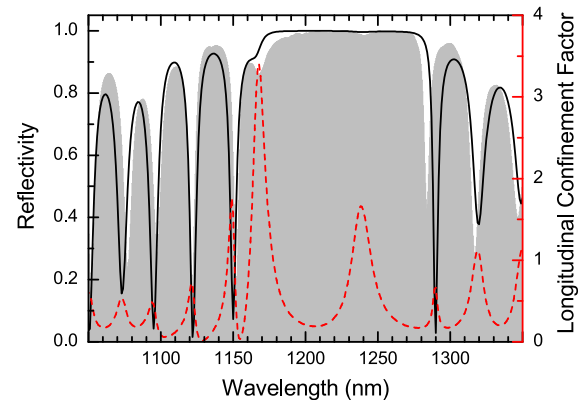


FIG. 2. Reflectivity measurement (grey-shaded area), reflectivity simulation (black solid line), and simulated longitudinal confinement factor (red dashed line) of the processed laser structure.

profile, and a super-Gaussian fit is applied in order to estimate the exact pump intensity. The complete procedure is described in more detail by Heinen *et al.*¹⁹ At full width at half maximum (FWHM), the elliptical pump spot is of the size $750\text{ }\mu\text{m} \times 870\text{ }\mu\text{m}$, which implies highly multi-transverse mode operation concerning the VECSEL. For comparison, the TEM_{00} mode size at the VECSEL chip for this cavity configuration is $270\text{ }\mu\text{m}$ at FWHM. It is found that the pump spot exhibits a flat-top profile with a super-Gaussian order of $m = 3.00$. Hence, it is valid to estimate the pump intensity directly from the pump spot radius.¹⁹

Laser operation is achieved with output coupler transmissivities of 0.2%, 0.7%, 1.0%, and 1.5%. The best performance is observed with the 0.7% output coupler for which the laser power curves are recorded with different heat sink temperatures in 15°C steps between -15°C and 30°C (cf. Fig. 3). The net input power is denoted at the bottom x-axis, considering that measured 23.2% of the pump light is reflected. The net pump intensity is denoted at the top x-axis. At -15°C heat sink temperature, the maximum output power of 4 W is achieved, and the threshold pump intensity is 1.18 kW/cm^2 . With increasing temperature, the threshold is continuously increasing to 1.43 kW/cm^2 , 1.92 kW/cm^2 , and 2.54 kW/cm^2 while maximum output powers are decreasing to 2.8 W, 1.6 W, and 0.6 W, for 0°C , 15°C , and 30°C , respectively.

In comparison to a type-I VECSEL in the same wavelength regime, the pump intensities at threshold are in the same order of magnitude. On the other hand, the slope efficiencies of less than 10% for the type-II structure are clearly smaller as in type-I systems with 31%–34% slope efficiency.^{20,21}

The optical spectrum analyzer is used to record the laser spectra while the power curve with 0°C heat sink temperature is recorded. The measurement is shown as false color plot in Fig. 4. The wavelength at lasing threshold is 1173 nm. A continuous red shift of the laser spectrum is observed although a blue shift of the material gain must be present due to the compensation of the large positive detuning. At the peak output power, a maximum wavelength of 1182 nm is observed. This result indicates that the maximum of the modal gain is dominated by the longitudinal confinement factor. If a linear shift of 0.12 nm/K is assumed, which

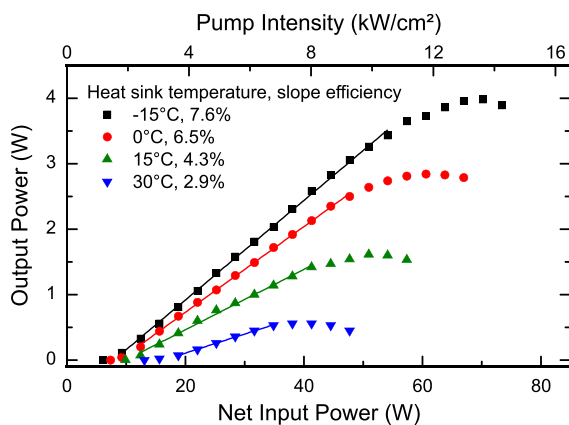


FIG. 3. Input/output characteristics for heat sink temperatures ranging from -15°C to 30°C .

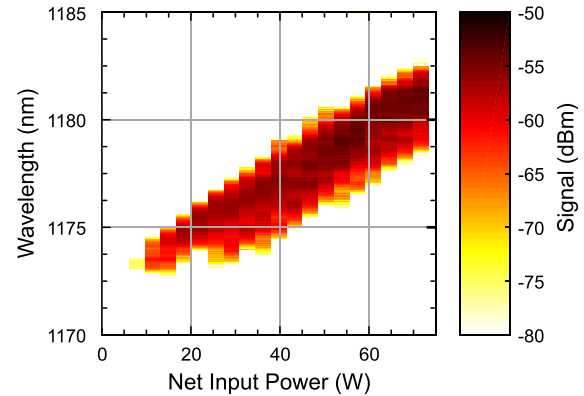


FIG. 4. Laser spectra corresponding to the power curve with 0°C heat sink temperature.

is a common value for the spectral shift of the reflectivity of such resonant periodic gain structures, temperatures of 60°C at threshold and 135°C at the maximum applied pump intensity are estimated. These values are similar to typical temperatures in type-I VECSELs.²²

In conclusion, we have demonstrated the feasibility of a VECSEL based on a type-II resonant periodic gain at $1.2\text{ }\mu\text{m}$ emission wavelength. It emits up to 4 W at -15°C and 1.6 W at 15°C heat sink temperature with an emission wavelength between 1173 nm and 1182 nm. Measurements confirm lasing at the type-II transitions. The detuning is estimated by a comparison of the edge PL and reflectivity measurement. In accordance to previous reports, we have observed a significant blue shift of the material gain because the positive detuning of 35 nm between the low density PL peak wavelengths and the microcavity resonance is compensated. However, the red shift of the laser wavelength indicates that the modal gain is dominated by the microcavity resonance. The observed characteristic of decreasing thresholds and increasing slope efficiencies for reduced heat sink temperatures cannot only be an indicator for an increasing material gain but also for an improved overlap of material gain with the microcavity resonance. As for type-I systems, it is expected that the performance of type-II VECSELs is critically depending on the detuning. Therefore, an optimized design concerning the detuning of a type-II setup can potentially lead to a significant improvement of the laser performance. The characteristic blue shift of type-II structures with increasing carrier densities implies that the optimization of type-II VECSELs is completely different from the well established type-I VECSEL.

The presented results will facilitate the realization of more efficient lasers based on the GaAs/(GaIn)As/Ga(AsSb)/(GaIn)As/GaAs material system. In order to exploit the full potential, optimizations can be performed in interplay of experiment and theoretical quantum design,²³ but also with respect to optimized growth conditions. Furthermore, the design based on this material system has the potential for emission wavelengths up to $1.4\text{ }\mu\text{m}$ and beyond.

The Marburg work was a project of the Sonderforschungsbereich 1083 funded by the Deutsche Forschungsgemeinschaft (DFG). The work at Nonlinear

Control Strategies, Inc. is supported via STTR Phase II, Contract No. FA9550-13-C-0009. The work from J. Hader and J. V. Moloney was also supported by the U.S. Air Force Office of Scientific Research (AFOSR), contract FA9550-14-1-0062.

- ¹E. Murphy, *Nat. Photonics* **4**, 287 (2010).
- ²G. P. Agrawal, *Fiber-Optic Communication Systems* (John Wiley & Sons, 2012), Vol. 222.
- ³S. Calvez, J. Hastie, M. Guina, O. Okhotnikov, and M. Dawson, *Laser Photonics Rev.* **3**, 407 (2009).
- ⁴J. A. Zuclich, D. J. Lund, and B. E. Stuck, *Health Phys.* **92**, 15 (2007).
- ⁵J. R. Meyer, C. L. Felix, W. W. Bewley, I. Vurgaftman, E. H. Aifer, L. J. Olafsen, J. R. Lindle, C. A. Hoffman, M.-J. Yang, B. R. Bennett, B. V. Shanabrook, H. Lee, C.-H. Lin, S. S. Pei, and R. H. Miles, *Appl. Phys. Lett.* **73**, 2857 (1998).
- ⁶J. R. Meyer, C. A. Hoffman, F. J. Bartoli, and L. R. Ram-Mohan, *Appl. Phys. Lett.* **67**, 757 (1995).
- ⁷N. Tansu and L. Mawst, *IEEE J. Quantum Electron.* **39**, 1205 (2003).
- ⁸J.-Y. Yeh, L. J. Mawst, A. A. Khandekar, T. F. Kuech, I. Vurgaftman, J. R. Meyer, and N. Tansu, *Appl. Phys. Lett.* **88**, 051115 (2006).
- ⁹J. Hader, J. V. Moloney, S. W. Koch, I. Vurgaftman, and J. R. Meyer, *Appl. Phys. Lett.* **94**, 061106 (2009).
- ¹⁰J. F. Klem, O. Blum, S. R. Kurtz, I. J. Fritz, and K. D. Choquette, *J. Vac. Sci. Technol., B* **18**, 1605 (2000).
- ¹¹R. Kaspi, A. Ongstad, G. C. Dente, J. Chavez, M. L. Tilton, and D. Gianardi, *Appl. Phys. Lett.* **81**, 406 (2002).
- ¹²C.-H. Chang, Z.-L. Li, H.-T. Lu, C.-H. Pan, C.-P. Lee, G. Lin, and S.-D. Lin, *IEEE Photonics Technol. Lett.* **27**, 225 (2015).
- ¹³S. Sprengel, A. Andrejew, F. Federer, G. K. Veerabathran, G. Boehm, and M.-C. Amann, *Appl. Phys. Lett.* **106**, 151102 (2015).
- ¹⁴C. Berger, C. Möller, P. Hens, C. Fuchs, W. Stolz, S. W. Koch, A. R. Perez, J. Hader, and J. V. Moloney, *AIP Adv.* **5**, 047105 (2015).
- ¹⁵S. Gies, C. Kruska, C. Berger, P. Hens, C. Fuchs, A. R. Perez, N. W. Rosemann, J. Veletas, S. Chatterjee, W. Stolz, S. W. Koch, J. Hader, J. V. Moloney, and W. Heimbrodt, *Appl. Phys. Lett.* **107**, 182104 (2015).
- ¹⁶A. Tropper and S. Hoogland, *Prog. Quantum Electron.* **30**, 1 (2006).
- ¹⁷J. Hader, G. Hardesty, G. Hardesty, M. J. Yarborough, Y. Kaneda, J. V. Moloney, B. Kunert, W. Stolz, and S. W. Koch, *IEEE J. Quantum Electron.* **46**, 810 (2010).
- ¹⁸W. W. Chow and H. C. Schneider, *Appl. Phys. Lett.* **78**, 4100 (2001).
- ¹⁹B. Heinen, C. Möller, K. Jandieri, B. Kunert, M. Koch, and W. Stolz, *IEEE J. Quantum Electron.* **51**, 1 (2015).
- ²⁰L. Fan, C. Hessenius, M. Fallahi, J. Hader, H. Li, J. V. Moloney, W. Stolz, S. W. Koch, J. T. Murray, and R. Bedford, *Appl. Phys. Lett.* **91**, 131114 (2007).
- ²¹S. Ranta, M. Tavast, T. Leinonen, N. V. Lieu, G. Fetzter, and M. Guina, *Electron. Lett.* **49**, 59 (2013).
- ²²B. Heinen, F. Zhang, M. Sparenberg, B. Kunert, M. Koch, and W. Stolz, *IEEE J. Quantum Electron.* **48**, 934 (2012).
- ²³J. V. Moloney, J. Hader, and S. W. Koch, *Laser Photonics Rev.* **1**, 24 (2007).

6.4 Publication 4

Citation

C Fuchs, A Brüggemann, M J Weseloh, C Berger, C Möller, S Reinhard, J Hader, J V Moloney, A Bäumner, S W Koch, and W Stolz. High-temperature operation of electrical injection type-II (GaIn)As/Ga(AsSb)/(GaIn)As “W”-quantum well lasers emitting at 1.3 μm . *Sci. Rep.*, 8(1):1422, 2018. doi: 10.1038/s41598-018-19189-1 ¹²⁰

Abstract

Electrical injection lasers emitting in the 1.3 μm wavelength regime based on (GaIn)As/Ga(AsSb)/(GaIn)As type-II double “W”-quantum well heterostructures grown on GaAs substrate are demonstrated. The structure is designed by applying a fully microscopic theory and fabricated using metal organic vapor phase epitaxy. Temperature-dependent electroluminescence measurements as well as broad-area edge-emitting laser studies are carried out in order to characterize the resulting devices. Laser emission based on the fundamental type-II transition is demonstrated for a 975 μm long laser bar in the temperature range between 10 °C and 100 °C. The device exhibits a differential efficiency of 41 % and a threshold current density of 1.0 kA/cm² at room temperature. Temperature-dependent laser studies reveal characteristic temperatures of $T_0 = (132 \pm 3) \text{ K}$ over the whole temperature range and $T_1 = (159 \pm 13) \text{ K}$ between 10 °C and 70 °C and $T_1 = (40 \pm 1) \text{ K}$ between 80 °C and 100 °C.

Contributions

Christian Fuchs conceived the experiments and carried out the epitaxial growth of the laser structures. Christian Fuchs and Anja Brüggemann carried out the experimental device analysis and Christian Fuchs evaluated the experimental data. Christoph Möller supported the spectroscopic experiments. Stefan Reinhard fabricated broad-area edge-emitting lasers. Ada Bäumner, Maria J. Weseloh, and Christian Berger performed the theoretical design studies. Ada Bäumner carried out the actual design analysis presented in this study. Christian Fuchs wrote the manuscript. Jörg Hader, Jerome V. Moloney, Stephan W. Koch, and Wolfgang Stolz supervised the work and secured the funding to support this study. All authors reviewed the manuscript.

SCIENTIFIC REPORTS

OPEN

High-temperature operation of electrical injection type-II (GaIn)As/Ga(AsSb)/(GaIn)As “W”-quantum well lasers emitting at 1.3 μm

C. Fuchs¹, A. Brüggemann¹, M. J. Weseloh¹, C. Berger¹, C. Möller¹, S. Reinhard¹, J. Hader^{2,3}, J. V. Moloney^{2,3}, A. Bäumner¹, S. W. Koch¹ & W. Stolz¹

Electrical injection lasers emitting in the 1.3 μm wavelength regime based on (GaIn)As/Ga(AsSb)/(GaIn)As type-II double “W”-quantum well heterostructures grown on GaAs substrate are demonstrated. The structure is designed by applying a fully microscopic theory and fabricated using metal organic vapor phase epitaxy. Temperature-dependent electroluminescence measurements as well as broad-area edge-emitting laser studies are carried out in order to characterize the resulting devices. Laser emission based on the fundamental type-II transition is demonstrated for a 975 μm long laser bar in the temperature range between 10 °C and 100 °C. The device exhibits a differential efficiency of 41 % and a threshold current density of 1.0 kA/cm² at room temperature. Temperature-dependent laser studies reveal characteristic temperatures of $T_0 = (132 \pm 3)$ K over the whole temperature range and $T_1 = (159 \pm 13)$ K between 10 °C and 70 °C and $T_1 = (40 \pm 1)$ K between 80 °C and 100 °C.

The development of efficient near-infrared lasers emitting at a wavelength of 1.3 μm is of great interest due to their application in optical telecommunications based on the O-band (1.26 μm to 1.36 μm). Present-day telecommunication systems typically use InP-based materials systems such as (GaIn)(AsP)/InP¹ or (AlGaIn)As/InP^{2–5}. While these materials have proven to be a spectrally suitable choice for telecommunication systems, their performance is considerably affected by Auger losses as well as potentially small hetero band offsets. A possible solution to these problems is the application of GaAs-based lasers which typically offer large hetero band offsets and mature (AlGa)As/GaAs-based technology. These improvements can prevent carrier leakage and facilitate the fabrication of sophisticated device structures such as vertical-cavity surface-emitting lasers (VCSELs). However, Auger recombination has to be considered as a loss mechanism which is primarily defined by the electronic structure of the active material. While the application of (GaIn)(NAs)/GaAs^{6–8} or Ga(AsSb)/GaAs^{9–11} as active materials are interesting due to their spectral properties, these materials systems do not provide a distinct route towards the suppression of Auger losses.

Type-II heterostructures were suggested as a possible solution to this problem^{12,13}. The conduction and valence band states are dominated by different materials in these heterostructures and thus, it is possible to independently modify these energy levels which allows for a more flexible band structure engineering and offers the opportunity to tune the Auger coefficients. The successful demonstration of type-II emission based on metal organic vapor phase epitaxy (MOVPE)-grown (GaIn)As/Ga(AsSb) bilayer quantum wells (QWs)¹⁴ was followed by various attempts to fabricate lasers based on these materials. The first demonstration of an electrical injection laser based on a bilayer structure was reported by Klem *et al.*¹⁵. The device exhibited a differential efficiency of 38 % and a maximum optical output pulse power of 0.14 W per facet at a wavelength of 1.17 μm . The first attempt to improve the performance of these devices was reported by Ryu and Dapkus in 2002 by applying “W”-QW heterostructures (“W”-QWH) in order to improve the wave function overlap of the spatially separated electrons and holes¹⁶.

In our previous studies, we applied MOVPE in order to fabricate (GaIn)As/Ga(AsSb)/(GaIn)As “W”-QWHs for near-infrared laser applications. A comparison of experimental and theoretical photoluminescence spectra

¹Materials Sciences Center and Department of Physics, Philipps-Universität Marburg, Renthof 5, 35032, Marburg, Germany. ²Nonlinear Control Strategies Inc., 7040 N. Montecatina Dr., Tucson, AZ, 85704, USA. ³College of Optical Sciences, University of Arizona, 1630 E. University Blvd., Tucson, AZ, 85721, USA. Correspondence and requests for materials should be addressed to C.F. (email: christian.fuchs@physik.uni-marburg.de)

obtained from a fully microscopic theory yielded an excellent agreement. Furthermore, material gain values similar to those of type-I heterostructures were predicted¹⁷. In order to confirm the results obtained from theoretical modeling and to analyze the energy states that are involved in the optical transitions in these “W”-QWHs, photo-modulated reflectance spectroscopy was employed. It was possible to confirm the existence of two bound electron states as well as up to three bound hole states depending on the antimony concentration¹⁸. These novel insights were used to fabricate vertical-external-cavity surface-emitting lasers (VECSELs) operating in the 1.2 μm wavelength regime. A continuous wave output power of 4 W was achieved under multi mode operating conditions¹⁹. Furthermore, an output power of 0.35 W with a beam quality factor below 1.2 under transverse single mode operating conditions was observed at room temperature²⁰. Low threshold electrical injection lasers emitting in the 1.2 μm regime with differential efficiencies of 66 % and a maximum optical output pulse power of 1.4 W per facet were demonstrated using broad-area edge-emitting lasers under pulsed excitation conditions²¹. Additionally, a MOVPE growth study demonstrated the possibility to adapt the design of the active “W”-QWH for emission at 1.3 μm by increasing the antimony concentration to approximately 27 %²².

In the present publication, a fully microscopic theory is applied to optimize the (GaIn)As/Ga(AsSb)/(GaIn)As “W”-QWH for an application as active region in lasers emitting at 1.3 μm . The structure proposed by this design study is fabricated using MOVPE and characterized by spectral measurements below and above laser threshold as well as measurements of laser characteristics in the temperature range between 10 °C and 100 °C.

Results

Theoretical design of the “W”-QWH active region. The “W”-QWH is designed using the fully microscopic theory described by Berger *et al.* in Ref.¹⁷, which was previously applied to various type-I²³ as well as type-II²⁴ materials systems. Only nominal material parameters such as QW thicknesses and compositions are required as input for this approach. The systems used in our previous laser studies consist of 6 nm thick electron and 4 nm thick hole quantum wells containing 20 % In and Sb, respectively, resulting in an emission wavelength of 1.2 μm . This design yields an overall thickness of the electron confinement potential of 16 nm. While the fabrication of these structures is possible, their application is challenging due to higher order type-II transitions that are predicted to dominate the material gain spectra at high charge carrier densities²⁵. This behavior results from the electron energy states being nearly degenerate due to the large thickness of the electron confinement potential¹⁸.

The adaption of the active region for applications at 1.3 μm using the fully microscopic theory yields concentrations of 22 % In and 28 % Sb while maintaining layer thicknesses of 6 nm and 4 nm, respectively. Furthermore, the microscopic theory is applied to calculate the indium concentration that is required to retain a constant emission wavelength while decreasing the (GaIn)As QW thicknesses in order to increase the energetic separation between the electron ground state and the first excited electron state. A thickness of 4 nm is chosen since the increase in quantization energy requires an experimentally accessible indium concentration of 28 %. The Ga(AsSb) QW remains unchanged with an antimony concentration of 28 % and a thickness of 4 nm. Altogether, these changes result in a low excitation density photoluminescence peak at a wavelength of 1.34 μm for a carrier density of $0.002 \times 10^{12}/\text{cm}^2$, a material gain value of 750/cm at a wavelength of 1.31 μm and a separation of the electron ground state and the first excited electron state of 22 meV for a carrier density of $3.0 \times 10^{12}/\text{cm}^2$. A comparison with the reference structure consisting of 6 nm thick (GaIn)As QWs containing 22 % indium and the same Ga(AsSb) QW yields improvements of the energetic separation of the electron ground state and the first excited electron state of 38 % as well as of the material gain value of 66 % at the above mentioned carrier density. Additionally, the strain thickness product per “W”-QWH is decreased by 11 % allowing for a more flexible device design in highly strained devices such as VECSELs¹⁹.

Temperature-dependent spectral properties. Room temperature electroluminescence (EL) spectra of a 975 μm long (GaIn)As/Ga(AsSb)/(GaIn)As double “W”-QWH laser are shown in Fig. 1. The EL peak wavelength shifts from 1.320 μm at a current density of 0.1 kA/cm² to 1.278 μm at 0.84 kA/cm². A linear fit yields a blue shift of (42 ± 7) meV/(kA/cm²) which was also observed in previous laser studies²¹ and thoroughly analyzed using microscopic models^{17,25,26}. The mode narrowing starting from 0.84 kA/cm² results in laser operation at 1.275 μm . Thus, the double “W”-QWH design used for this device efficiently suppresses higher order type-II transitions by establishing suitable charge carrier densities per “W”-QWH.

Temperature-dependent spectral laser measurements directly above laser threshold are carried out in order to verify that the laser emission is based on the fundamental type-II transition up to a temperature of 100 °C. Therefore, the emission directly above laser threshold is analyzed for temperatures between 10 °C and 100 °C. The resulting spectra are presented in Fig. 2. A temperature-induced average shift rate of 0.28 nm/K is observed corresponding to a shift of the emission wavelength from 1.272 μm (10 °C) to 1.296 μm (100 °C). However, no switching to higher order type-II transitions is observed and thus, stable laser operation based on the fundamental type-II transition up to a temperature of 100 °C is obtained using the present design.

Temperature-dependent laser studies. The knowledge of the emission wavelengths enables the measurement of laser characteristics using an appropriate detector calibration for each temperature. Laser characteristics of a 975 μm long (GaIn)As/Ga(AsSb)/(GaIn)As double “W”-QWH laser are shown in Fig. 3 for temperatures between 10 °C and 100 °C. The room temperature measurement (20 °C) is carried out before and after the temperature series in order to verify that no device degradation occurs during the temperature series. A differential efficiency of 41 %, a threshold current density of 1.0 kA/cm², and a maximum optical output pulse power of 0.68 W per facet at a power supply-limited current density of 4.5 kA/cm² are observed at a wavelength of 1.275 μm . Furthermore, simple cavity length dependent studies of the present laser structure yield internal losses of $(0.7 \pm 1.6)/\text{cm}$ and an internal efficiency of $(37.1 \pm 6.4)\%$ at a temperature of 20 °C. While this low internal loss value is excellent, additional experiments are underway in order to analyze whether cavity length dependent studies are an appropriate tool for

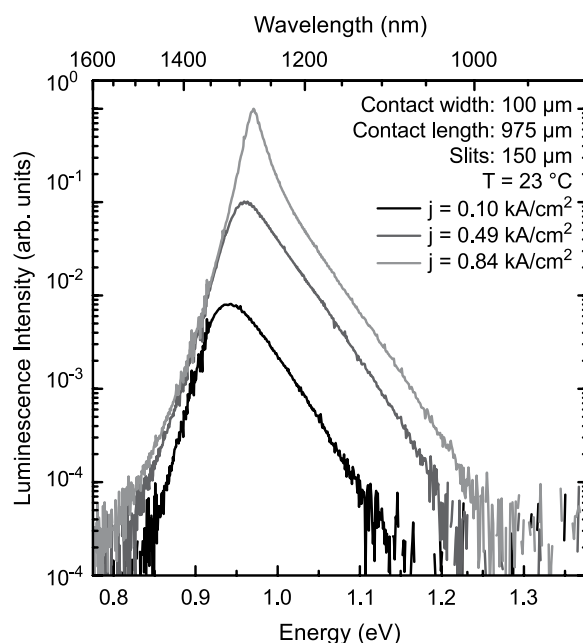


Figure 1. EL spectra of a 975 μm long (GaIn)As/Ga(AsSb)/(GaIn)As double “W”-QWH laser at a temperature of 23 $^{\circ}\text{C}$. All spectra shown here are recorded below laser threshold for current densities between 0.10 kA/cm^2 and 0.84 kA/cm^2 . The spectra are normalized with respect to the 0.84 kA/cm^2 measurement and monochromator slit widths of 150 μm are used for all measurements.

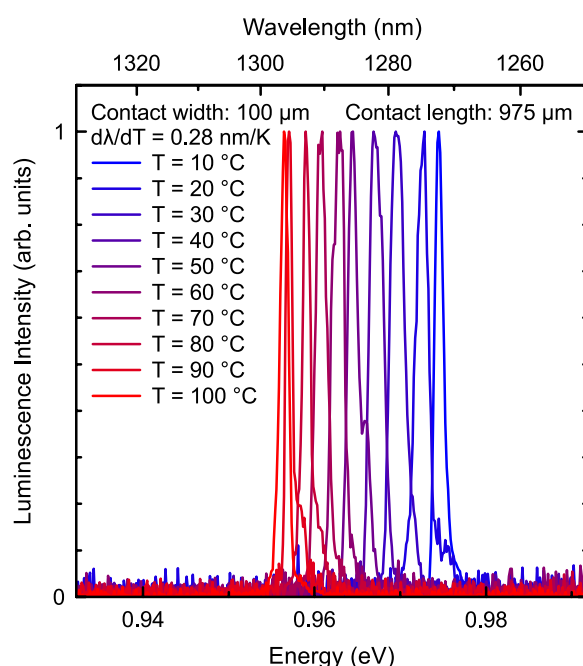


Figure 2. Normalized laser spectra directly above laser threshold of a 975 μm long (GaIn)As/Ga(AsSb)/(GaIn)As double “W”-QWH laser for temperatures between 10 $^{\circ}\text{C}$ and 100 $^{\circ}\text{C}$. A linear fit of the peak wavelengths yields a shift rate of 0.28 nm/K .

the characterization of internal losses in type-II lasers^{1,4,5}. A possible reason for deviations may be the fact that the confinement potentials are distorted as charge carriers are filled into the active region resulting in a strong carrier density dependence of the wave functions. Thus, the internal efficiency as well as the internal losses might strongly depend on the actual carrier density in the type-II active region. Laser operation is obtained up to a setup-limited temperature of 100 $^{\circ}\text{C}$ and an output power of 0.18 W is achieved at this temperature. Thus, the present device concept can be utilized under the typical operating conditions found in telecommunication laser applications.

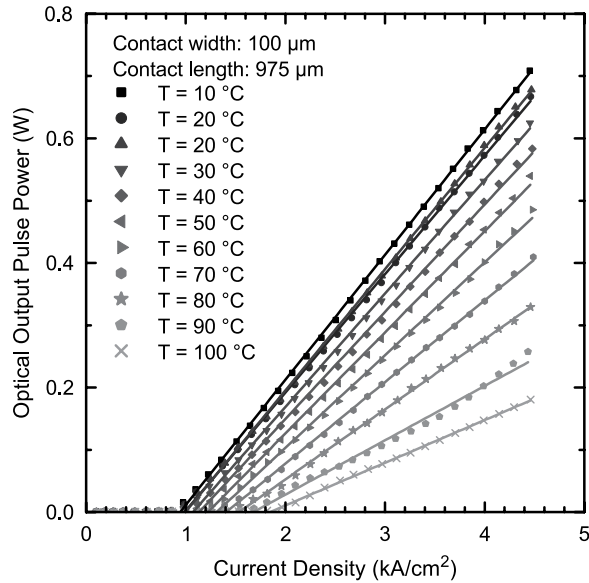


Figure 3. Laser characteristics of a 975 μm long (GaIn)As/Ga(AsSb)/(GaIn)As double “W”-QWH laser at temperatures between 10 $^{\circ}\text{C}$ and 100 $^{\circ}\text{C}$. All optical output pulse power values presented in this graph are single facet values. Laser emission is based on the fundamental type-II transition up to a setup-limited temperature of 100 $^{\circ}\text{C}$.

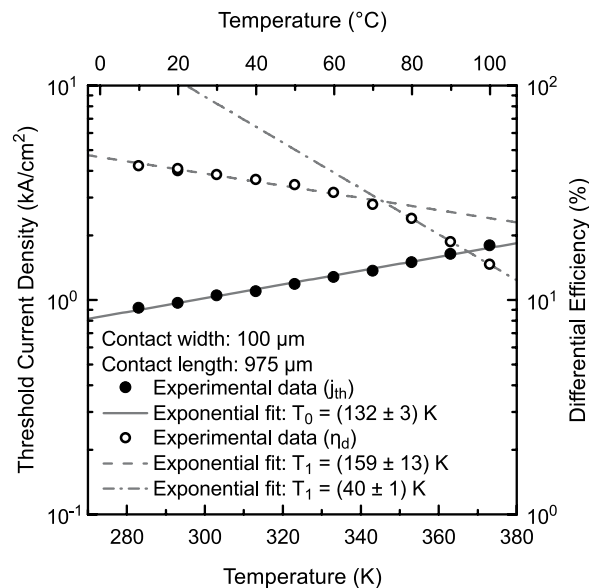


Figure 4. Temperature dependence of the threshold current density and differential efficiency of the 975 μm long (GaIn)As/Ga(AsSb)/(GaIn)As double “W”-QWH laser. Exponential fits yield characteristic temperatures of $T_0 = (132 \pm 3) \text{ K}$ over the whole temperature range and $T_1 = (159 \pm 13) \text{ K}$ between 10 $^{\circ}\text{C}$ and 70 $^{\circ}\text{C}$ and $T_1 = (40 \pm 1)$ between 80 $^{\circ}\text{C}$ and 100 $^{\circ}\text{C}$.

A plot of the threshold current density and the differential efficiency in combination with exponential fits reveals characteristic temperatures of $T_0 = (132 \pm 3) \text{ K}$ over the whole temperature range and $T_1 = (159 \pm 13) \text{ K}$ between 10 $^{\circ}\text{C}$ and 70 $^{\circ}\text{C}$ and $T_1 = (40 \pm 1) \text{ K}$ between 80 $^{\circ}\text{C}$ and 100 $^{\circ}\text{C}$ as shown in Fig. 4. These promising values for T_0 and T_1 up to a temperature of 70 $^{\circ}\text{C}$ once again underline the potential of type-II heterostructures. Additional experiments are underway to also quantify Auger losses in these type-II “W”-QWH lasers and to determine the origin of the decrease of T_1 above 70 $^{\circ}\text{C}$. A comparison with literature values of InP-based materials systems is difficult since the actual device design as well as facet coatings have an influence on the characteristic temperatures³. Typical T_0 values reported in the literature are $T_0 = 50 \text{ K} - 80 \text{ K}$ and $T_0 = 100 \text{ K} - 120 \text{ K}$ for (GaIn)(AsP)/InP¹ and (AlGaIn)As/InP^{2–5}, respectively, in case of ridge waveguide and buried-heterostructure lasers.

Summary and Conclusion

In conclusion, the careful optimization of (GaIn)As/Ga(AsSb)/(GaIn)As “W”-QWHs for emission at 1.3 μm using a fully microscopic theory resulted in an improvement of the material gain values by 66 % compared to previous designs. The suggested structures were fabricated using MOVPE and their characterization yielded room temperature laser operation based on the fundamental type-II transition at 1.275 μm . Furthermore, a differential efficiency of 41 %, a threshold current density of 1.0 kA/cm^2 , and a maximum optical output pulse power of 0.68 W per facet at a power supply-limited current density of 4.5 kA/cm^2 were obtained from characteristics in case of a 975 μm long laser bar at room temperature. The temperature-dependent characterization of the device yielded operation based on the fundamental type-II transition up to a temperature of 100 °C as well as characteristic temperatures of $T_0 = (132 \pm 3)$ K over the whole temperature range and $T_1 = (159 \pm 13)$ K between 10 °C and 70 °C and $T_1 = (40 \pm 1)$ K between 80 °C and 100 °C. These results indicate that the (GaIn)As/Ga(AsSb)/(GaIn)As materials system grown on GaAs substrate is a promising candidate for efficient and temperature-stable telecommunication lasers emitting at 1.3 μm . Further research should be carried out in order to improve the active region as well as the device design and the growth conditions of the active region in order to achieve a reduction of the threshold current density. The excellent threshold current densities obtained using (GaIn)(NAs)/GaAs active regions, which are considerably smaller than 1.0 kA/cm^2 ^{27,8}, should serve as a benchmark during these investigations. Additionally, the suppression of Auger losses needs to be confirmed and advanced device concepts such as VCSELs and distributed feedback lasers based on this materials system should be demonstrated and investigated.

Experimental Methods

The epitaxial growth of the sample is carried out in an AIXTRON AIX 200 GFR (Gas Foil Rotation) reactor system using H_2 as carrier gas at a reactor pressure of 50 mbar. Triethylgallium (TEGa), trimethylindium (TMIn), and trimethylaluminum (TMAI) are applied as group-III, tertiarybutylarsine (TBAs) and triethylantimony (TESb) are applied as group-V, and diethyltellurium (DETe) and tetrabromomethane (CBr_4) are applied as dopant sources, respectively. The n-GaAs (001) ($\pm 0.1^\circ$) substrates are treated with a TBAs-stabilized bake-out procedure in order to remove the native oxide layer before depositing a tellurium-doped GaAs buffer as well as the laser structure. The laser structure consists of 1.4 μm thick ($\text{Al}_{0.4}\text{Ga}_{0.6}$)As cladding layers, 0.2 μm thick GaAs separate confinement heterostructures (SCHs), and two active “W”-QWHs. Furthermore, a 20 nm thick GaAs intermediate barrier is grown in between the “W”-QWHs in order to ensure quantum mechanically separated systems. A highly carbon-doped GaAs cap is added on top of the p-(AlGa)As cladding in order to ensure small contact resistances. This layer is doped using CBr_4 as dopant sources while the p-(AlGa)As cladding is carbon-doped by employing a decreased V/III ratio. The growth of the n-GaAs buffer, the n- and p-(AlGa)As claddings, the SCHs, and the p⁺-GaAs cap is carried out at a growth temperature of 625 °C, while the growth temperature is lowered to 550 °C for the growth of the active regions as well as for the GaAs intermediate barrier. The resulting double “W”-QWH laser structure is processed as outlined in Ref.²¹ in order to obtain broad-area edge-emitting lasers with cavity lengths between 750 μm and 1990 μm .

The detailed device characterization is carried out under pulsed excitation conditions using a pulse length of 400 ns at a repetition rate of 10 kHz. Laser characteristics are measured using a large-area germanium photodetector for the detection of the single-facet output power as a function of the injection current density. EL measurements below laser threshold are performed using a custom-built setup in which the optical signal is dispersed by a grating monochromator (Jobin-Yvon THR 1000) and detected using a liquid nitrogen cooled germanium detector in combination with a lock-in amplifier (Stanford Research Systems SR510). EL measurements above laser threshold are carried out using an optical spectrum analyzer (Yokogawa AQ6370B). All EL measurements are carried out in a p-side up geometry and the temperature is adjusted using a thermoelectric heater.

References

- Phillips, A. F., Sweeney, S. J., Adams, A. R. & Thijs, P. J. A. The temperature dependence of 1.3- μm and 1.5- μm compressively strained InGaAs(P) MQW semiconductor lasers. *IEEE J. Sel. Topics Quantum Electron.* **5**, 401–412, <https://doi.org/10.1109/2944.78839> (1999).
- Zah, C. E. *et al.* High-Performance Uncooled 1.3 μm AlxGayIn1-x-yAs/InP Strained-Layer Quantum-Well Lasers for Subscriber Loop Applications. *IEEE J. Quantum Electron.* **30**, 511–523, <https://doi.org/10.1109/3.283799> (1994).
- Chen, T. R. *et al.* Low-Threshold and High-Temperature Operation of InGaAlAs-InP Lasers. *IEEE Photon. Technol. Lett.* **9**, 17–18, <https://doi.org/10.1109/68.554156> (1997).
- Higashi, T. *et al.* Observation of reduced nonradiative current in 1.3 μm AlGaInAs-InP strained MQW lasers. *IEEE Photon. Technol. Lett.* **11**, 409–411, <https://doi.org/10.1109/68.752531> (1999).
- Sweeney, S. J., Higashi, T., Adams, A. R., Uchida, T. & Fujii, T. A comparison of AlGaInAs and InGaAsP-based 1.3 μm semiconductor lasers using high pressure. *High Press. Res.* **18**, 49–55, <https://doi.org/10.1080/08957950008200947> (2000).
- Höhnsdorf, F. *et al.* Reduced threshold current densities of (GaIn)(NAs)/GaAs single quantum well lasers for emission wavelengths in the range 1.28–1.38 μm . *Electron. Lett.* **35**, 571–572, <https://doi.org/10.1049/el:19990421> (1999).
- Kawaguchi, M. *et al.* Lasing Characteristics of Low-Threshold GaInNAs Lasers Grown by Metalorganic Chemical Vapor Deposition. *Jpn. J. Appl. Phys.* **40**, 744–746, <https://doi.org/10.1143/JJAP.40.L744> (2001).
- Tansu, N., Kirsch, N. J. & Mawst, L. J. Low-threshold-current-density 1300-nm dilute-nitride quantum well lasers. *Appl. Phys. Lett.* **81**, 2523–2525, <https://doi.org/10.1063/1.1511290> (2002).
- Blum, O. & Klem, J. F. Characteristics of GaAsSb Single-Quantum-Well-Lasers Emitting Near 1.3 μm . *IEEE Photon. Technol. Lett.* **12**, 771–773, <https://doi.org/10.1109/68.853495> (2000).
- Yamada, M. *et al.* Low-Threshold Operation of 1.3- μm GaAsSb Quantum-Well Lasers Directly Grown on GaAs Substrates. *IEEE Photon. Technol. Lett.* **12**, 774–776, <https://doi.org/10.1109/68.853496> (2000).
- Quochi, F., Kilper, D. C., Cunningham, J. E., Dinu, M. & Shah, J. Continuous-Wave Operation of a 1.3- μm GaAsSb–GaAs Quantum-Well Vertical-Cavity Surface-Emitting Laser at Room Temperature. *IEEE Photon. Technol. Lett.* **13**, 921–923, <https://doi.org/10.1109/68.942647> (2001).
- Zegrya, G. G. & Andreev, A. D. Mechanism of suppression of Auger recombination processes in type-II heterostructures. *Appl. Phys. Lett.* **67**, 2681–2683, <https://doi.org/10.1063/1.114291> (1995).

13. Meyer, J. R. *et al.* Auger coefficients in type-II InAs/Ga_{1-x}In_xSb quantum wells. *Appl. Phys. Lett.* **73**, 2857–2859, <https://doi.org/10.1063/1.122609> (1998).
14. Peter, M. *et al.* Realization and modeling of a pseudomorphic (GaAs_{1-x}Sb_x-In_yGa_{1-y}As)/GaAs bilayer-quantum well. *Appl. Phys. Lett.* **67**, 2639–2641, <https://doi.org/10.1063/1.114321> (1995).
15. Klem, J. F., Blum, O., Kurtz, S. R., Fritz, I. J. & Choquette, K. D. GaAsSb/InGaAs type-II quantum wells for long-wavelength lasers on GaAs substrates. *J. Vac. Sci. Technol., B* **18**, 1605–1608, <https://doi.org/10.1116/1.591437> (2000).
16. Ryu, S. W. & Dapkus, P. D. Room temperature operation of type-II GaAsSb/InGaAs quantum well laser on GaAs substrates. *Electron. Lett.* **38**, 564–565, <https://doi.org/10.1049/el:20020410> (2002).
17. Berger, C. *et al.* Novel type-II material system for laser applications in the near-infrared regime. *AIP Adv.* **5**, 047105, <https://doi.org/10.1063/1.4917180> (2015).
18. Gies, S. *et al.* Excitonic transitions in highly efficient (GaIn)As/Ga(AsSb) type-II quantum-well structures. *Appl. Phys. Lett.* **107**, 182104, <https://doi.org/10.1063/1.4935212> (2015).
19. Möller, C. *et al.* Type-II VECSEL with Watt Level Output Powers at 1.2 μm. *Appl. Phys. Lett.* **108**, 071102, <https://doi.org/10.1063/1.4942103> (2016).
20. Möller, C. *et al.* Fundamental transverse mode operation of a type-II vertical-external-cavity surface emitting laser at 1.2 μm. *Electron. Lett.* **53**, 93–94, <https://doi.org/10.1049/el.2016.3732> (2017).
21. Fuchs, C. *et al.* Electrical injection type-II (GaIn)As/Ga(AsSb)/(GaIn)As single “W”-quantum well laser at 1.2 μm. *Electron. Lett.* **52**, 1875–1877, <https://doi.org/10.1049/el.2016.2851> (2016).
22. Fuchs, C., Beyer, A., Volz, K. & Stolz, W. MOVPE growth of (GaIn)As/Ga(AsSb)/(GaIn)As type-II heterostructures on GaAs substrate for near infrared laser applications. *J. Cryst. Growth* **464**, 201–205, <https://doi.org/10.1016/j.jcrysgro.2016.10.052> (2017).
23. Hader, J., Moloney, J. V., Koch, S. W. & Chow, W. W. Microscopic Modeling of Gain and Luminescence in Semiconductors. *IEEE J. Sel. Topics Quantum Electron.* **9**, 688–697, <https://doi.org/10.1109/JSTQE.2003.818342> (2003).
24. Hader, J., Moloney, J. V., Koch, S. W., Vurgaftman, I. & Meyer, J. R. Microscopic analysis of mid-infrared type-II “W” diode lasers. *Appl. Phys. Lett.* **94**, 061106, <https://doi.org/10.1063/1.3080216> (2009).
25. Chow, W. W., Blum Spahn, O., Schneider, H. C. & Klem, J. F. Contributions to the Large Blue Emission Shift in a GaAsSb Type-II Laser. *IEEE J. Quantum Electron.* **37**, 1178–1182, <https://doi.org/10.1109/3.945323> (2001).
26. Chow, W. W. & Schneider, H. C. Charge-separation effects in 1.3 μm GaAsSb type-II quantum-well laser gain. *Appl. Phys. Lett.* **78**, 4100–4102, <https://doi.org/10.1063/1.1379784> (2001).

Acknowledgements

The authors gratefully acknowledge the funding provided by Deutsche Forschungsgemeinschaft (DFG) in the framework of Sonderforschungsbereich 1083 - Structure and Dynamics of Internal Interfaces, U.S. Air Force Office of Scientific Research in the framework of STTR Phase II, grant # FA9550-16-C-0021, and U.S. Air Force Office of Scientific Research in the framework of contract # FA9550-14-1-0062.

Author Contributions

C.F. conceived the experiments and carried out the epitaxial growth of the laser structures. S.R. fabricated broad-area edge-emitting lasers. C.F. and A.Br. carried out the experimental device analysis. C.M. supported the spectroscopic experiments. C.F. evaluated the experimental data and wrote the manuscript. W.S. supervised the experimental work. A.B., M.J.W., and C.B. carried out the theoretical studies. A.B. carried out the design analysis presented in this study. S.W.K., J.H., and J.V.M. supervised the theoretical work. W.S., S.W.K., J.H., and J.V.M. secured the funding to support this study. All authors reviewed the manuscript.

Additional Information

Competing Interests: The authors declare that they have no competing interests.

Publisher's note: Springer Nature remains neutral with regard to jurisdictional claims in published maps and institutional affiliations.



Open Access This article is licensed under a Creative Commons Attribution 4.0 International License, which permits use, sharing, adaptation, distribution and reproduction in any medium or format, as long as you give appropriate credit to the original author(s) and the source, provide a link to the Creative Commons license, and indicate if changes were made. The images or other third party material in this article are included in the article's Creative Commons license, unless indicated otherwise in a credit line to the material. If material is not included in the article's Creative Commons license and your intended use is not permitted by statutory regulation or exceeds the permitted use, you will need to obtain permission directly from the copyright holder. To view a copy of this license, visit <http://creativecommons.org/licenses/by/4.0/>.

© The Author(s) 2018

6.5 Further publications

The previous sections summarize scientific publications to which Christian Fuchs made substantial contributions. Therefore, these contributions were chosen to be a part of the present thesis. Christian Fuchs contributed to additional publications by growing samples, evaluating structural properties of samples using HR-XRD and contributing the respective excerpts to publications for other projects which investigate the temporal dynamics, spectroscopic, theoretical or microscopic properties of type-II heterostructures and lasers. While these publications are not meant to be a part of this thesis due to their particular thematic focus, the following list summarizes these contributions for the sake of completeness.

- C Berger, C Möller, P Hens, C Fuchs, W Stolz, S W Koch, A Ruiz Perez, J Hader, and J V Moloney. Novel type-II material system for laser applications in the near-infrared regime. *AIP Adv.*, 5(4):047105, 2015. doi: 10.1063/1.4917180⁹⁶
- S Gies, C Kruska, C Berger, P Hens, C Fuchs, A Ruiz Perez, N W Rosemann, J Veletas, S Chatterjee, W Stolz, S W Koch, J Hader, J V Moloney, and W Heimbrodt. Excitonic transitions in highly efficient (GaIn)As/Ga(AsSb) type-II quantum-well structures. *Appl. Phys. Lett.*, 107(18):182104, 2015. doi: 10.1063/1.4935212¹⁰⁶
- P Springer, S Gies, P Hens, C Fuchs, H Han, J Hader, J V Moloney, W Stolz, K Volz, S W Koch, and W Heimbrodt. Charge transfer luminescence in (GaIn)As/GaAs/Ga(NAs) double quantum wells. *J. Lumin.*, 175:255 – 259, 2016. doi: 10.1016/j.jlumin.2016.03.010¹²¹
- C Möller, C Berger, C Fuchs, A Ruiz Perez, S W Koch, J Hader, J V Moloney, and W Stolz. 1.2 μm emitting VECSEL based on type-II aligned QWs. *Proc. SPIE*, 9734: 97340H, 2016. doi: 10.1117/12.2212438¹²²
- C Lammers, M Stein, C Berger, C Möller, C Fuchs, A Ruiz Perez, A Rahimi-Iman, J Hader, J V Moloney, W Stolz, S W Koch, and M Koch. Gain spectroscopy of a type-II VECSEL chip. *Appl. Phys. Lett.*, 109(23):232107, 2016. doi: 10.1063/1.4971333¹²³
- S Gies, M J Weseloh, C Fuchs, W Stolz, J Hader, J V Moloney, S W Koch, and W Heimbrodt. Band offset in (Ga, In)As/Ga(As, Sb) heterostructures. *J. Appl. Phys.*, 120(20):204303, 2016. doi: 10.1063/1.4968541¹²⁴
- S Gies, B Holz, C Fuchs, W Stolz, and W Heimbrodt. Recombination dynamics of type-II excitons in (Ga,In)As/GaAs/Ga(As,Sb) heterostructures. *Nanotechnology*, 28(2):025701, 2017. doi: 10.1088/0957-4484/28/2/025701¹²⁵
- C Möller, F Zhang, C Fuchs, C Berger, A Rehn, A Ruiz Perez, A Rahimi-Iman, J Hader, M Koch, J V Moloney, S W Koch, and W Stolz. Fundamental transverse

mode operation of a type-II vertical-external-cavity surface emitting laser at 1.2 μm . *Electron. Lett.*, 53(2):93 – 94, 2017. doi: 10.1049/el.2016.3732¹²⁶

- P Kükelhan, A Beyer, C Fuchs, M J Weseloh, S W Koch, W Stolz, and K Volz. Atomic structure of “W”-type quantum well heterostructures investigated by aberration-corrected STEM. *J. Microsc.*, 268(3):259 – 268, 2017. doi: 10.1111/jmi.12647¹²⁷

6.6 Talks and posters

The following list summarizes talks and posters presented by Christian Fuchs at national and international conferences and workshops. Talks and posters to which Christian Fuchs contributed as co-author are neglected here.

- C Fuchs, C Berger, C Möller, M J Weseloh, S Reinhard, A Ruiz Perez, J Hader, J V Moloney, S W Koch and W Stolz. MOVPE growth and characterization of (GaIn)As/Ga(AsSb)/(GaIn)As “W”-quantum well heterostructures on GaAs substrate. *International Conference on Internal Interfaces (ICII)*, 2016, contributed poster.
- C Fuchs, C Möller, C Berger, M J Weseloh, J Hader, J V Moloney, S W Koch and W Stolz. MOVPE growth of (GaIn)As/Ga(AsSb)/(GaIn)As-based type-II heterostructures on GaAs substrate for near infrared laser applications. *International Conference on Metal Organic Vapor Phase Epitaxy (ICMOVPE)*, 2016, contributed talk.
- C Fuchs, A Brüggemann, C Berger, M J Weseloh, C Möller, S Reinhard, J Hader, J V Moloney, A Bäumner, S W Koch and W Stolz. Temperature-dependent properties and optimization of type-II (GaIn)As/Ga(AsSb)/(GaIn)As “W”-quantum well lasers at 1.2 μm . *Compound Semiconductor Week (CSW)*, 2017, contributed talk.
- C Fuchs, A Brüggemann, P Kükelhan, C Berger, M J Weseloh, C Möller, J Hader, J V Moloney, A Beyer, K Volz, A Bäumner, S W Koch and W Stolz. Structural optimization of type-II (GaIn)As/Ga(AsSb)/(GaIn)As “W”-quantum well heterostructures for NIR laser applications. *European Workshop on Metal Organic Vapor Phase Epitaxy (EWMOVPE)*, 2017, contributed poster.

Bibliography

- [1] E Murphy. The semiconductor laser: Enabling optical communication. *Nat. Photon.*, 4(5):287, 2010.
- [2] A F Phillips, S J Sweeney, A R Adams, and P J A Thijs. The temperature dependence of 1.3- and 1.5- μm compressively strained InGaAs(P) MQW semiconductor lasers. *IEEE J. Sel. Topics Quantum Electron.*, 5(3):401 – 412, 1999. doi: 10.1109/2944.788398.
- [3] C E Zah, R Bhat, B N Pathak, F Favire, W Lin, M C Wang, N C Andreadakis, D M Hwang, M A Koza, T P Lee, Z Wang, D Darby, D Flanders, and J J Hsieh. High-Performance Uncooled 1.3 μm $\text{Al}_x\text{Ga}_y\text{In}_{1-x-y}\text{As}/\text{InP}$ Strained-Layer Quantum-Well Lasers for Subscriber Loop Applications. *IEEE J. Quantum Electron.*, 30(2): 511 – 523, 1994. doi: 10.1109/3.283799.
- [4] T R Chen, P C Chen, J Ungar, M A Newkirk, S Oh, and N Bar-Chaim. Low-Threshold and High-Temperature Operation of InGaAlAs-InP Lasers. *IEEE Photon. Technol. Lett.*, 9(1):17 – 18, 1997. doi: 10.1109/68.554156.
- [5] T Higashi, S J Sweeney, A F Phillips, A R Adams, E P O'Reilly, T Uchida, and T Fujii. Observation of reduced nonradiative current in 1.3 μm AlGaInAs-InP strained MQW lasers. *IEEE Photon. Technol. Lett.*, 11(4):409 – 411, 1999. doi: 10.1109/68.752531.
- [6] T Higashi, S J Sweeney, A F Phillips, A R Adams, E P O'Reilly, T Uchida, and T Fujii. Experimental Analysis of Temperature Dependence in 1.3- μm AlGaInAs-InP Strained MQW Lasers. *IEEE J. Sel. Topics Quantum Electron.*, 5(3):413 – 419, 1999. doi: 10.1109/2944.788399.
- [7] S J Sweeney, T Higashi, A R Adams, T Uchida, and T Fujii. A comparison of AlGaInAs and InGaAsP-based 1.3 μm semiconductor lasers using high pressure. *High Press. Res.*, 18(1-6):49 – 55, 2000. doi: 10.1080/08957950008200947.
- [8] S Seki, H Oohashi, H Sugiura, T Hirono, and K Yokoyama. Study on the dominant mechanisms for the temperature sensitivity of threshold current in 1.3- μm InP-based

- strained-layer quantum-well lasers. *IEEE J. Quantum Electron.*, 32(8):1478 – 1486, 1996. doi: 10.1109/3.511561.
- [9] Y P Varshni. Temperature dependence of the energy gap in semiconductors. *Physica*, 34(1):149 – 154, 1967. doi: 10.1016/0031-8914(67)90062-6.
- [10] G G Zegrya and A D Andreev. Mechanism of suppression of Auger recombination processes in type-II heterostructures. *Appl. Phys. Lett.*, 67(18):2681 – 2683, 1995. doi: 10.1063/1.114291.
- [11] J R Meyer, C L Felix, W W Bewley, I Vurgaftman, E H Aifer, L J Olafsen, J R Lindle, C A Hoffman, M J Yang, B R Bennett, B V Shanabrook, H Lee, C H Lin, S S Pei, and R H Miles. Auger coefficients in type-II InAs/Ga_{1-x}In_xSb quantum wells. *Appl. Phys. Lett.*, 73(20):2857 – 2859, 1998. doi: 10.1063/1.122609.
- [12] M Ohkubo, T Ijichi, A Iketani, and T Kikuta. 980-nm Aluminum-Free InGaAs/InGaAsP/InGaP GRIN-SCH SL-QW Lasers. *IEEE J. Quantum Electron.*, 30(2):408 – 414, 1994. doi: 10.1109/3.283788.
- [13] H Asonen, A Ovtchinnikov, G Zhang, J Näppi, P Savolainen, and M Pessa. Aluminum-Free 980-nm GaInAs/GaInAsP/GaInP Pump Lasers. *IEEE J. Quantum Electron.*, 30(2):415 – 423, 1994. doi: 10.1109/3.283789.
- [14] N Chand, S N G Chu, N K Dutta, J Lopata, M Geva, A V Syrbu, A Z Mereutza, and V P Yakovlev. Growth and Fabrication of High-Performance 980-nm Strained InGaAs Quantum-Well Lasers for Erbium-Doped Fiber Amplifiers. *IEEE J. Quantum Electron.*, 30(2):424 – 440, 1994. doi: 10.1109/3.283790.
- [15] L J Mawst, A Bhattacharya, J Lopez, D Botez, D Z Garbuzov, L DeMarco, J C Connolly, M Jansen, F Fang, and R F Nabiev. 8 W continuous wave front-facet power from broad-waveguide Al-free 980 nm diode lasers. *Appl. Phys. Lett.*, 69(11):1532 – 1534, 1996. doi: 10.1063/1.117995.
- [16] M Peter, K Winkler, M Maier, N Herres, J Wagner, D Fekete, K H Bachem, and D Richards. Realization and modeling of a pseudomorphic (GaAs_{1-x}Sb_x-In_yGa_{1-y}As)/GaAs bilayer-quantum well. *Appl. Phys. Lett.*, 67(18):2639 – 2641, 1995. doi: 10.1063/1.114321.
- [17] S R Johnson, S Chapparo, J Wang, N Samal, Y Cao, Z B Chen, C Navarro, J Xu, S Q Yu, D J Smith, C Z Guo, P Dowd, W Braun, and Y H Zhang. GaAs-substrate-based long-wave active materials with type-II band alignments. *J. Vac. Sci. Technol. B*, 19(4):1501 – 1504, 2001. doi: 10.1116/1.1386380.

- [18] B N Zvonkov, S M Nekorkin, O V Vikhrova, and N V Dikareva. Emission properties of heterostructures with a (GaAsSb-InGaAs)/GaAs bilayer quantum well. *Semiconductors*, 47(9):1219 – 1223, 2013. doi: 10.1134/S1063782613090261.
- [19] N V Dikareva, O V Vikhrova, B N Zvonkov, N V Malekhonova, S M Nekorkin, A V Pirogov, and D A Pavlov. Effect of thermal annealing on the emission properties of heterostructures containing a quantum-confined GaAsSb layer. *Semiconductors*, 49(1):9 – 12, 2015. doi: 10.1134/S1063782615010054.
- [20] W W Chow and H C Schneider. Charge-separation effects in 1.3 μm GaAsSb type-II quantum-well laser gain. *Appl. Phys. Lett.*, 78(26):4100 – 4102, 2001. doi: 10.1063/1.1379784.
- [21] W W Chow, O Blum Spahn, H C Schneider, and J F Klem. Contributions to the Large Blue Emission Shift in a GaAsSb Type-II Laser. *IEEE J. Quantum Electron.*, 37(9):1178 – 1182, 2001. doi: 10.1109/3.945323.
- [22] M Kudo, K Ouchi, J Kasai, and T Mishima. Low-Lattice-Strain Long-Wavelength GaAsSb/GaInAs Type-II Quantum Wells Grown on GaAs Substrates. *Jpn. J. Appl. Phys.*, 41(10A):1040 – 1042, 2002. doi: 10.1143/JJAP.41.L1040.
- [23] C Schlichenmaier, S W Koch, and W W Chow. Linewidth enhancement factor in 1.3 μm GaAsSb type-II quantum-well lasers. *Appl. Phys. Lett.*, 81(16):2944 – 2946, 2002. doi: 10.1063/1.1514392.
- [24] S H Park and I D Hwang. Effect of an InGaAs Layer in 1.3- μm GaAsSb/GaInAs Type-II Trilayer Quantum-Well Lasers on GaAs Substrates. *J. Korean Phys. Soc.*, 45(2):348 – 351, 2004.
- [25] S H Park. Electronic and Optical Properties of Type-II GaAsSb/GaInAs/GaAs Trilayer Quantum-Well Lasers. *J. Korean Phys. Soc.*, 46(4):835 – 839, 2005.
- [26] S H Park, H M Kim, and J J Kim. Threshold Current Density of 1.3- μm GaAsSb/GaInAs/GaAs Type-II Trilayer Quantum Well Lasers on GaAs Substrates. *J. Korean Phys. Soc.*, 50(4):1018 – 1021, 2007.
- [27] J F Klem, O Blum, S R Kurtz, I J Fritz, and K D Choquette. GaAsSb/InGaAs type-II quantum wells for long-wavelength lasers on GaAs substrates. *J. Vac. Sci. Technol. B*, 18(3):1605 – 1608, 2000. doi: 10.1116/1.591437.
- [28] S W Ryu and P D Dapkus. Room temperature operation of type-II GaAsSb/InGaAs quantum well laser on GaAs substrates. *Electron. Lett.*, 38(12):564 – 565, 2002. doi: 10.1049/el:20020410.

- [29] J R Meyer, C A Hoffmann, F J Bartoli, and L R Ram-Mohan. Type-II quantum-well lasers for the mid-wavelength infrared. *Appl. Phys. Lett.*, 67(6):757 – 759, 1995. doi: 10.1063/1.115216.
- [30] J I Malin, J R Meyer, C L Felix, J R Lindle, L Goldberg, C A Hoffmann, F J Bartoli, C H Lin, P C Chang, S J Murry, R Q Yang, and S S Pei. Type II mid-infrared quantum well lasers. *Appl. Phys. Lett.*, 68(21):2976 – 2978, 1996. doi: 10.1063/1.116374.
- [31] J R Meyer, L J Olafsen, E H Aifer, W W Bewley, C L Felix, I Vurgaftman, M J Yang, L Goldberg, D Zhang, C H Lin, S S Pei, and D H Chow. Type II W, interband cascade and vertical-cavity surface-emitting mid-IR lasers. *IEEE Proc. Optoelectron.*, 145(5):275 – 280, 1998. doi: 10.1049/ip-opt:19982304.
- [32] I Vurgaftman, C L Felix, W W Bewley, D W Stokes, R E Bartolo, and J R Meyer. Mid-infrared “W” lasers. *Phil. Trans. R. Soc. Lond. A*, 359(1780):489 – 503, 2001. doi: 10.1098/rsta.2000.0738.
- [33] C L Canedy, W W Bewley, J R Lindle, C S Kim, M Kim, I Vurgaftman, and J R Meyer. Investigation of Mid-Infrared Type-II “W” Diode Lasers. *J. Electron. Mater.*, 35(3):453 – 461, 2006. doi: 10.1007/BF02690532.
- [34] J Hader, J V Moloney, S W Koch, I Vurgaftman, and J R Meyer. Microscopic analysis of mid-infrared type-II “W” diode lasers. *Appl. Phys. Lett.*, 94(6):061106, 2009. doi: 10.1063/1.3080216.
- [35] R Sidhu, N Duan, J C Campbell, and A L Holmes. A Long-Wavelength Photodiode on InP Using Lattice-Matched GaInAs-GaAsSb Type-II Quantum Wells. *IEEE Photon. Technol. Lett.*, 17(12):2715 – 2717, 2005. doi: 10.1109/LPT.2005.859163.
- [36] U Seidel, B E Săgöl, N Szabó, K Schwarzburg, and T Hannappel. InGaAs/GaAsSb-interface studies in a tunnel junction of a low band gap tandem solar cell. *Thin Solid Films*, 516(20):6723 – 6728, 2008. doi: 10.1016/j.tsf.2007.12.013.
- [37] J Y T Huang, L J Mawst, T F Kuech, X Song, S E Babcock, C S Kim, I Vurgaftman, J R Meyer, and A L Holmes Jr. Design and characterization of strained InGaAs/GaAsSb type-II “W” quantum wells on InP substrates for mid-IR emission. *J. Phys. D: Appl. Phys.*, 42(2):025108, 2009. doi: 10.1088/0022-3727/42/2/025108.
- [38] C Grasse, P Wiecha, T Gruendl, S Sprengel, R Meyer, and M C Amann. InP-based 2.8-3.5 μ m resonant-cavity light emitting diodes based on type-II transitions in GaInAs/GaAsSb heterostructures. *Appl. Phys. Lett.*, 101(22):221107, 2012. doi: 10.1063/1.4768447.

- [39] C Grasse, T Gruendl, S Sprengel, P Wiecha, K Vizbaras, R Meyer, and M C Amann. GaInAs/GaAsSb-based type-II micro-cavity LED with 2-3 μm light emission grown on InP substrate. *J. Cryst. Growth*, 370:240 – 243, 2013. doi: 10.1016/j.jcrysgro.2012.07.001.
- [40] N Yadav, G Bhardwaj, S G Anjum, S Dalela, M J Siddiqui, and P A Alvi. Investigation of high optical gain in complex type-II InGaAs/InAs/GaAsSb nano-scale heterostructure for MIR applications. *Appl. Optics*, 56(15):4243, 2017. doi: 10.1364/AO.56.004243.
- [41] S Sprengel, C Grasse, P Wiecha, A Andrejew, T Gruendl, G Boehm, R Meyer, and M C Amann. InP-Based Type-II Quantum-Well Lasers and LEDs. *IEEE J. Sel. Topics Quantum Electron.*, 19(4):1900909, 2013. doi: 10.1109/JSTQE.2013.2247572.
- [42] S Sprengel, A Andrejew, F Federer, G K Veerabathran, G Boehm, and M C Amann. Continuous wave vertical cavity surface emitting lasers at 2.5 μm with InP-based type-II quantum wells. *Appl. Phys. Lett.*, 106(15):151102, 2015. doi: 10.1063/1.4917282.
- [43] S Sprengel, G K Veerabathran, F Federer, A Andrejew, and M C Amann. InP-Based Vertical-Cavity Surface-Emitting Lasers With Type-II Quantum Wells. *IEEE J. Sel. Topics Quantum Electron.*, 21(6):453 – 461, 2015. doi: 10.1109/JSTQE.2015.2424834.
- [44] C H Chang, Z L Li, L Hong-Ting, C H Pan, C P Lee, G Lin, and S D Lin. Low-Threshold Short-Wavelength Infrared InGaAs/GaAsSb “W”-Type QW Laser on InP Substrate. *IEEE Photon. Technol. Lett.*, 27(3):225 – 228, 2015. doi: 10.1109/LPT.2014.2362151.
- [45] L A Coldren, S W Corzine, and M L Mašanović. *Diode Lasers and Photonic Integrated Circuits*. John Wiley & Sons, 2nd edition, 2012.
- [46] S Adachi. *GaAs and Related Materials: Bulk Semiconducting and Superlattice Properties*. World Scientific, 1st edition, 1994. doi: 10.1142/2508.
- [47] S J Sweeney and S R Jin. Bismide-nitride alloys: Promising for efficient light emitting devices in the near- and mid-infrared. *J. Appl. Phys.*, 113(4):043110, 2013. doi: 10.1063/1.4789624.
- [48] I Vurgaftman, J R Meyer, and L R Ram-Mohan. Band parameters for III-V compound semiconductors and their alloys. *J. Appl. Phys.*, 89(11):5816 – 5875, 2001. doi: 10.1063/1.1368156.
- [49] T H Maiman. Stimulated Optical Radiation in Ruby. *Nature*, 187(4736):493 – 494, 1960. doi: 10.1038/187493a0.

- [50] J J Coleman. The development of the semiconductor laser diode after the first demonstration in 1962. *Semicond. Sci. Technol.*, 27(9):090207, 2012. doi: 10.1088/0268-1242/27/9/090207.
- [51] S Adachi. *Properties of Aluminium Gallium Arsenide*. Inspec, 1st edition, 1993.
- [52] W T Tsang. Extremely low threshold (AlGa)As graded-index waveguide separate-confinement heterostructure lasers grown by molecular beam epitaxy. *Appl. Phys. Lett.*, 40(217):217 – 219, 1982. doi: 10.1063/1.93046.
- [53] S Hersee, M Baldy, P Assenat, B De Cremoux, and J P Duchemin. Low-threshold GRIN-SCH GaAs/GaAlAs laser structure grown by OM VPE. *Electron. Lett.*, 18(14):618 – 620, 1982. doi: 10.1049/el:19820423.
- [54] R D Burnham, W Streifer, D R Scifres, C Lindström, and T L Paoli. Low-threshold single quantum Well (60 Å) GaAlAs lasers grown by MO-CVD with Mg as p-type dopant. *Electron. Lett.*, 18(25):1095 – 1097, 1982. doi: 10.1049/el:19820748.
- [55] R Chin, N Holonyak Jr, B A Vojak, K Hess, R D Dupuis, and P D Dapkus. Temperature dependence of threshold current for quantum-well $\text{Al}_x\text{Ga}_{1-x}\text{As}$ -GaAs heterostructure laser diodes. *Appl. Phys. Lett.*, 36(1):19 – 21, 1980. doi: 10.1063/1.91290.
- [56] H Iwamura, T Saku, T Ishibashi, K Otsuka, and Y Horikoshi. Dynamic behaviour of a GaAs-AlGaAs MQW laser diode. *Electron. Lett.*, 19(5):180 – 181, 1983. doi: 10.1049/el:19830125.
- [57] B Heinen, T L Wang, M Sparenberg, A Weber, B Kunert, J Hader, S W Koch, J V Moloney, M Koch, and W Stolz. 106 W continuous-wave output power from vertical-external-cavity surface-emitting laser. *Electron. Lett.*, 48(9):516 – 517, 2012. doi: 10.1049/el.2012.0531.
- [58] J Hader, G Hardesty, T L Wang, M J Yarborough, Y Kaneda, J V Moloney, B Kunert, W Stolz, and S W Koch. Predictive Microscopic Modeling of VECSELs. *IEEE J. Quantum Electron.*, 46(5):810 – 817, 2010. doi: 10.1109/JQE.2009.2035714.
- [59] A R Zakharian, J Hader, J V Moloney, S W Koch, P Brick, and S Lutgen. Experimental and theoretical analysis of optically pumped semiconductor disk lasers. *Appl. Phys. Lett.*, 83(7):1313 – 1315, 2003. doi: 10.1063/1.1601672.
- [60] A C Tropper and S Hoogland. Extended cavity surface-emitting semiconductor lasers. *Prog. Quant. Electron.*, 30(1):1 – 43, 2006. doi: 10.1016/j.pquantelec.2005.10.002.
- [61] C Möller. *Fundamental analysis and optimization of barrier-pumped GaAs-based VECSELs*. PhD thesis, Philipps-Universität Marburg, 2016.

- [62] T R Chen, B Chang, L C Chiu, K L Yu, S Margalit, and A Yariv. Carrier leakage and temperature dependence of InGaAsP lasers. *Appl. Phys. Lett.*, 43(3):217 – 218, 1983. doi: 10.1063/1.94305.
- [63] W Shockley and W T Read Jr. Statistics of the Recombinations of Holes and Electrons. *Phys. Rev.*, 57(5):835 – 842, 1952. doi: 10.1103/PhysRev.87.835.
- [64] R N Hall. Electron-Hole Recombination in Germanium. *Phys. Rev.*, 87(2):387, 1952. doi: 10.1103/PhysRev.87.387.
- [65] Y K Hsieh and H C Card. Limitation to Shockley-Read-Hall model due to direct photoionization of the defect states. *J. Appl. Phys.*, 65(6):2409 – 2415, 1989. doi: 10.1063/1.342810.
- [66] G Beaucarne and M A Green. A modified Shockley-Read-Hall theory including radiative transitions. *Solid State Electron.*, 47(4):685 – 689, 2003. doi: 10.1016/S0038-1101(02)00316-7.
- [67] R Fehse, S Jin, S J Sweeney, A R Adams, E P O'Reilly, H Riechert, S Illek, and A Y Egorov. Evidence for large monomolecular recombination contribution to threshold current in 1.3 μm GaInNAs semiconductor lasers. *Electron. Lett.*, 37(25):1518 – 1520, 2001. doi: 10.1049/el:20011033.
- [68] A Haug. Free-carrier absorption in semiconductor lasers. *Semicond. Sci. Technol.*, 7(3):373 – 378, 1992. doi: 10.1088/0268-1242/7/3/017.
- [69] A R Adams, M Asada, Y Suematsu, and S Arai. The Temperature Dependence of the Efficiency and Threshold Current of $\text{In}_{1-x}\text{Ga}_x\text{As}_y\text{P}_{1-y}$ Lasers Related to Intervalence Band Absorption. *Jpn. J. Appl. Phys.*, 19(10):621 – 624, 1980. doi: 10.1143/JJAP.19.L621.
- [70] A R Adams, K C Heasman, and J Hilton. A reassessment of intervalence band absorption in 1.6 μm (GaIn)(AsP)/InP. *Semicond. Sci. Technol.*, 2(12):761 – 764, 1987. doi: 10.1088/0268-1242/2/12/001.
- [71] G N Childs, S Brand, and R A Abram. Intervalence band absorption in semiconductor laser materials. *Semicond. Sci. Technol.*, 1(2):116 – 120, 1986. doi: 10.1088/0268-1242/1/2/004.
- [72] E P O'Reilly. Valence band engineering in strained-layer structures. *Semicond. Sci. Technol.*, 4(3):121 – 137, 1989. doi: 10.1088/0268-1242/4/3/001.
- [73] A Haug. Phonon-assisted intervalence band absorption in semiconductor lasers. *Semicond. Sci. Technol.*, 5(6):557 – 560, 1990. doi: 10.1088/0268-1242/5/6/016.

- [74] B A Ikoy. Electron-Hole and Photon Recombination Processes in Quantum Well Semiconductor Lasers. *Am. J. Opt. Photon.*, 3(5):80 – 84, 2015. doi: 10.11648/j.ajop.20150305.14.
- [75] A R Beattie and P T Landsberg. Auger Effect in Semiconductors. *P. Roy. Soc. Lond. A Mat.*, 249(1256):16 – 29, 1959. doi: 10.1098/rspa.1959.0003.
- [76] A R Beattie and G Smith. Recombination in Semiconductors by a Light Hole Auger Transition. *Phys. Status Solidi B*, 12(2):577 – 586, 1967. doi: 10.1002/pssb.19670190209.
- [77] N K Dutta and R J Nelson. Temperature dependence of threshold of InGaAsP/InP double-heterostructure lasers and Auger recombination. *Appl. Phys. Lett.*, 38(6):407 – 409, 1981. doi: 10.1063/1.92380.
- [78] A Haug. Auger recombination in direct-gap semiconductors: band-structure effects. *J. Phys. C: Solid State Phys.*, 16(21):4159 – 4172, 1983. doi: 10.1088/0022-3719/16/21/017.
- [79] A D Andreev and G G Zegrya. Auger recombination in strained quantum wells. *Semiconductors*, 31(3):297 – 303, 1997. doi: 10.1134/1.1187132.
- [80] S Hausser, G Fuchs, A Hangleiter, K Streubel, and W T Tsang. Auger recombination in bulk and quantum well InGaAs. *Appl. Phys. Lett.*, 56(10):913 – 915, 1990. doi: 10.1063/1.103175.
- [81] G Fuchs, C Schiedel, A Hangleiter, V Härle, and F Scholz. Auger recombination in strained and unstrained InGaAs/InGaAsP multiple quantum-well lasers. *Appl. Phys. Lett.*, 62(4):396 – 398, 1993. doi: 10.1063/1.108941.
- [82] Y Zou, J S Osinski, P Grodzinski, P D Dapkus, W Rideout, W F Sharfin, and F D Crawford. Effect of Auger recombination and differential gain on the temperature sensitivity of 1.5 μm quantum well lasers. *Appl. Phys. Lett.*, 62(2):175 – 177, 1993. doi: 10.1063/1.109362.
- [83] C A Broderick, M Usman, S J Sweeney, and E P O'Reilly. Band engineering in dilute nitride and bismide semiconductor lasers. *Semicond. Sci. Technol.*, 27(9): 094011, 2012. doi: 10.1088/0268-1242/27/9/094011.
- [84] G G Zegrya and A S Polkovnikov. Mechanisms of Auger recombination in quantum wells. *J. Exp. Theor. Phys.*, 86(4):815 – 832, 1998. doi: 10.1134/1.558544.
- [85] K Hantke, J D Heber, C Schlichenmaier, A Thränhardt, T Meier, B Kunert, K Volz, W Stolz, S W Koch, and W W Rühle. Time-resolved photoluminescence of type-I and type-II (GaIn)As/Ga(NAs) heterostructures. *Phys. Rev. B*, 71(16):165320, 2005. doi: 10.1103/PhysRevB.71.165320.

- [86] H Kroemer. The 6.1 Å family (InAs, GaSb, AlSb) and its heterostructures: a selective review. *Physica E*, 20(3):196 – 203, 2004. doi: 10.1016/j.physe.2003.08.003.
- [87] O J Pitts, S P Watkins, C X Wang, V Fink, and K L Kavanagh. Antimony segregation in GaAs-based multiple quantum well structures. *J. Cryst. Growth*, 254: 28 – 34, 2003. doi: 10.1016/S0022-0248(03)01164-3.
- [88] B E Hawkins, A A Khandekar, J Y Yeh, L J Mawst, and T F Kuech. Effects of Gas switching sequences on GaAs/GaAs_{1-y}Sb_y superlattices. *J. Cryst. Growth*, 272:686 – 693, 2004. doi: 10.1016/j.jcrysgro.2004.08.045.
- [89] M Pristovsek, M Zorn, U Zeimer, and M Weyers. Growth of strained GaAsSb layers on GaAs (001) by MOVPE. *J. Cryst. Growth*, 276:347 – 353, 2005. doi: 10.1016/j.jcrysgro.2004.11.420.
- [90] A A Khandekar, J Y Yeh, L J Mawst, X Song, S E Babcock, and T F Kuech. Effects of Ga- and Sb-precursor chemistry on the alloy composition in pseudomorphically strained GaAs_{1-y}Sb_y films grown via metalorganic vapor phase epitaxy. *J. Cryst. Growth*, 303:456 – 465, 2007. doi: 10.1016/j.jcrysgro.2006.12.034.
- [91] T F Kuech, A A Khandekar, M Rathi, L J Mawst, J Y T Huang, X Song, S E Babcock, J R Meyer, and I Vurgaftman. MOVPE growth of antimonide-containing alloy materials for long wavelength applications. *J. Cryst. Growth*, 310:4826 – 4830, 2008. doi: 10.1016/j.jcrysgro.2008.09.006.
- [92] Y K Su, C T Wan, R W Chuang, C Y Huang, W C Chen, Y S Wang, and H C Yu. Temperature effect on the growth of strained GaAs_{1-y}Sb_y/GaAs (y>0.4) quantum wells by MOVPE. *J. Cryst. Growth*, 310:4850 – 4853, 2008. doi: 10.1016/j.jcrysgro.2008.07.085.
- [93] W Braun, P Dowd, C Z Guo, S L Chen, C M Ryu, U Koelle, S R Johnson, Y H Zhang, J W Tomm, T Elsässer, and D J Smith. Strained InGaAs/GaPAsSb heterostructures grown on GaAs (001) for optoelectronic applications in the 1100-1550 nm range. *J. Appl. Phys*, 88(5):3004 – 3014, 2000. doi: 10.1063/1.1287233.
- [94] I Vurgaftman, J R Meyer, N Tansu, and L J Mawst. (In)GaAsN-based type-II “W” quantum-well lasers for emission at $\lambda = 1.55 \mu\text{m}$. *Appl. Phys. Lett.*, 83(14):2742 – 2744, 2003. doi: 10.1063/1.1616193.
- [95] J Y Yeh, L J Mawst, A A Khandekar, T F Kuech, Vurgaftman, J R Meyer, and N Tansu. Long wavelength emission of InGaAsN/GaAsSb type II “W” quantum wells. *Appl. Phys. Lett.*, 88(5):05115, 2006. doi: 10.1063/1.2171486.

- [96] C Berger, C Möller, P Hens, C Fuchs, W Stolz, S W Koch, A Ruiz Perez, J Hader, and J V Moloney. Novel type-II material system for laser applications in the near-infrared regime. *AIP Adv.*, 5(4):047105, 2015. doi: 10.1063/1.4917180.
- [97] C Fuchs, A Beyer, K Volz, and W Stolz. MOVPE growth of (GaIn)As/Ga(AsSb)/(GaIn)As type-II heterostructures on GaAs substrate for near infrared laser applications. *J. Cryst. Growth*, 464:201 – 205, 2017. doi: 10.1016/j.jcrysgro.2016.10.052.
- [98] H Mohseni, V I Litvinov, and M Razeghi. Interface-induced suppression of the Auger recombination in type-II InAs/GaSb superlattices. *Phys. Rev. B*, 58(23):15378 – 15380, 1998. doi: 10.1103/PhysRevB.58.15378.
- [99] G B Stringfellow. *Organometallic Vapor-Phase Epitaxy*. Academic Press, 2nd edition, 1998.
- [100] R D Deslattes, E G Kessler Jr, P Indelicato, L de Billy, E Lindroth, and J Anton. X-ray transition energies: new approach to a comprehensive evaluation. *Rev. Mod. Phys.*, 75(1):35 – 99, 2003. doi: 10.1103/RevModPhys.75.35.
- [101] G C Wang and T M Lu. *RHEED Transmission Mode and Pole Figures*. Springer, 1st edition, 2014. doi: 10.1007/978-1-4614-9287-0.
- [102] W Hagen. Tetragonal distortion in heteroepitaxial layers: Ge on GaAs. *J. Cryst. Growth*, 43(6):739 – 744, 1978. doi: 10.1016/0022-0248(78)90154-9.
- [103] L Tapfer and K Ploog. X-ray interference in ultrathin epitaxial layers: A versatile method for the structural analysis of single quantum wells and heterointerfaces. *Phys. Rev. B*, 40(14):9802 – 9810, 1989. doi: 10.1103/PhysRevB.40.9802.
- [104] L De Caro, C Giannini, and L Tapfer. Determination of the lattice strain and chemical composition of semiconductor heterostructures by high-resolution x-ray diffraction. *J. Appl. Phys.*, 79(8):4101 – 4110, 1996. doi: 10.1063/1.361773.
- [105] J Hader, M Scheller, A Laurain, C Baker, J V Moloney, and S W Koch. Ultrafast non-equilibrium carrier dynamics in semiconductor laser mode-locking. *Semicond. Sci. Technol.*, 32(1):013002, 2017. doi: 10.1088/0268-1242/32/1/013002.
- [106] S Gies, C Kruska, C Berger, P Hens, C Fuchs, A Ruiz Perez, N W Rosemann, J Veletas, S Chatterjee, W Stolz, S W Koch, J Hader, J V Moloney, and W Heimbrodt. Excitonic transitions in highly efficient (GaIn)As/Ga(AsSb) type-II quantum-well structures. *Appl. Phys. Lett.*, 107(18):182104, 2015. doi: 10.1063/1.4935212.
- [107] H Döscher, P Hens, A Beyer, L Tapfer, K Volz, and W Stolz. GaP-interlayer formation on epitaxial GaAs(001) surfaces in MOVPE ambient. *J. Cryst. Growth*, 464:2 – 7, 2017. doi: 10.1016/j.jcrysgro.2016.10.055.

- [108] C Möller, C Fuchs, C Berger, A Ruiz Perez, M Koch, J Hader, J V Moloney, S W Koch, and W Stolz. Type-II VECSEL with Watt Level Output Powers at 1.2 μm . *Appl. Phys. Lett.*, 108(7):071102, 2016. doi: 10.1063/1.4942103.
- [109] N Tansu and L J Mawst. Design Analysis of 1550-nm GaAsSb-(In)GaAsN Type-II Quantum-Well Laser Active Regions. *IEEE J. Quantum Electron.*, 39(10):1205 – 1210, 2003. doi: 10.1109/JQE.2003.817235.
- [110] A A Khandekar, B E Hawkins, T F Kuech, J Y Yeh, L J Mawst, J R Meyer, I Vurgaftman, and N Tansu. Characteristics of GaAsN/GaAsSb type-II quantum wells grown by metalorganic vapor phase epitaxy on GaAs substrates. *J. Appl. Phys.*, 98(12):123525, 2005. doi: 10.1063/1.2148620.
- [111] H Yang, V Lordi, and J S Haris. Photoluminescence and electroabsorption in GaNAs/GaAsSb heterojunctions. *Electron. Lett.*, 42(1):52 – 54, 2006. doi: 10.1049/el:20063572.
- [112] J Y Yeh, L J Mawst, A A Khandekar, T F Kuech, Vurgaftman, J R Meyer, and N Tansu. Characteristics of InGaAsN-GaAsSb type-II “W” quantum wells. *J. Cryst. Growth*, 287:615 – 619, 2006. doi: 10.1016/j.jcrysgro.2005.10.087.
- [113] L J Mawst, J Y T Huang, D P Xu, J Y Yeh, G Tsvd, T F Kuech, and N Tansu. MOCVD-Grown Dilute Nitride Type II Quantum Wells. *IEEE J. Sel. Topics Quantum Electron.*, 14(4):979 – 991, 2008. doi: 10.1109/JSTQE.2008.918105.
- [114] High antimony content GaAs_{1-z}N_z-GaAs_{1-y}Sb_y type-II “W” structure for long wavelength emission. *J. Appl. Phys.*, 106(6):063713, 2009. doi: 10.1063/1.3226000.
- [115] W Pan, L Zhang, L Zhu, Y Li, X Chen, X Wu, F Zhang, J Shao, and S Wang. Optical properties and band bending of InGaAs/GaAsBi/InGaAs type-II quantum well grown by gas source molecular beam epitaxy. *J. Appl. Phys.*, 120(10):105702, 2016. doi: 10.1063/1.4962288.
- [116] L Yue, Y Song, X Chen, Q Chen, W Pan, X Wu, J Liu, L Zhang, J Shao, and S Wang. Novel type II InGaAs/GaAsBi quantum well for longer wavelength emission. *J. Alloy. Compd.*, 695:753 – 759, 2017. doi: 10.1016/j.jallcom.2016.07.300.
- [117] J Hwang and J D Phillips. Band structure of strain-balanced GaAsBi/GaAsN superlattices on GaAs. *Phys. Rev. B*, 83(19):195327, 2011. doi: 10.1103/PhysRevB.83.195327.
- [118] C A Broderick, S Jin, I P Marko, K Hild, P Ludewig, Z L Bushell, W Stolz, J M Rorison, E P O’Reilly, K Volz, and S Sweeney. GaAs_{1-x}Bi_x/GaN_yAs_{1-y} type-II quantum wells: novel strainbalanced heterostructures for GaAs-based near- and mid-infrared photonics. *Sci. Rep.*, 7:46371, 2017. doi: 10.1038/srep46371.

- [119] C Fuchs, C Berger, C Möller, M Weseloh, S Reinhard, J Hader, J V Moloney, S W Koch, and W Stolz. Electrical injection type-II (GaIn)As/Ga(AsSb)/(GaIn)As single ‘W’-quantum well laser at 1.2 μm . *Electron. Lett.*, 52(22):1875 – 1877, 2016. doi: 10.1049/el.2016.2851.
- [120] C Fuchs, A Brüggemann, M J Weseloh, C Berger, C Möller, S Reinhard, J Hader, J V Moloney, A Bäumner, S W Koch, and W Stolz. High-temperature operation of electrical injection type-II (GaIn)As/Ga(AsSb)/(GaIn)As “W”-quantum well lasers emitting at 1.3 μm . *Sci. Rep.*, 8(1):1422, 2018. doi: 10.1038/s41598-018-19189-1.
- [121] P Springer, S Gies, P Hens, C Fuchs, H Han, J Hader, J V Moloney, W Stolz, K Volz, S W Koch, and W Heimbrodt. Charge transfer luminescence in (GaIn)As/GaAs/Ga(NAs) double quantum wells. *J. Lumin.*, 175:255 – 259, 2016. doi: 10.1016/j.jlumin.2016.03.010.
- [122] C Möller, C Berger, C Fuchs, A Ruiz Perez, S W Koch, J Hader, J V Moloney, and W Stolz. 1.2 μm emitting VECSEL based on type-II aligned QWs. *Proc. SPIE*, 9734: 97340H, 2016. doi: 10.1117/12.2212438.
- [123] C Lammers, M Stein, C Berger, C Möller, C Fuchs, A Ruiz Perez, A Rahimi-Iman, J Hader, J V Moloney, W Stolz, S W Koch, and M Koch. Gain spectroscopy of a type-II VECSEL chip. *Appl. Phys. Lett.*, 109(23):232107, 2016. doi: 10.1063/1.4971333.
- [124] S Gies, M J Weseloh, C Fuchs, W Stolz, J Hader, J V Moloney, S W Koch, and W Heimbrodt. Band offset in (Ga, In)As/Ga(As, Sb) heterostructures. *J. Appl. Phys.*, 120(20):204303, 2016. doi: 10.1063/1.4968541.
- [125] S Gies, B Holz, C Fuchs, W Stolz, and W Heimbrodt. Recombination dynamics of type-II excitons in (Ga,In)As/GaAs/Ga(As,Sb) heterostructures. *Nanotechnology*, 28(2):025701, 2017. doi: 10.1088/0957-4484/28/2/025701.
- [126] C Möller, F Zhang, C Fuchs, C Berger, A Rehn, A Ruiz Perez, A Rahimi-Iman, J Hader, M Koch, J V Moloney, S W Koch, and W Stolz. Fundamental transverse mode operation of a type-II vertical-external-cavity surface emitting laser at 1.2 μm . *Electron. Lett.*, 53(2):93 – 94, 2017. doi: 10.1049/el.2016.3732.
- [127] P Kükelhan, A Beyer, C Fuchs, M J Weseloh, S W Koch, W Stolz, and K Volz. Atomic structure of “W”-type quantum well heterostructures investigated by aberration-corrected STEM. *J. Microsc.*, 268(3):259 – 268, 2017. doi: 10.1111/jmi.12647.

Acronyms

CBr₄ – tetrabromomethane

CHCC – conduction band – heavy hole band, conduction band – conduction band

CHSH – conduction band – heavy hole band, spin-orbit split off band – heavy hole band

CW – continuous wave

DBR – distributed Bragg reflector

DETe – diethyltellurium

DFB – distributed feedback

EL – electroluminescence

fcc – face-centered cubic

GFR – Gas Foil Rotation[®]

HR-XRD – high resolution X-ray diffraction

IBA – inter-band absorption

ICBA – inter-conduction band absorption

IVBA – inter-valence band absorption

LCF – longitudinal confinement factor

MOVPE – metal organic vapor phase epitaxy

OSA – optical spectrum analyzer

PL – photoluminescence

QW – quantum well

QWH – quantum well heterostructure

RPG – resonant periodic gain

SCH – separate confinement heterostructure

TBAs – tertiarybutylarsine

TBP – tertiarybutylphosphine

TEGa – triethylgallium

TESb – triethylantimony

TMAI – trimethylaluminum

TMIn – trimethylindium

VCSEL – vertical-cavity surface-emitting laser

VECSEL – vertical-external-cavity surface-emitting laser

List of Figures

2.1	Schematic illustration of the band structure of III/V semiconductors	4
2.2	Schematic illustration of fundamental light–matter interaction processes in semiconductors	5
2.3	Plot of the band gap energy against the lattice constant of III/V semiconductors	7
2.4	Schematic illustration of electrical confinement, gain-guiding and optical confinement in semiconductor lasers	9
2.5	Schematic illustration of longitudinal modes in diode lasers	11
2.6	Schematic illustration of a VECSEL	14
2.7	Schematic illustration of charge carrier leakage from quantum wells	16
2.8	Schematic illustration of Shockley–Read–Hall recombination	17
2.9	Schematic illustration of inter-band absorption	18
2.10	Schematic illustration of Auger processes in semiconductors	19
2.11	Schematic illustration of type-I, -II, and -III band alignments	21
2.12	Schematic illustration of type-II “W”-quantum well heterostructure	21
3.1	Schematic atomic scale illustration of a MOVPE growth process	26
3.2	Schematic illustration of HR-XRD in strained heterostructures	27
3.3	Schematic illustration of excitation and recombination processes in PL studies	30
3.4	Schematic illustration of a PL setup	31
3.5	Schematic illustration of excitation and recombination processes in EL and laser studies	32
3.6	Schematic illustration of an EL and laser studies setup	33
4.1	HR-XRD patterns of “W”-QWH samples with different antimony concentrations and comparison of a room temperature type-II PL spectrum with type-I reference samples	36
4.2	EL spectra and laser characteristics of a single “W”-QWH laser emitting at 1.2 μm	38
4.3	Current density-dependent EL spectra below laser threshold of a single and a double “W”-QWH laser emitting at 1.2 μm	39

4.4	Temperature-dependence of the threshold current density and the differential efficiency of a single and a double “W”-QWH laser	40
4.5	Temperature-dependence of the laser emission wavelength of the single “W”-QWH laser, the double “W”-QWH laser, the single “W”-QWH laser with GaP interlayers, and a (GaIn)(NAs) double QWH laser	41
4.6	Temperature-dependent VECSEL characteristics and pump power-dependent EL spectra above laser threshold for a heat sink temperature of 0 °C . . .	42
4.7	Temperature-dependent EL spectra and laser characteristics of a double “W”-QWH laser emitting at 1.3 μm	44

List of Tables

2.1	Summary of band parameters of GaAs, InAs and GaSb	6
2.2	Summary of bowing parameters for (GaIn)As and Ga(AsSb)	6
4.1	Overview of important growth-related, structural, and optical parameters of samples discussed in the growth study	36